

ON THE INTERNAL PROCESSES MODULATING TROPICAL CYCLONE  
INTENSITY: TURBULENT STRESSES AND SUBMESOSCALE DYNAMICS

A Dissertation

Submitted to the Graduate School  
of the University of Notre Dame  
in Partial Fulfillment of the Requirements  
for the Degree of

Doctor of Philosophy

by

Chibueze Nnamdi Oguejiofor

---

David H. Richter, Director

Graduate Program in Civil and Environmental Engineering and Earth Sciences

Notre Dame, Indiana

October 2024

This document is in the public domain.

# ON THE INTERNAL PROCESSES MODULATING TROPICAL CYCLONE INTENSITY: TURBULENT STRESSES AND SUBMESOSCALE DYNAMICS

Abstract

by

Chibueze Nnamdi Oguejiofor

Forecasting rapid intensity changes in hurricane intensity continues to evade current weather forecasting models, largely due to the multiscale dynamics of hurricanes. Typically, dynamical processes with scales below that of the forecasting model are parameterized. Thus, a clear understanding of the physics of these processes (from submesoscale to turbulent scale) is paramount to hurricane intensity forecast improvement.

This dissertation presents some progress in the characterization of turbulent eddies, their influence on hurricane mean intensity and the kinematics of their evolution as they relate to extreme Reynolds stress occurrence in the hurricane boundary layer. In addition, a framework for the representation of multiscale sea surface temperature (SST) anomalies, constrained by realistic satellite observations in rapidly intensifying storms, is presented. The results from this dissertation is expected to guide the improvement of turbulence parameterization schemes as well as the prediction of hurricane rapid intensification in current operational weather forecasting models.

I would like to dedicate this dissertation to my parents, Mr. and Mrs. Oguejiofor, for the unconditional love and support. You both are my first true mentors and I look forward to continually making you proud.

# CONTENTS

Figures . . . . .	v
Tables . . . . .	xi
Acknowledgments . . . . .	xii
Chapter 1: Introduction . . . . .	1
1.1 Background and Motivation . . . . .	1
1.2 Research Objectives and Dissertation Structure . . . . .	4
Chapter 2: Onset of Tropical Cyclone Rapid Intensification: Evaluating the response to Length Scales of Sea Surface Temperature Anomalies . . . . .	7
2.1 Introduction . . . . .	7
2.2 Data and Methodology . . . . .	10
2.2.1 Sea Surface Temperature (SST) data . . . . .	10
2.2.2 Mathematical framework: random field theory . . . . .	13
2.2.3 Structure function and spectral analysis of SST field. . . . .	15
2.2.4 Simulated sea surface temperature fields . . . . .	18
2.2.5 Model Setup . . . . .	19
2.2.5.1 Length scale experiment – A . . . . .	21
2.2.5.2 Length scale experiment – B . . . . .	21
2.2.5.3 Translating storm experiment . . . . .	23
2.3 Results and Discussion . . . . .	23
2.3.1 Evaluating the response of stationary storms to SST length scales . . . . .	23
2.3.1.1 Sensitivity of Modeled Storms to SST length scales . . . . .	23
2.3.1.2 Isolating the contribution of SST length scales . . . . .	30
2.3.1.3 The Influence of Scale-Induced Convective Asymmetries on RI Onset Timing . . . . .	32
2.3.2 Investigating the effect of storm translation speed on the variance in RI onset timing . . . . .	37
2.4 Conclusions . . . . .	42
2.5 Acknowledgments . . . . .	46

Chapter 3: The Role of Turbulence in an Intense Tropical Cyclone: Momentum Diffusion, Eddy Viscosities, and Mixing Lengths . . . . .	47
3.1 Introduction . . . . .	47
3.2 Simulation Methodology . . . . .	51
3.3 Results . . . . .	55
3.3.1 The Mean Velocity Fields . . . . .	59
3.3.2 Mean Field Budget - The Role Of Turbulent Eddies . . . . .	62
3.3.3 The Validity Of Eddy Viscosity Hypothesis & Estimates Of Effective Mixing Lengths . . . . .	67
3.3.4 A Revised Formulation Of Eddy Viscosities . . . . .	81
3.4 Conclusions and Discussion . . . . .	85
3.5 Acknowledgments . . . . .	87
Chapter 4: Near-surface Coherent Structures in an Intense Tropical Cyclone: Conditional Eddies and Vertical Momentum Fluxes . . . . .	88
4.1 Introduction . . . . .	88
4.2 Methodology . . . . .	91
4.2.1 Numerical Model And Dataset Description . . . . .	91
4.2.2 Conditional Averaging and Compositing . . . . .	94
4.3 Results . . . . .	95
4.3.1 Near-surface mean velocity fields & turbulent fluxes . . . . .	95
4.3.2 Quadrant analysis . . . . .	98
4.3.3 The structure of educed conditional eddies . . . . .	101
4.4 Discussion and Conclusions . . . . .	107
4.5 Acknowledgments . . . . .	108
Chapter 5: Dissertation conclusion . . . . .	110
Appendix A: Ocean observation of SST during Hurricane Irma's (2017) passage	113
Appendix B: Variogram estimation and Anisotropy . . . . .	115
Appendix C: Mean Field Budget Analyses . . . . .	118
Appendix D: Structure of Conditionally Averaged Sweep Events . . . . .	123
Bibliography . . . . .	125

## FIGURES

1.1	Intensity forecasts (initialized on 10/24/2023 00:00:00) of Hurricane Otis's intensity $\approx 31$ hours before landfall. The solid colored lines denote the forecasted intensity from various dynamical model while the dotted black line indicates the actual intensity. (source: Tomer Burg, CIRES/NOAA)	2
1.2	Track of Hurricane Otis over warm SST anomalies right before it's unprecedented stint of rapid intensification and landfall. (source: Brian McNoldy, University of Miami)	3
2.1	Broad framework and methodology used in this study	9
2.2	(a) Map showing the track traversed by Hurricane Irma (2017). (b) Map showing the distribution of ocean instrument measuring ocean conditions of Hurricane Irma (ALAMO floats and AXBTs) along the track of Hurricane Irma. (c) NASA's MODIS 1km Satellite product showing the sea surface temperature conditions of the boxed field in (a) and (b) on 05/09/2017. (d) Probability density distribution of SST field shown in (c). (e) A plot of the International Best Track Archive for Climate Stewardship (IBTrACS) intensity chart for Hurricane Irma.	12
2.3	(a) 2D Power spectral density curve of the SST field shown in Fig. 2.2 (c), with the red line showing the 7/5 slope line. (b) Percentage variance contribution from different length scales; the full integral of panel (a) represents the total variance.	17
2.4	Sample of SST fields with length scales corresponding to (a) 360 km, (b) 144 km, (c) 72 km, (d) 36 km.	18
2.5	Intensity plots of modeled storms with initial RMW of 36 km using ensemble SST random fields with length scales of (a) 360 km, (b) 144 km, (c) 72 km, and (d) 36 km.	25
2.6	(a) Variance of maximum 10-m wind speed against integration time for selected length scale simulations (solid lines) and intrinsic variability of model (dashed black line). (b) Variance of maximum 10-m wind speed for different length scales during selected times corresponding to intensification (50 hrs - black line, 60 hrs - purple line, 70 hrs - magenta line) and post intensification (80 hrs - golden line), showing a variance peak for a length scale of 360 km.	26

2.7	SST distribution for the ensemble members with (a) delayed RI, (c) early RI. Panels (b) and (d) show a closer view of the SST near the domain center with the initial RMW of 36 km overlaid, corresponding to <i>Random SST</i> <sub>1</sub> and <i>Random SST</i> <sub>8</sub> respectively in Fig. 2.5a. . . .	27
2.8	Ensemble plots of reflectivity (at 1 km height) on model day 3 for length scales of 36 km (first column), 72 km (second column), 144 km (third column) and 360 km (fourth column). . . . .	28
2.9	Plots of spatial correlation coefficient between SST & reflectivity (at 1km altitude) and SST & surface accumulated rainfall at for <i>Random SST</i> <sub>1</sub> and <i>Random SST</i> <sub>8</sub> shown in Fig. 2.11b and f respectively. The dashed vertical line shows the timing of RI onset for both simulations. . . .	29
2.10	Same as Fig. 2.6a but using constant variance in SST fields. . . . .	31
2.11	(a) Intensity plots of three selected simulations ( <i>Random SST</i> <sub>1</sub> , <i>Random SST</i> <sub>3</sub> and <i>Random SST</i> <sub>8</sub> ) with a length scale of 360 km, (b – d – f) Time-invariant SST fields for the selected three simulations shown in (a), (c – e – f) Simulated radar reflectivity at 72 hours for the selected three simulations shown in (a). . . . .	32
2.12	Box and whisker plots of SST values (for (a) 360 km and (b) 36 km length scale) within a 36 km radius beneath the domain center where the storm vortex was initialized. The nine box and whisker plots in each panel are for the nine ensemble members for each SST anomaly size. . . . .	34
2.13	Azimuthally averaged vertical velocity ( $\text{m s}^{-1}$ ) from 48 - 96hrs (RI phase) for <i>RandomSST</i> <sub>1</sub> , <i>RandomSST</i> <sub>3</sub> and <i>RandomSST</i> <sub>8</sub> shown in Fig. 2.11. . . . .	36
2.14	Illustration of the start (solid blue box) and end location of storms translating at $2.5 \text{ m s}^{-1}$ and $5.0 \text{ m s}^{-1}$ (solid and dashed black boxes respectively) over an SST field with length scale = 360 km for 10 days (zoomed view of stationary case shown in Fig. 2.11f). . . . .	37
2.15	Line plots of variance in maximum 10-m wind speed amongst ensemble simulations for a stationary storm (solid blue line), $2.5 \text{ m s}^{-1}$ translation speed (solid green line) and $5.0 \text{ m s}^{-1}$ translation speed (solid red line), intrinsic variability (dashed black line). Experiments are for small sized storm (RMW = 36 km) translating over SST anomalies with a length scale of 360 km. . . . .	38
2.16	Same as Fig. 2.11 (c) - (e) - (g), but with the storm translating from left to right at $2.5 \text{ m s}^{-1}$ and $5.0 \text{ m s}^{-1}$ . . . . .	40
2.17	Same as the last row in Fig. 2.13, but for a storm translating from left to right at $2.5 \text{ m s}^{-1}$ and $5.0 \text{ m s}^{-1}$ . . . . .	42

2.18	Comparing the intensity evolution of a stationary and translating storm, same as the golden line plot ( <i>Random SST</i> <sub>8</sub> ) in Fig. 2.11a but with plots of the effect of various translation speeds included as solid (2.5 m s <sup>-1</sup> ) and dashed (5.0 m s <sup>-1</sup> ) black lines. . . . .	43
2.19	Schematics showing updraft and spatial distribution of convection and convective bursts induced by the magnitude of SST length scales for (a) Small length scales, (b) Larger length scales and (c) Larger length scales with a storm translating at $U_T$ , relative to the storm center. The red and blue region represent relatively warmer and cooler SSTs.	45
3.1	Schematic showing the model-simulation setup. The green box (LES subdomain) represents the region on which the analysis presented in this study is focused. Color shading qualitatively represents near-surface wind speed, with red colors being the highest values. . . . .	53
3.2	Horizontal cross sections of the vertical velocity field $w$ [m/s] around the SW quadrant of the storm, at different heights. The black vertical arrow passes through the eye of the storm. . . . .	56
3.3	Windowed-in horizontal cross sections of (a) vertical velocity [m/s] in the southwest quadrant of the LES model domain and (b) water vapor mixing ratio [kg/kg], at $z \approx 700$ m. Vertical cross sections of (c) vertical velocity [m/s] and (e) potential temperature [K] in the inner eyewall ( $r \approx 11$ km). Vertical cross sections of (d) vertical velocity [m/s] and (f) potential temperature [K] outside the eyewall ( $r \approx 22$ km). The black and blue lines in (a) represent the locations (inner eyewall and outside the eyewall respectively) from which the vertical sections in (c) & (e) and (d) & (f) are plotted, respectively. The boxes in (c) and (d) highlight the vertical extent of two kilometer-scale intense downdraft features in (a). . . . .	57
3.4	Plots of the azimuthally and time-averaged velocity components for (a) tangential velocity $\langle v \rangle$ , (b) radial velocity $\langle u \rangle$ and (c) vertical velocity $\langle w \rangle$ , all in [m/s]. The solid and dashed black contour lines in each panel indicates $\langle w \rangle$ at $\pm 1.0$ m/s, highlighting the eyewall region and a significant downdraft feature just outside the eyewall, respectively. (d) Plot showing the nomenclature used in the identification of regions in the simulation; the top of the boundary layer (BL) is considered to be roughly (but not strictly) at 1 km. . . . .	61
3.5	Contour plots of azimuthally and time-averaged radial velocity field $\langle u \rangle$ , overlain with shadings from the contributions due to turbulent eddy tendencies in the (a) radial ( $T_r^u + \langle F_r^u \rangle$ in $ms^{-2}$ ) and (b) vertical ( $T_z^u + \langle F_z^u \rangle$ in $ms^{-2}$ ) directions. Panels (c) (for $T_r^v + \langle F_r^v \rangle$ ) and (d) (for $T_z^v + \langle F_z^v \rangle$ ) represent analogous plots for the average tangential velocity field $\langle v \rangle$ . Panels (e) (for $T_r^w + \langle F_r^w \rangle$ ) and (f) (for $T_z^w + \langle F_z^w \rangle$ ) represent analogous plots for the average vertical velocity field $\langle w \rangle$ . . . . .	64

3.6	Profiles for $z=0 - 200\text{m}$ , of resolved ( $T_z^v$ in $[ms^{-2}]$ - red line), parameterized ( $\langle F_z^v \rangle$ in $[ms^{-2}]$ - blue line) and total ( $T_z^v + \langle F_z^v \rangle$ - black line) turbulent tendencies in the vertical direction for the tangential velocity (shown in Fig. 3.5d) at (a) $r=10\text{km}$ , (b) $r=12.5\text{km}$ and (c) $r=22\text{km}$ . . . . .	66
3.7	Contour plots of mean radial velocity $\langle u \rangle$ in $[\text{m/s}]$ , overlain by shadings of (a) azimuthally and time-averaged vertical fluxes of radial velocity $\langle u'w' \rangle$ in $[m^2s^{-2}]$ , (b) the vertical gradient of mean radial velocity $\frac{\partial \langle u \rangle}{\partial z}$ in $[s^{-1}]$ and (c) the effective eddy viscosity $K_z^u$ , in $[m^2s^{-1}]$ . [Plots (b) and (c) use the same contour interval for $\langle u \rangle$ as in (a)]. Panels (d) and (e) show near-surface profiles of $\langle u'w' \rangle$ and $K_z^u$ respectively, for the first 200m height, at $r=10\text{km}$ (solid-blue line), $r=17.5\text{km}$ (dashed-blue line) and $r=22\text{km}$ (dotted-blue line). . . . .	69
3.8	Contour plots of mean tangential velocity $\langle v \rangle$ in $[\text{m/s}]$ , overlain by shadings of (a) azimuthally and time-averaged vertical fluxes of tangential velocity $\langle v'w' \rangle$ in $[m^2s^{-2}]$ , (b) the vertical gradient of mean tangential velocity $\frac{\partial \langle v \rangle}{\partial z}$ in $[s^{-1}]$ and (c) the effective eddy viscosity, $K_z^v$ in $[m^2s^{-1}]$ . [Plots (b) and (c) use the same contour interval for $\langle v \rangle$ as in (a)]. Panels (d) and (e) show near-surface profiles of $\langle v'w' \rangle$ and $K_z^v$ respectively, for the first 200m height, at $r \approx 10\text{km}$ (solid-blue line), $r \approx 12.5\text{km}$ (dashed-blue line) and $r \approx 22\text{km}$ (dotted-blue line). . . . .	71
3.9	(a) Plot of effective eddy viscosity, $K_{\text{eff}}^v$ in $[m^2s^{-1}]$ . Vertical profiles of $K_{\text{eff}}^v$ - black line, $K_w$ - red line and $K_m$ - blue line at (b) $r \approx 10\text{km}$ and (c) $r \approx 22\text{km}$ . [The black vertical lines in (a) indicate the radii where the black profiles in (b) and (c) are plotted]. The insets in (b) and (c) show windowed-in plots of the first 100m height of the BL. . . . .	73
3.10	Plots of the effective mixing length ( $L_{\text{eff}}^v$ ) in meters. (a) Radius-height plot. (b)-(c) Vertical profiles of $L_{\text{eff}}^v$ (black line) and analytical Louis-type profiles (red dashed lines, with $L_\infty = 150\text{m}$ ) and the Prandtl theoretical surface layer relations (gray line) at (b) $r=10\text{km}$ and (c) $r=22\text{km}$ . (d) Radial variation of $L_{\text{eff}}^v$ at $z = 0.75, 1.0$ and $1.25\text{km}$ (black, red and blue lines respectively). [The black vertical lines in (a) indicate the locations of the profiles in (b) and (c). The solid and dashed black contours in (a) indicate $\langle w \rangle$ at $\pm 1.0\text{m/s}$ .] . . . . .	75
3.11	Contour plots of $\frac{\langle v \rangle}{r}$ in $[s^{-1}]$ , overlain by shadings of (a) azimuthally and time-averaged radial fluxes of tangential velocity $\langle u'v' \rangle$ in $[m^2s^{-2}]$ , (b) $r \times$ the radial gradient of rotation rate $r \frac{\partial \langle v \rangle}{\partial r} \frac{1}{r}$ in $[s^{-1}]$ and (c) the effective eddy viscosity, $K_h$ in $[m^2s^{-1}]$ . [Plots (b) and (c) use the same contour interval for $\frac{\langle v \rangle}{r}$ as in (a).] . . . . .	80

3.12	Plots of (a) effective radial eddy viscosity, $K_{\text{eff}}^h$ in $[m^2s^{-1}]$ using (3.14) and (b) effective vertical eddy viscosity, $K_{\text{eff}}^v$ in $[m^2s^{-1}]$ using (3.15). The solid black contour line in each panel indicates $\langle w \rangle$ of +1.0m/s, highlighting the eyewall region. The solid and dashed gray contour lines in each panel show the mean radial velocity $\langle u \rangle$ , using the same contour interval as in Fig. 3.7(a). . . . .	83
4.1	(a) Horizontal cross section of the vertical velocity field at $z \approx 700\text{m}$ . (b) and (c) show windowed-in regions of the N-W quadrant illustrating the organization of turbulent velocity structures in the outer eyewall and eye-eyewall interface respectively. [A plane view of the 3D vertical velocity isosurface (for (c)) is shown in Fig. 2 below (bottom-center panel i.e., $T_4$ )]. . . . .	92
4.2	Three-dimensional isosurfaces (plan view) of instantaneous velocity structures (i.e., intense downdrafts with $w = -8\text{ms}^{-1}$ ) advected – from $T_0$ to $T_5$ – along the eye-eyewall interface of the simulated Category 5 hurricane. The interval between each time step ( $\Delta T$ ) is 20s and the red-dashed line in all panels marks $r \approx 11\text{km}$ , indicating the eye-eyewall interface. [The bottom-center panel, marked $T_4$ , shows the same time instance as Fig. 1(c) above]. . . . .	93
4.3	(a) Horizontal profiles of the azimuthally and time-averaged radial $\langle u \rangle$ (solid red line), tangential $\langle v \rangle$ (solid blue line) and vertical $\langle w \rangle$ [multiplied by a factor of 10 for visibility] (solid black line) velocity components (all in m/s) at $z \approx 63\text{m}$ height, with the dashed black lines indicating the radii (11.5km, 15.5km and 26km) where the vertical profiles in (b), (c) and (d) are plotted. (d) Horizontal profiles of the azimuthally and time-averaged vertical fluxes of radial velocity (red line – $\langle u'w' \rangle$ ) and tangential velocity (blue line – $\langle v'w' \rangle$ ). . . . .	96
4.4	Quadrant distribution of fluctuating velocity components ( $u'$ , $v'$ and $w'$ ) in the inner eyewall ( $r \approx 10 - 13\text{km}$ – (a),(b)), outer eyewall ( $r \approx 14 - 17\text{km}$ – (c),(d)) and inflowing boundary layer ( $r \approx 22 - 30\text{km}$ – (e),(f)), at 63m height above the surface. The red dashed curves in each panel represents arbitrary hyperbolic curves to visually identify extreme events. The blue, brown, green and black numbers in each quadrant denotes the mean flux components from the $Q_1$ , $Q_2$ , $Q_3$ and $Q_4$ quadrant respectively. . . . .	99

4.5	Horizontal sections through the center of the normalized conditionally-averaged structure (denoted by "x") in the (a) inner eyewall, (b) outer eyewall and (c) inflowing BL. The vectors $[(u', v')]$ , at the top right corner of each panel, represents the normalized fluctuating velocity components (exaggerated by $\times 7$ for visibility), while the red contours indicate the Q-criteria with $[\text{min}, \text{max}, \text{interval}] = [-15, 15, 0.75]$ . The blue arrow in panel indicates the mean flow direction at the center of the averaging radii. . . . .	102
4.6	Transverse – [(b), (d), (f)] and longitudinal – [(c), (e), (g)] slices through the center of the normalized conditionally-averaged structure (denoted by "x") in the inner eyewall (Fig. 4.5(a) above). The vectors $[(u', w'), (v', w')]$ respectively, at the top right corner of each panel, represents the normalized fluctuating velocity components (exaggerated by $\times 7$ for visibility), while the red contours indicate the Q-criteria with $[\text{min}, \text{max}, \text{interval}] = [-15, 15, 0.75]$ . . . . .	104
4.7	3D isosurfaces of Q-criteria=1.0 in top view – (a) and side view – (b) for the conditionally averaged structure in the inner eyewall, shown in Fig. 4.5(a). The dashed black lines cut across the centroid of the structure. . . . .	105
A.1	Temporal variation of upper ocean temperature, measured from four selected ALAMO floats distributed across the path of Hurricane Irma (2017) as shown in Fig. 2.2b. . . . .	114
B.1	Experimental omni-directional variogram (N-S and E-W direction) of the SST field traversed by Hurricane Irma (2017). . . . .	116
B.2	(a) Experimental directional variogram (N-S and E-W direction) of the SST field traversed by Hurricane Irma (2017), (b) Experimental variogram for E-W direction fitted with spherical theoretical variogram, (c) Experimental variogram for N-S direction fitted with spherical theoretical variogram. . . . .	117
C.1	As in Fig. 3.5 except showing the contribution from other mean-field terms in the budget equation shown in Eqs. (3.1) and (3.2), as indicated at the top of each panel. . . . .	120
C.2	As in Fig. 3.5 except showing terms related to the contribution of resolved and parameterized turbulence to the mean field budget, as indicated at the top of each panel. . . . .	121
C.3	As in Fig. 3.5(c)–(d) except showing the contribution from other mean-field and turbulent terms in the budget equation shown in Eq. (3.3), as indicated at the top of each panel. . . . .	122
D.1	Same as Fig. 4.5(a) and Fig. 4.6, but for sweep events i.e., $Q_4: [+u', -w'], [+v', -w']$ . . . . .	124

## TABLES

2.1	Summary of the three groups of numerical experiments in this study .	22
-----	--	----

## ACKNOWLEDGMENTS

Reading this dissertation in its entirety, I have come to realize that it is indeed a culmination of several years of academic training spanning three continents and four countries. Up until this very moment, I never fully appreciated how much work it took to pursue my graduate studies so far from where I grew up calling home (Lagos, Nigeria). While I believe that I handled this challenge pretty well, it would not have been possible without the support of a number of people.

I would like to acknowledge the support of my PhD advisor, Prof. David H. Richter, for giving me the opportunity to study under his guidance at the University of Notre Dame. Our intellectual exchange over the years nudged me in the direction of academic rigor that have and will prove useful over the coming years. I would also like to appreciate Dr. George Bryan for hosting my multiple academic research visits to NSF NCAR. I sincerely appreciate Dr. Richard Rotunno. Our random meeting in an elevator at the AMS 2021 Hurricanes meeting began a series of collaboration and mentorship that I hold dear. I also would like to recognize the support and guidance of Dr. Peter Sullivan. Amongst other lessons, our conversations have taught me to always keep an eye out for the bigger picture, both in my research career and more generally in life.

## CHAPTER 1

### INTRODUCTION

#### 1.1 Background and Motivation

Hurricanes are one of the most catastrophic natural phenomena on the planet. According to the NOAA annual report, they accounted for  $>52\%$  of the total cost of weather related disasters ( $\approx 31$  billion dollars/year), in the United States between 1980 and 2022. In addition, the death toll from hurricane related disasters have been estimated to be between 300,000–500,000 lives for Tropical Cyclone Bhola (1970) and more recently, 149 lives for Hurricane Ian (2022). Even as the science of hurricane prediction makes substantial leaps, the increasing occupation of coastal cities and flood-prone regions pose an increased risk to human life and property, specifically in the wake of an ever changing climate.

The widespread devastation caused by intense tropical cyclones (TC) in recent decades can be partly attributed to current limitations in accurately forecasting their “rapid intensification (RI)”. This sudden ( $\geq 15.0$  m/s increase in wind speed over 24 hours or less) intensity change continues to evade traditional weather forecasting systems, giving coastal communities insufficient time to effect necessary evacuation protocols. Figure 1.1 shows a recent example (Hurricane Otis) rapidly intensifying from tropical storm to a Category 5 hurricane in less than 24hrs – one of the fastest RI case yet. Figure 1.1 also indicates the failure of all TC forecast models in capturing the predicted intensity of the storm, costing damages to the tune of 3.5 - 15 Billion dollars and about 51 lives [71]. The inherent multiscale nature of TC dynamics lies

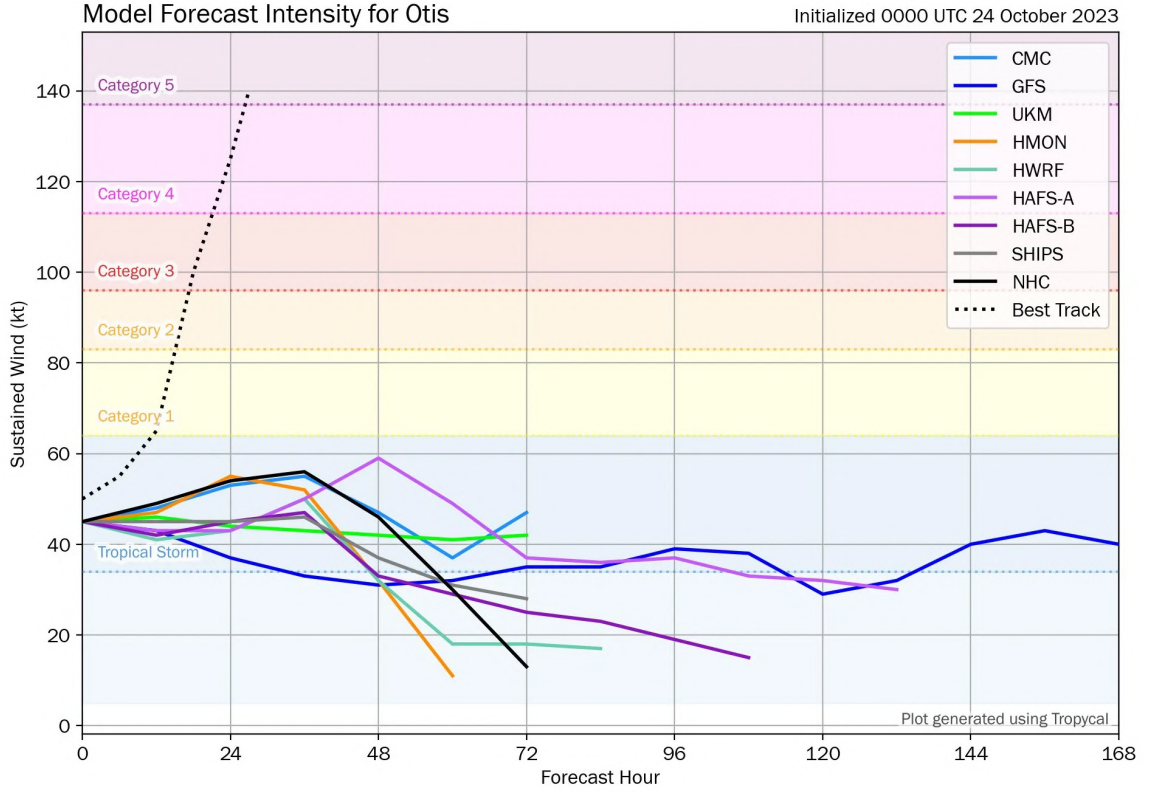


Figure 1.1. Intensity forecasts (initialized on 10/24/2023 00:00:00) of Hurricane Otis's intensity  $\approx 31$  hours before landfall. The solid colored lines denote the forecasted intensity from various dynamical model while the dotted black line indicates the actual intensity. (source: Tomer Burg, CIRES/NOAA)

at the core of this challenge in predicting RI. In the case of Hurricane Otis, Figure 1.2 shows that the track (black solid line) crossed over SST anomalies with temperatures of about  $31^{\circ}$  Celcius, possibly fuelling it's rapid intensification. However, the least understood scales are those associated with turbulence – which modulates heat, moisture and momentum exchange at the air-sea interface between the TC and the ocean underneath.

Recent studies spanning across theory, observation and modeling, have shown that SST anomalies such as mesoscale ocean eddies (with a lifetime of  $\approx 10 - 100$

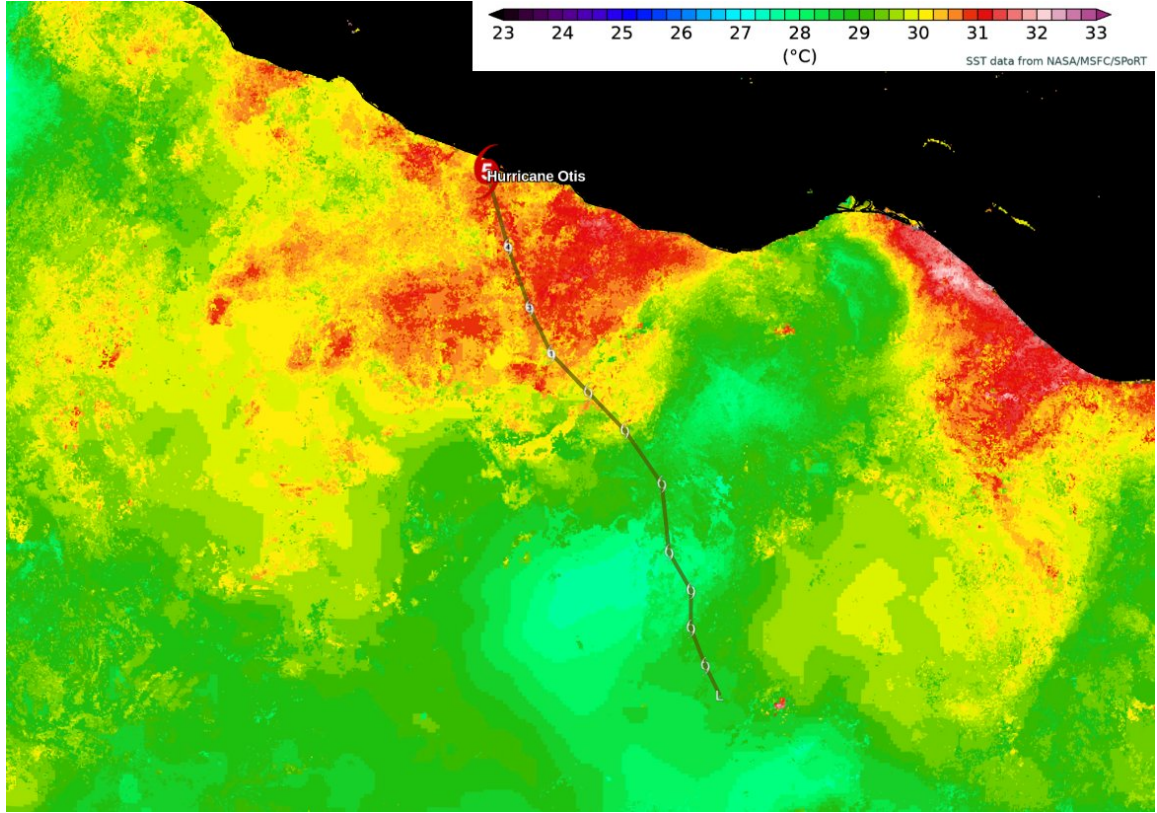


Figure 1.2. Track of Hurricane Otis over warm SST anomalies right before it's unprecedented stint of rapid intensification and landfall. (source: Brian McNoldy, University of Miami)

days) modulate air-sea interaction within the TC environment that strongly influences the storm intensity. To date, however, the lack of understanding of these high-resolution spatiotemporal processes, particularly in the most intense regions of the storm, presents a huge gap in knowledge and can lead to oversimplifications of their representation in numerical weather prediction models; hence the continued difficulty in prediction of TC rapid intensification. This is further compounded by the changing climate, driving long term (multi decadal) increases in SST.

Furthermore, the lack of sufficiently high spatio-temporal observations of turbulent processes in the TC eyewall region poses great challenges in the parameterization

in weather forecast models. Owing to their coarse resolution, these models must approximate the nature of turbulent processes in hurricanes.

## 1.2 Research Objectives and Dissertation Structure

The broad research objectives of this dissertation centers on the understanding of the multiscale internal processes which affect the mean intensity of intense hurricanes, as well as the onset of their rapid intensification. Seeing that uncertainties in these processes are the major factors which currently limit intensity forecasts, understanding them would allow for better advance warning systems, decision making and disaster preparedness, in line with the broader impacts of scientific research. This dissertation aims to make impactful scientific contributions at scales which prove extremely difficult for both observation and weather prediction, improving hazard mitigation at the local level, especially for coastal communities with increasing exposure to disasters in the face of a changing climate.

To this end, using a combination of mesoscale ( $\approx 2000\text{m}$  horizontal grid spacing) and large-eddy ( $\approx 30\text{m}$  horizontal grid spacing), this dissertation poses and addresses key questions related to the physics of hurricane intensity. In the following sections, the setup of numerical experiments as well as detailed outline of research methodology is presented and discussed. The rest of this dissertation is outlined as follows.

In Chapter two, to address the on-going problem of predicting TC RI, we developed a novel geostatistical methodology which utilizes satellite imagery of SST conditions around a specific tropical cyclone to predict the onset of RI. Experimental variograms of the observed gridded SST conditions are modeled – constrained by the appropriate length scale contribution to the total variance from spectral analysis – and used to generate multiple realizations of unconditional gaussian random fields. The different realizations of ensemble random fields are generated with varying SST length-scales with the aim of studying the effect of SST length-scales on

the timing of the onset of intensification. The generated SST fields are used as input fields for model runs. Our methodology was implemented for Category 4 – Hurricane Irma (2017), using SST fields of the storm environment just before RI, as captured by NASA’s MODIS (Moderate Resolution Imaging Spectroradiometer) satellite imagery. In agreement with previous studies, we show that the magnitude of SST anomalies underneath the eye – eyewall region plays an important role in modulating the timing of the onset of RI. Beyond this, however, we find that the length scales of SST anomaly exceeding the initial storm size induce asymmetries in convection which can act to delay RI despite the presence of favourable SST conditions within the eyewall. This suggests that the mean SST in the core most certainly influences storm intensity, however it may not be the dominant factor in RI onset timing. Furthermore, the reduced exposure time of a moving storm to SST anomalies of a prescribed length, compared to a stationary storm, is seen to modulate the effect of the SST anomalies on storm development. Higher storm translation speeds reduce azimuthal asymmetries in convection by preventing the preferential development of convection over stationary warm SST anomalies, which removes a potential barrier to intensification.

In Chapter three, to address the *bulk* role of turbulence in intense TCs, we analyze the output of a large-eddy simulation (with  $\Delta x = \Delta y = 31.25\text{m}$ ,  $\Delta z = 15.625\text{m}$ ) of a Category-5 storm and its influence on the mean intensity. Azimuthally and temporally averaged budgets of the momentum fields show that TC turbulence acts to weaken the maximum tangential velocity, diminish the strength of radial inflow into the eye, and suppress the magnitude of the mean eyewall updraft. Turbulent flux divergences in both the vertical and radial directions are shown to influence the TC mean wind field, with the vertical being dominant in most of the inflowing boundary layer and the eyewall (analogous to traditional atmospheric boundary layer flows), while the radial becomes important only in the eyewall. The validity of the down-

gradient eddy viscosity hypothesis is largely confirmed for mean velocity fields, except in narrow regions which generally correspond to weak gradients of the mean fields, as well as a narrow region in the eye. This study also provides guidance for values of effective eddy viscosities and vertical mixing length in the most turbulent regions of intense TCs, which have rarely been measured observationally. A generalized formulation of effective eddy viscosity (including the Reynolds normal stresses) is presented.

Chapter four expands on Chapter 3: As opposed to the *bulk* results in the Chapter 3, Chapter 4 digs deeper by investigating the instantaneous occurrences of near-surface extreme vertical momentum fluxes which were averaged out in the bulk analyses of the preceding chapter. First, profiles and quadrant analysis in the inflowing boundary layer, outer and inner eyewall are analysed to understand the mean near-surface conditions and dominant flux distribution. Then, the kinematics of coherent turbulent structures conditioned on "ejection" events and extreme vertical momentum fluxes are investigated in detail and found to be associated with a vortex core (as indicated by the Q-criteria) roughly inclined in the direction of the mean winds. The structure of this educed conditionally eddy is found to be similar in the inflowing boundary layer, outer eyewall and inner eyewall. Additionally, three dimensional isosurfaces of the vortex core shows it's head to be lifted downstream. The eddy structure educed via conditioning on "sweep" events is shown to be less coherent than for ejection events.

Finally, Chapter 5 summarizes the main findings from this dissertation (as discussed in Chapters 2, 3, and 4), drawing connections between the multiscale internal mechanisms modulating TC intensity.

## CHAPTER 2

# ONSET OF TROPICAL CYCLONE RAPID INTENSIFICATION: EVALUATING THE RESPONSE TO LENGTH SCALES OF SEA SURFACE TEMPERATURE ANOMALIES

The research in this chapter was carried out in collaboration with Charlotte Wainwright, Johna E. Rudzin and David H. Richter. It has been published in the journal of the Atmospheric Sciences (<https://doi.org/10.1175/JAS-D-22-0158.1>).

### 2.1 Introduction

Sea surface temperature (SST) represents one of the several multi-scale environmental parameters modulating hurricane intensity changes, alongside vertical wind shear (VWS), outflow jets, etc. [85, 54]. The magnitude of SST is a principal component of the wind-induced surface heat exchange (WISHE) TC paradigm, which suggests that a positive feedback between surface wind and heat/moisture fluxes is responsible for the intensification TCs [55, 84, 57]. Warm SST anomalies as little as  $1^{\circ}\text{C}$  have been shown to significantly increase the intensity of TCs [56, 189, 234] while cold SST anomalies (associated with the wind driven cooling) enhance a negative feedback mechanism which decreases TC intensity.

Warm and cold core ocean eddies in the subtropical zonal band of the North Pacific ocean are examples of SST anomalies. [119] shows that these mesoscale ocean anomalies have sizes varying from about 30 km to about 170 km and have a life span of up to 50 weeks, covering about 20–30% percent of the ocean surface [30, 35] and in some cases having a warm anomaly of  $1.4^{\circ}\text{C}$  at the surface and  $2.5^{\circ}\text{C}$  at a

depth of 370 m [242, 243]. Previous work has shown that the magnitude and sizes of the eddies influence the intensity of TCs as warm core eddies reduce the storm-wind induced cooling of SST and hence increase TC intensity [194, 114, 233, 116, 127, 185, 11, 120]. In one of the the more recent attempts to investigate the impacts of a spatial distribution of warm eddies, [210] examined the influence of the proximity of a fixed-size warm SST anomaly on a stationary storm using a suite of idealized experiments, finding that a warm SST anomaly close to the storm center enhances secondary circulation, increases heat fluxes, and hence strengthens the storm intensity. An opposite effect was noted for warm SST anomalies positioned farther from the storm center.

In addition to ocean mesoscale eddies, other SST anomalies exist, such as the cold wake generated by a TC, which can vary in size and have a lifespan of up to 4 days [170, 152], and hence affect the same TC or a subsequent storm. These interactions between TCs and their cold wakes have been investigated extensively in both observational studies [37, 76, 245, 188] as well as numerical simulations [31, 97]. Both types of studies generally agree that the net effect of a cold wake is to reduce the energy supply from warm SSTs, leading to a negative feedback which decreases the TC intensity. This process, however, depends on the translation speed of the TC [31].

Despite the advances in understanding the impact of SST on TC intensity changes, there are still open questions. For instance: what is the sensitivity of TC intensity to the multiscale nature of these SST anomalies (i.e., the spatial extent of horizontal heterogeneities in SST anomalies), and how does the size of the TC modulate this sensitivity? Studies have also shown that cold wakes can be advected by pre-existing warm eddies [152], suggesting an interaction of SST anomalies of varying length scales. More generally, how do these multiscale features modulate the timing of the onset of RI?

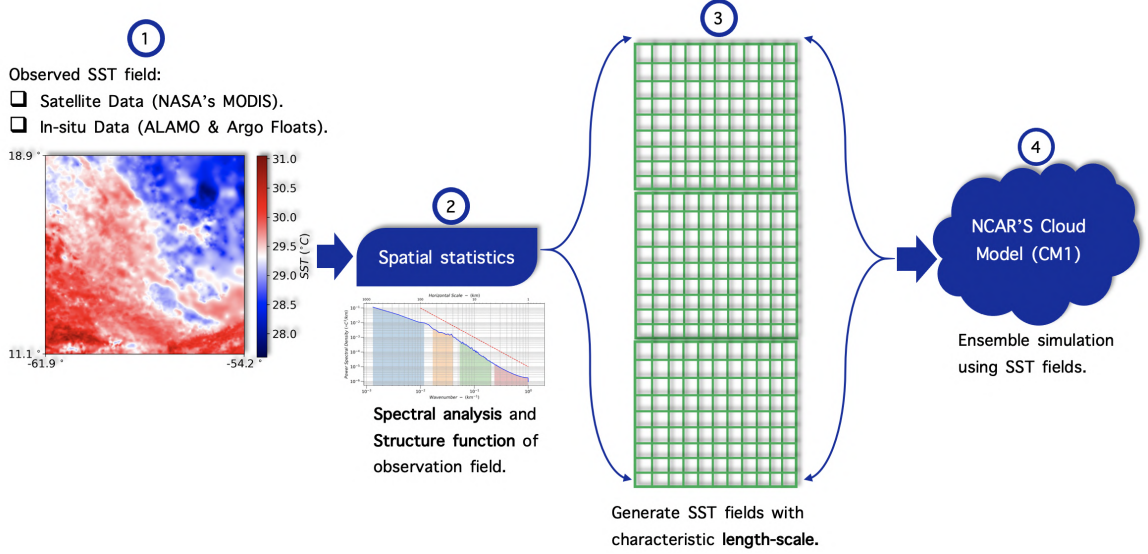


Figure 2.1. Broad framework and methodology used in this study

As described in the literature, the development and persistence of SST anomalies (ocean eddies and cold wakes of TCs), their modulation of air-sea interaction, and how these affect the RI of TCs remain an active area of research. The lack of high resolution spatio-temporal ocean observations of SST variation in the high-wind TC boundary layer suggests a gap in present knowledge and a possible oversimplification of physics therein. Furthermore, the dependence of RI on realistic size and spatial distribution of these SST anomalies remain unclear.

In this study, a geostatistical approach is utilized to understand the impact of the length scale of these SST anomalies on storm intensity using random field theory. SST fields obtained from NASA's multi-scale ultra high resolution (MUR) satellite imagery (1 km) provide spatial distribution of these anomalies during the rapid intensification phase of Hurricane Irma (2017). Spatial statistics of this SST field are used to generate multiple realizations of unconditional Gaussian random fields with varying length scale parameters in order to mimic the spatial extent of realistic SST

anomalies. The generated SST fields are used as boundary conditions for idealized model runs using Cloud Model 1 (CM1) [22]. This process is shown schematically in Figure 2.1. We investigate the impact of varying the SST length scale on subsequent TC dynamics and intensification.

Specific objectives of this study include:

1. Understanding the interaction between modeled storms and the length scales of SST anomalies. Specifically, we are interested in isolating the impact of these length scales and how they influence the variance in onset of rapid intensification.
2. Investigating the impact of storm translation speed on its interaction with SST anomalies. We aim to understand the impact of storm exposure time to these length scales of SST heterogeneities and how this modulates the variance in RI onset timing.

The remainder of this paper is organized as follows: Section 4.2 describes the broad framework of this study, beginning with the SST data and statistical analyses used to generate the realistic random SST fields. Following this is the model setup and an explanation of the suite of idealized uncoupled simulations conducted to investigate the impact of length scales of SST heterogeneities on RI, including how this sensitivity is affected by storm size and storm translation speed. Section 4.3 presents the results exploring the variances in the onset timing of rapid intensification and its sensitivity to spatial heterogeneities in SST. Section 4.3 also explores the sensitivity of the TC translation speed to the length scales of these SST anomalies. Finally, results discussed in section 4.3 are summarized with concluding remarks in Section 4.4.

## 2.2 Data and Methodology

### 2.2.1 Sea Surface Temperature (SST) data

Global high resolution ( $0.01^\circ \times 0.01^\circ$  grid) data obtained from NASA’s Multi-Scale Ultra High Resolution (MUR) project [36] provides a gap-free, gridded dataset

of daily SST during the life cycle of Hurricane Irma (2017). The dataset is synthesized by combining multiple Level-2 satellite SST datasets including: NASA Advanced Microwave Scanning Radiometer-EOS (AMSR-E), the JAXA Advanced Microwave Scanning Radiometer 2 (AMSR-2) on GCOM-W1, the Moderate Resolution Imaging Spectroradiometers (MODIS) on the NASA Aqua and Terra platforms, the US Navy microwave WindSat radiometer, the Advanced Very High Resolution Radiometer (AVHRR) on several NOAA satellites, and in situ SST observations from the NOAA iQuam project [239, 240, 241]. This high-resolution SST product has been used previously to analyze the high-wind environment of hurricanes, with validation using 415 collocated Airborne EXpendable BathyThermographs (AXBTs) showing about 70% difference in SST within a  $\pm 0.5^\circ\text{C}$  bound and 42% within a  $\pm 0.25^\circ\text{C}$  bound [185]. [93] extended this validation by adding in-situ measurements from two additional hurricanes (Earl (2010) and Isaac (2012)), leading to an overall SST root mean square error (RMSE) of  $0.8^\circ\text{C}$  from a total of 1085 data points. We note that for the purpose of this study, the RMSE is of minor importance, as the goal of our methodology is to conduct sensitivity experiments for varying SST length scales, not for getting a response to the exact SST field felt by Irma at that time.

Figures 2.2a and 2.2b show the track across the Atlantic followed by Hurricane Irma during its life cycle. The spatial distribution of SST over a  $8.0^\circ \times 8.0^\circ$  square grid during September 5th 2017 is shown in Fig. 2.2c. This square grid is selected at the specific time slice during the RI phase of Hurricane Irma (Fig. 2.2e) to show the multiscale nature of SST anomalies associated with a typical hurricane environment. As seen in Fig. 2.2c, there are SST anomalies of varying sizes (length scales) seen in this region. The data follow an approximately Gaussian distribution (Fig. 2.2d) of SST with a mean of  $29.4^\circ\text{C}$ , a variance of  $0.23^\circ\text{C}^2$ . In addition to the high-resolution satellite imagery of SST distribution, several AXBTs and Air-Launched Autonomous Micro Observers (ALAMOs) also made profile measurements of upper

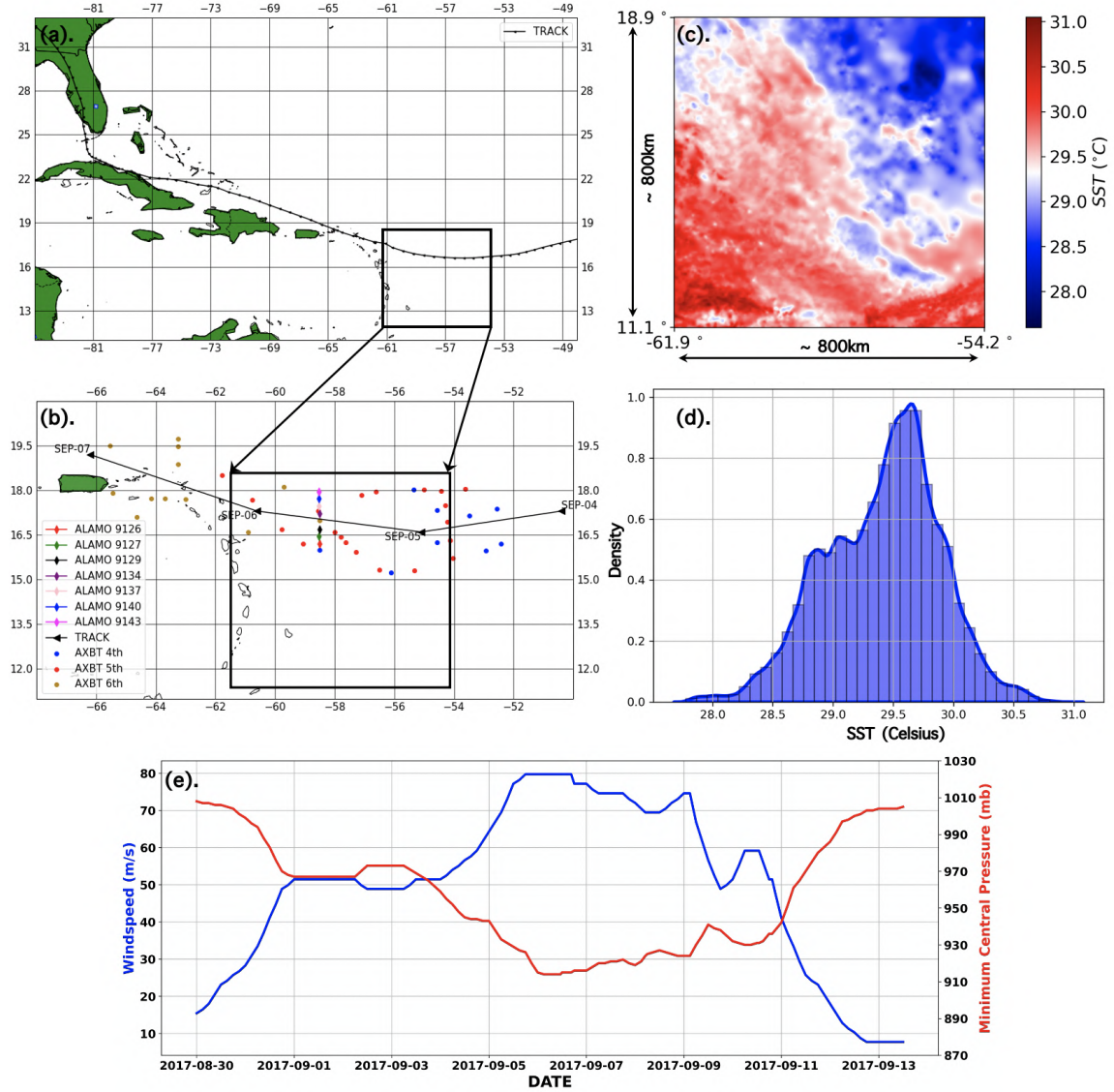


Figure 2.2. (a) Map showing the track traversed by Hurricane Irma (2017). (b) Map showing the distribution of ocean instrument measuring ocean conditions of Hurricane Irma (ALAMO floats and AXBTs) along the track of Hurricane Irma. (c) NASA's MODIS 1km Satellite product showing the sea surface temperature conditions of the boxed field in (a) and (b) on 05/09/2017. (d) Probability density distribution of SST field shown in (c). (e) A plot of the International Best Track Archive for Climate Stewardship (IBTrACS) intensity chart for Hurricane Irma.

ocean conditions in the domain of interest during the RI phase of Hurricane Irma, showing a warm upper ocean condition necessary for RI [186, 188]. See Appendix A for a description of ALAMO float measurements relative to Hurricane Irma’s path.

### 2.2.2 Mathematical framework: random field theory

Given a two-dimensional (2D) snapshot of a continuous variable such as SST, the value of SST at a point in space ( $\mathbf{x}_1, \mathbf{x}_2, \mathbf{x}_3 \dots \mathbf{x}_n$ ) can be assumed to be a random variable  $T(\mathbf{x})$  with a characteristic mean, variance and probability density function. A collection of random variables for all points in space for the above 2D field is defined as a random function and the actual set of values of  $T(\mathbf{x})$  that makes up this realization of the random function is known as the *regionalized variable* [230].

This regionalized variable can be represented as a stationary random process model with a characteristic structural component (i.e mean,  $T_\mu$ ) and two random components consisting of one spatially-correlated variation ( $\varepsilon$ ) and one uncorrelated variation ( $\varepsilon'$ ; i.e noise), as shown in the equation below [80]:

$$T(\mathbf{x}) = T_\mu + \varepsilon(\mathbf{x}) + \varepsilon'(\mathbf{x}). \quad (2.1)$$

The spatially-correlated component is relevant in our study of SST variation as it can be interpreted as a measure of the spatial coherence of the SST heterogeneity. This random component can be assumed to be drawn from a distribution with zero mean and a covariance function given by:

$$C(\mathbf{h}) = E[\varepsilon(\mathbf{x})\varepsilon(\mathbf{x} + \mathbf{h})], \quad (2.2)$$

where  $\mathbf{x}$  is a measure of the distance metric of separation between the value of  $\mathbf{x}$  at one location and  $\mathbf{x}$  at another location (hereafter referred to as *lag distance*). For small lag distances ( $\mathbf{h}$ ), under the assumption of second-order stationarity, the

expected difference between the value of the random variable at one point ( $\mathbf{x}$ ) and ( $\mathbf{x} + \mathbf{h}$ ) would be zero [137], thus:

$$E[T(\mathbf{x}) - T(\mathbf{x} + \mathbf{h})] = 0. \quad (2.3)$$

Hence, the variance is given by:

$$\begin{aligned} \text{var}[T(\mathbf{x}) - T(\mathbf{x} + \mathbf{h})] &= E[\{T(\mathbf{x}) - T(\mathbf{x} + \mathbf{h})\}^2], \\ &= 2\gamma(\mathbf{h}), \end{aligned} \quad (2.4)$$

where  $\gamma(\mathbf{h})$  is called the semi-variance at lag  $\mathbf{h}$  [42].

The structure function of a 2D SST field is computed using the semi-variance  $\gamma(\mathbf{h})$  for every possible pair of data points separated by the particular lag vector  $\mathbf{h}$ ,  $m(\mathbf{h})$ :

$$\gamma(\mathbf{h}) = \frac{1}{2}E[\{T(\mathbf{x}) - T(\mathbf{x} + \mathbf{h})\}^2] = \frac{1}{2m(\mathbf{h})} \sum_{i=1}^{m(\mathbf{h})} \{T(\mathbf{x}) - T(\mathbf{x} + \mathbf{h})\}^2. \quad (2.5)$$

A plot of the structure function (variogram) computed from the observed data is called the experimental variogram, which can be fitted with known statistical models possessing particular properties (positive definiteness, continuity, differentiability, etc.) from which information about the field is extracted [95, 40].

The structure function has a general shape of increasing in value with lag distance until it plateaus at a value of semi-variance known as the *sill* for a given lag distance (*range*). The range is the lag distance at which the semi-variance is maximized (i.e., the lag distance at which point samples are completely uncorrelated), hence it is a measure of the length scale of spatial continuity seen in the 2D distribution of SST values. The structure function can be used to generate multiple realizations (simulations) of spatially-correlated 2D SST fields.

### 2.2.3 Structure function and spectral analysis of SST field.

The SST field is down-scaled to a 2 km resolution product (Fig. 2.2c) from which the first and second order moments (mean and variance) are extracted. The structure function (experimental variogram) is then calculated from the domain shown in Fig. 2.2c using Eqn. 5. The variogram is computed numerically over the domain using a bin size of 45 and a maximum lag of 560 km. SST follows a general trend of decrease in magnitude from the equator to the poles due to uneven solar radiation. However, following a similar rationale by [48], the size of the domain was chosen after manual investigation to minimize the inherent spatial heterogeneity associated with a latitude dependence of SST while preserving the spatial extent necessary for capturing the multiscale nature of SST anomalies (5–200 km). This choice also provides a justification for computing an omni-directional variogram which assumes an isotropic field (i.e., spatial continuity has no preferred direction/orientation). For larger domain sizes with inherent anisotropy, spatial continuity in preferred directions are often captured using directional variograms for the major axes (N-S and E-W). Furthermore, this study is focused more on the influence of the length scales of SST anomalies on the onset of RI, and not anisotropic effects. More information on the experimental variogram and anisotropic effects in the domain is detailed in appendix B.

The experimental variogram computed was then fitted with a common function known as the spherical model:

$$\gamma(h) = \begin{cases} c \left\{ \frac{3h}{2a} - \frac{1}{2} \left( \frac{h}{a} \right)^3 \right\} & \text{for } h \leq a, \\ c & \text{for } h > a, \end{cases} \quad (2.6)$$

where  $a$  is the range,  $c$  is the sill. The spherical model is chosen for use in this study because it is simple, ubiquitous in use in geostatistics, and known for ease of interpretation [40], not necessarily for any specific physical reason. For an ideal

case, this represents a function with a small value of semivariance at the origin representative of distances smaller than the sampling interval (2 km) or unresolved submesoscale (defined here as  $< 2$  km) variance  $c_0$ . This function then increases in value with increasing lag distance until it plateaus out for a lag distance  $h$  (the range), roughly representative of the maximum diameter of spatial continuity. The range represents the maximum length scale of continuity, corresponding in this study to SST anomalies of interest, e.g., ocean mesoscale eddies and cold wakes. The value of the semivariance  $c$  at the range represents the maximum variance in the 2D field. The experimental variogram was fitted using a theoretical spherical variogram with  $c_0 = 0.0$  °C<sup>2</sup>,  $c = 0.23$  °C<sup>2</sup> (variance of the 2D SST field) and a variable range corresponding to the chosen length scale of SST anomalies we wish to simulate.

A power spectral density (PSD) of the SST field (Fig. 2.3a) is computed from the 2D discrete Fourier transform of the SST fields. The amplitude of the Fourier spectrum is then computed for the norm of wave numbers ( $k$ -spatial frequency) which have been appropriately binned. A plot of the square of the Fourier amplitude against wave numbers gives the power spectral density and is indicative of the variance distribution at different wavenumbers (length scales) — this is shown in Fig. 2.3a. Figure 2.3a shows the PSD of the SST field, with the shaded area under the PSD curve indicative of the variance contribution by specific wavenumber ranges (horizontal scales; note that overlap of the colors at high wavenumbers is implied). The PSD curve is scaled by the area under the curve to extract the appropriate variance used in simulating the random SST fields shown in Fig. 2.4. Thus, spectral scaling allows the transfer of the appropriate variance contribution from the observed SST field to the simulated SST fields with different length scales.

Figure 2.3b shows the percentage contribution of different horizontal scales to the total variances seen in the SST field characteristic of when Irma underwent RI. We see clearly that most of the variance is contributed by large-scale SST anomalies (about

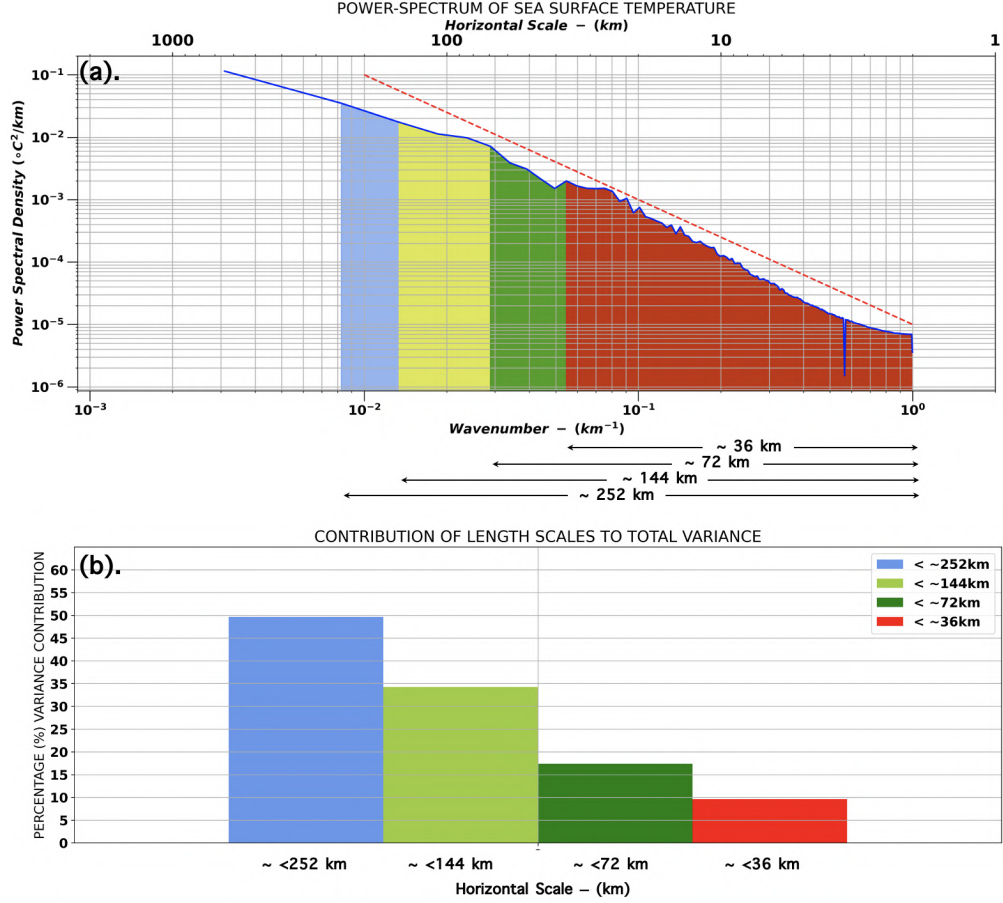


Figure 2.3. (a) 2D Power spectral density curve of the SST field shown in Fig. 2.2 (c), with the red line showing the  $7/5$  slope line. (b) Percentage variance contribution from different length scales; the full integral of panel (a) represents the total variance.

50% variance contribution from length scales of  $\leq 252$  km), while the least variance contribution is attributed to smaller scales (about 10.0% variance contribution from length scales of  $\leq 36$  km). This justifies our choice of scaling the variance in the simulated fields of different spatial scales generated (in section 2.2.4), despite the mean being kept constant. For completeness, we also later investigate the effect of using the same variance in generating the simulated fields (changing only the spatial scales).

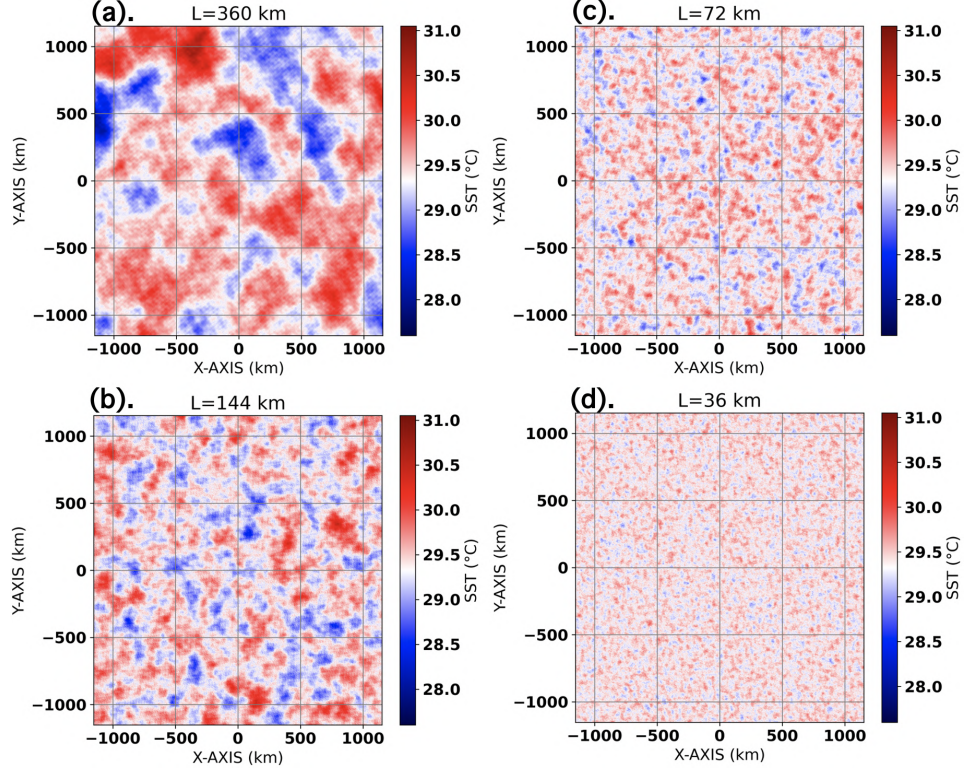


Figure 2.4. Sample of SST fields with length scales corresponding to (a) 360 km, (b) 144 km, (c) 72 km, (d) 36 km.

#### 2.2.4 Simulated sea surface temperature fields

We investigate the sensitivity of the RI onset timing to SST length scales by generating an ensemble of random fields with the same first and second order statistics (mean and variance) as the domain traversed by Hurricane Irma, as well as varying the length scale of spatial continuity (range) of the structure function used to generate the fields. With this, we are able to analyze multiple realizations of stationary, isotropic, Gaussian random fields generated with similar correlation structures as the parent field, only differing by the diameter of spatial coherence, indicative of characteristic sizes of SST anomalies. Sample synthetic fields are shown in Fig. 2.4.

Each realization of the random field generated represents one possible SST spatial distribution. As stated above, the assumptions of isotropy (that the SST fields do not

have any preferred direction of spatial continuity), weak stationarity (that the mean and variance of the SST fields do not vary with absolute location on the field but with lag distance alone), ergodicity (that the statistical moments of a single realization of the random field in space approach those of the ensemble as the regional boundaries tend to infinity [230]), and Gaussianity (that the random fields generated follows a normal distribution with known mean and variance) are made. The assumption of isotropy is justified for the small domain of interest as there is no observable latitude dependence of SST as would be expected for a larger domain. The assumption of Gaussianity is also justified as the distribution of SST in the parent domain is seen to follow a roughly normal distribution (Fig. 2.2d).

In addition to these assumptions, the spatial correlation of the fields are approximated using a spherical model as described in Sect. 2b and Eqn. 3 above. Recall that the range parameter ( $h$ ) controls the diameter of spatial continuity in this model; thus, we vary this parameter in generating the random SST fields to simulate specific sizes of SST anomalies observed in a typical hurricane environment. An ensemble of nine random fields are generated for each of four selected length scales (360 km, 144 km, 72 km and 36 km) corresponding to multiples of the initial RMW used in the subsequent simulated storms. Figure 2.4 shows a sample of one random field for each of the specified length scales, clearly illustrating a decrease in the length scale of SST anomalies and associated variance. Notice that the smallest length scale (36 km) SST field approaches a uniform field as the variations become almost indistinguishable at the scale of the figure.

### 2.2.5 Model Setup

The model used in this study is the CM1 model version 20.2.0 [22], which is a three-dimensional, non-hydrostatic solver. 36 sensitivity experiments (9 for each SST length scale) are performed using the SST fields generated above as lower surface

boundary conditions. The model intrinsic variability was obtained by initializing the simulation with random potential temperature perturbations of  $\pm 0.1$  K throughout the entire domain, also for an ensemble size of 9. The simulations are initialized using a modified Rankine vortex for a small sized storm (following the definition of TC size in [28]) with an initial RMW of 36 km and maximum tangential velocity ( $V_{\max}$ ) of  $10 \text{ m s}^{-1}$ . In order to further isolate the impact of length scales, the same set of experiments above are repeated but the variance for all SST fields (across different length scales) is kept constant, totalling 63 experiments. We note that using the same variance for SST fields having length scales ranging between 360km and 36km is physically unrealistic, as such sharp SST gradients between small perturbations are rarely observed in reality. Instead, these set of experiments are meant to untangle the interaction between SST variance magnitude and length scale, thereby strengthening our conclusions. In addition to these, a final set of experiments was carried out with a translating storm across the prescribed SST field. Table 1 below summarizes the experiment setup for each group of simulations.

Each experiment is run on a  $1152 \times 1152$  horizontal grid with uniform horizontal grid spacing of 2 km. The vertical grid has 59 levels and is stretched below 5500 m, with 50 m grid spacing near the surface to ensure the boundary layer is appropriately resolved. Above 5500 m, a constant vertical grid spacing of 500 m is used to the domain top at 25 km. The total size of the domain in the horizontal direction is approximately  $2300 \text{ km} \times 2300 \text{ km}$ . The simulations are set up on an  $f$  plane with Coriolis parameter of  $5 \times 10^{-5} \text{ s}^{-1}$ , using the Morrison double-moment microphysics scheme [148, 150], and the simple Louis-type planetary boundary layer (PBL) parameterization scheme [23] as a result of their simplicity and wide usage in TC modeling studies. All simulations were run with radiation turned off in order to isolate other complexities of TC dynamics, seeing that this study is focused on the impact of ocean conditions (specifically SST) and its effect on RI onset timing.

The simulations are broken into three specific numerical experiments as detailed below.

#### 2.2.5.1 Length scale experiment – A

The simulated TC is initialized using a modified Rankine vortex with an RMW of 36 km, and a maximum wind speed of  $10 \text{ m s}^{-1}$  decaying at a radial decay rate of 0.5 until 500 km (radius of zero wind). The vortex was initialized at the center of the domain, with no large-scale pressure gradient acceleration applied to the  $u$  and  $v$  components of velocity. Similarly, the vertical wind shear is zero for all simulations which allows a more conducive environment for rapid vortex spin up. The SST fields used in these experiments are the ensemble realizations noted above with varying length scales as shown in Fig. 2.4. The SST fields are time invariant for this set of experiments.

#### 2.2.5.2 Length scale experiment – B

The model setup for this set of experiments remains the same as the length scale experiment – A with a simple change in variance of the SST fields amongst the length scale ensemble. Instead of the observationally scaled variances (as in length scale experiment – A), these set of experiments use a fixed variance (corresponding to the variance of the 360 km length scale ensemble) for all SST fields generated. Thus SST fields with length scales of 36 km, 72 km and 144 km would have the same spatial variance as those of 360 km length scale. We note that this effectively implies an unrealistic sharp gradient between SST anomalies in the generated field (specifically in the smaller length scales). However, in combination with length scale experiment – A, this would further elucidate the dynamical response of RI onset timing to SST length scales apart from their magnitude.

TABLE 2.1

SUMMARY OF THE THREE GROUPS OF NUMERICAL  
EXPERIMENTS IN THIS STUDY

EXPERIMENT	MODEL SETUP	DESCRIPTION
<b>LENGTH SCALE EXPERIMENT – A</b>		
Sensitivity of RI onset to length scales of SST anomalies (realistic scaling of SST variance).	Initial RMW = 36 km Initial Vmax=10 m s <sup>-1</sup> $\Delta x = \Delta y = 2$ km (unstretched)	36 ensemble simulations using time-invariant SST fields with different length scales (36 km, 72 km, 144 km & 360 km).
<b>LENGTH SCALE EXPERIMENT – B</b>		
Sensitivity of RI onset to length scales of SST anomalies (constant SST variance across length scales).	Initial RMW = 36 km Initial Vmax=10 m s <sup>-1</sup> $\Delta x = \Delta y = 2$ km (unstretched)	27 new ensemble simulations using time-invariant SST fields with different length scales (36 km, 72 km & 144 km).
<b>TRANSLATION SPEED EXPERIMENT</b>		
Sensitivity of translating storms to length scales of SST anomalies	Initial RMW = 36 km Initial Vmax = 10 m s <sup>-1</sup> $\Delta x = \Delta y = 2$ km (unstretched)	18 ensemble simulations using time varying SST fields (with a length scale of 360km) with the storm translating from left to right at 2.5 m s <sup>-1</sup> (9 simulations) and 5.0 m s <sup>-1</sup> (9 simulations).

### 2.2.5.3 Translating storm experiment

For this set of experiments, unlike the stationary storm experiments above, the effects of storm translation are included to understand the influence of storm exposure to SST anomalies. This experiment uses two translation speeds of  $2.5 \text{ m s}^{-1}$  and  $5.0 \text{ m s}^{-1}$  (typical average translation speed for category 4-5 storms [138, 104]), to capture the effect of both realistic storm translation speed and slower-than-average storm translation speed. In order to minimize the influence of windshear and/or storm related environmental flow on eyewall symmetry, the translation was implemented by updating the lower boundary (SST fields) of the domain every model time step (Fig. 2.14). These experiments (using a storm initialized in the way as in experiments A and B above) translate from left to right across SST fields with a length scale of 360 km ( $10 \times$  initial RMW).

## 2.3 Results and Discussion

### 2.3.1 Evaluating the response of stationary storms to SST length scales

#### 2.3.1.1 Sensitivity of Modeled Storms to SST length scales

Figures 2.5a-d show plots of the intensity (in terms of  $V_{\max}$ ) of all ensemble members for SST length scales of 360 km, 144 km, 72 km and 36 km respectively, exhibiting differences in the spread of the onset timing of RI. From these plots, there is a clear influence of the length scales on the variance of RI onset time. It is worth noting that there is also a significant spread in the steady state intensity (particularly after 180 hrs) amongst the ensembles for each length scale. However, in this study, we are primarily concerned with the variance in RI onset timing (between 40 and 90 hours), hence most of our analyses are focused on this time span. Storms initialized over SST fields with a length scale of 360 km are seen to have a wider spread in RI onset compared to storms initialized over a 36 km length scale, suggesting a scale

dependence of variance in RI onset.

Figure 2.6a shows a plot of the maximum 10-m wind speed variance ( $\sigma_{V_{max}}^2$ ) amongst the ensemble simulations over time, with the black dashed line representing the model intrinsic variability and the solid lines representing different length scales. This figure shows that for all length scales (except 36 km and 72 km), the variances in the onset timing of RI is significantly higher than the intrinsic variability of the model. The maximum variance is seen between 40 – 90 h, which corresponds to the range of timing of RI amongst the ensemble members. The maximum variance during this period is associated with the largest length scale (360 km), and is seen to decrease for smaller length scales. Furthermore, the onset of the increase in variance appears earlier for larger length scales (360 km and 144 km). For smaller length scales, however, there is a delay in the timing of the increase in variance of maximum 10-m wind speed (by up to 10 h to 20 h - compared to the 360 km and 144 km length scale), suggesting a scale-dependent response of modeled storms to RI onset timing despite the domain mean SST staying roughly the same.

Figure 2.6b presents the variances in maximum 10-m wind speed against SST anomaly length scale at specified times within the observed range of rapid intensification (50, 60, 70 and 80 hrs) across the ensemble. From these, there is a noticeable steady increase in the variance of Vmax with length scale. This maximum in Vmax variance is consistent for all sampled times (360 km), decreasing for length scales. Minimum variance is seen for length scales smaller than  $2 \times$  the initial RMW of the storm. Figures 2.6a and b suggest an interesting dynamical response of the storm to SST anomalies having a length scale at least two times that of the initial storm size. To investigate this further, the SST fields corresponding to the ensemble members with the earliest and latest onset of RI (*Random SST<sub>1</sub>* and *Random SST<sub>8</sub>*) are closely examined in Fig. 2.7. Figures 2.7a-d show the SST fields associated with these end members overlain by the initial RMW. These SST fields represent the

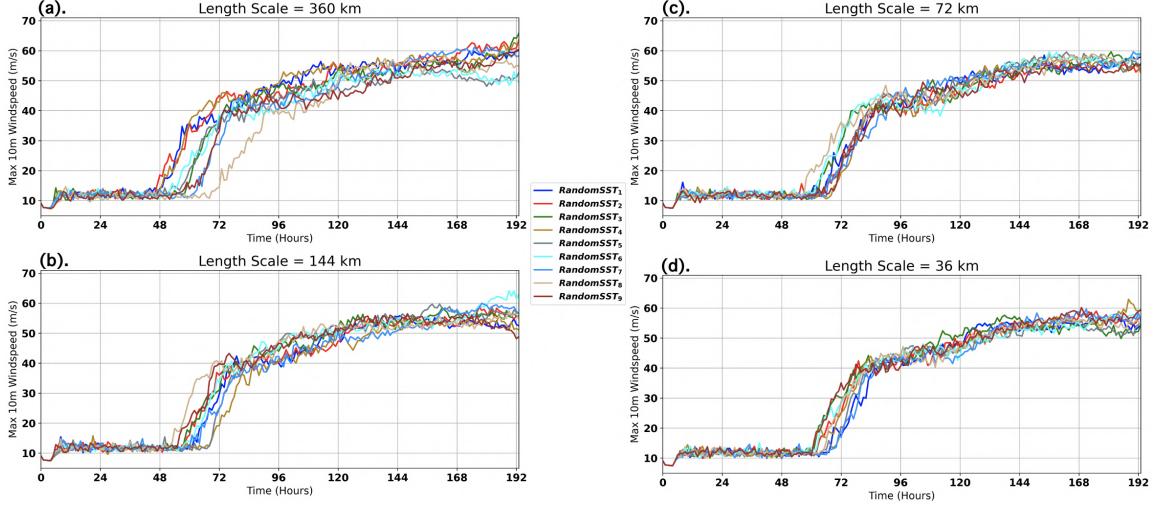


Figure 2.5. Intensity plots of modeled storms with initial RMW of 36 km using ensemble SST random fields with length scales of (a) 360 km, (b) 144 km, (c) 72 km, and (d) 36 km.

lower boundary conditions experienced by the storms simulated in Fig. 2.5a above (shown by the blue and light-gold solid lines respectively). From this, it is seen that the magnitude and size of SST anomalies underneath the eye/eyewall plays a crucial role in modulating the timing of RI onset, as might be expected, with warmer SST anomalies within the RMW (Fig. 2.7a and b, blue line in Fig. 2.5a) leading to the storm intensifying about 20 hrs earlier than cold SST anomalies (Fig. 2.7c and d, light-gold line plot in Fig. 2.5a).

A visual comparison of convective structures of all simulated storms at day 3 is shown in Fig. 2.8, indicating the simulated reflectivity at 1 km height (zoomed to a 200 km square domain) for all nine ensemble members with an SST length scales of 36 km, 72 km, 144km and 360 km. From the last column, there are clear differences in the convective structure and eyewall formation for simulations using different SST fields with the same length scale of spatial continuity. Members 1 and 8 of the last column in Fig. 2.8 show the reflectivity signatures for the storms initialized over the

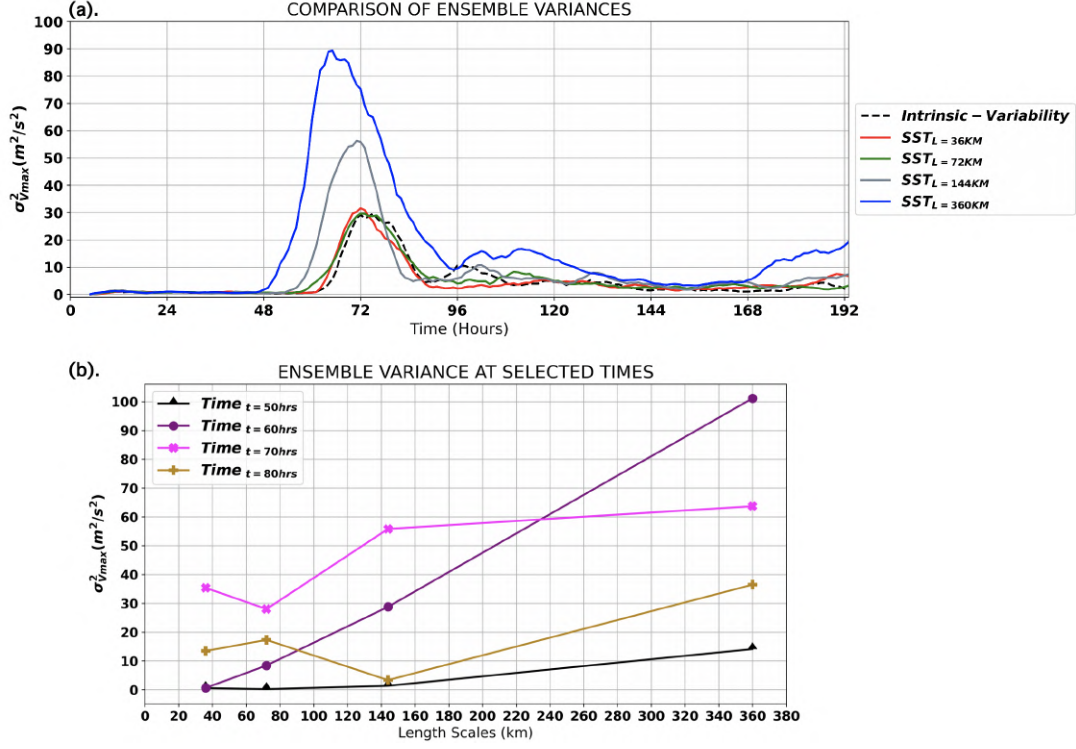


Figure 2.6. (a) Variance of maximum 10-m wind speed against integration time for selected length scale simulations (solid lines) and intrinsic variability of model (dashed black line). (b) Variance of maximum 10-m wind speed for different length scales during selected times corresponding to intensification (50 hrs - black line, 60 hrs - purple line, 70 hrs - magenta line) and post intensification (80 hrs - golden line), showing a variance peak for a length scale of 360 km.

relatively warm and cool SST anomaly referred to in Fig. 2.7, clearly illustrating the distinct eye formation for the former and the scattered/unorganized convection in the latter. It is clear that the magnitude and size of the SST anomaly underneath the eye/eyewall of the storm significantly influences the convective structure and eyewall formation, which consequently affects the timing of the onset of RI. Furthermore, the variance in the mesoscale and convective structures of the storms is seen to increase progressively as the length scales increase up until the maximum at 360 km (last column). The convective structures in the last column (360 km length scale) display,

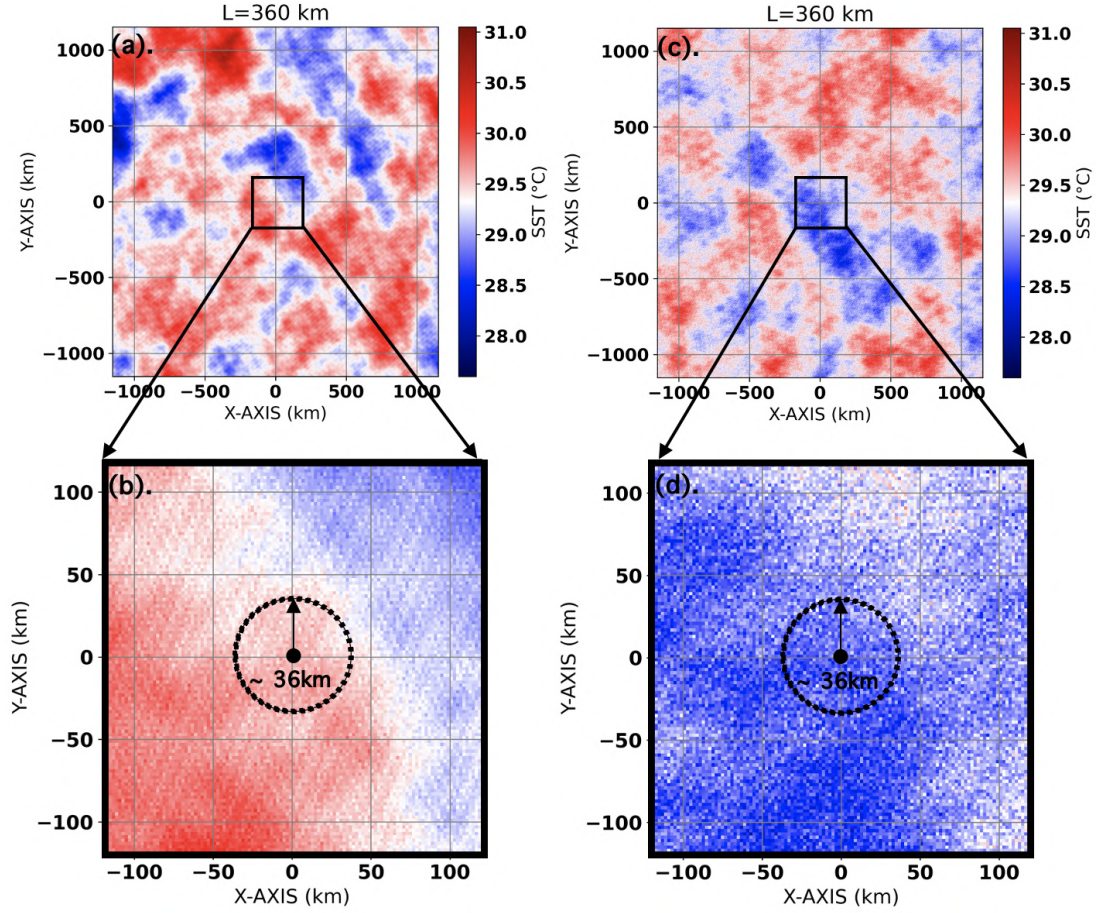


Figure 2.7. SST distribution for the ensemble members with (a) delayed RI, (c) early RI. Panels (b) and (d) show a closer view of the SST near the domain center with the initial RMW of 36 km overlaid, corresponding to *Random SST<sub>1</sub>* and *Random SST<sub>8</sub>* respectively in Fig. 2.5a.

qualitatively speaking, a significant variance amongst ensemble members as seen in Fig. 2.8, with member 8 showing unorganized convection with a poorly organized eyewall, uncharacteristic of strong storms. Ensemble members 1, 2 and 4 show well-organized, closed convective structures around the eye, indicative of an intensifying or already-strong storm. An opposite structural variance is seen in the first column (36 km length scale), with all ensemble members (except for 3 and 6) showing an equally weakly-organized convective structures. The physical processes underlying the variance in convective structures seen across ensemble members at varying length

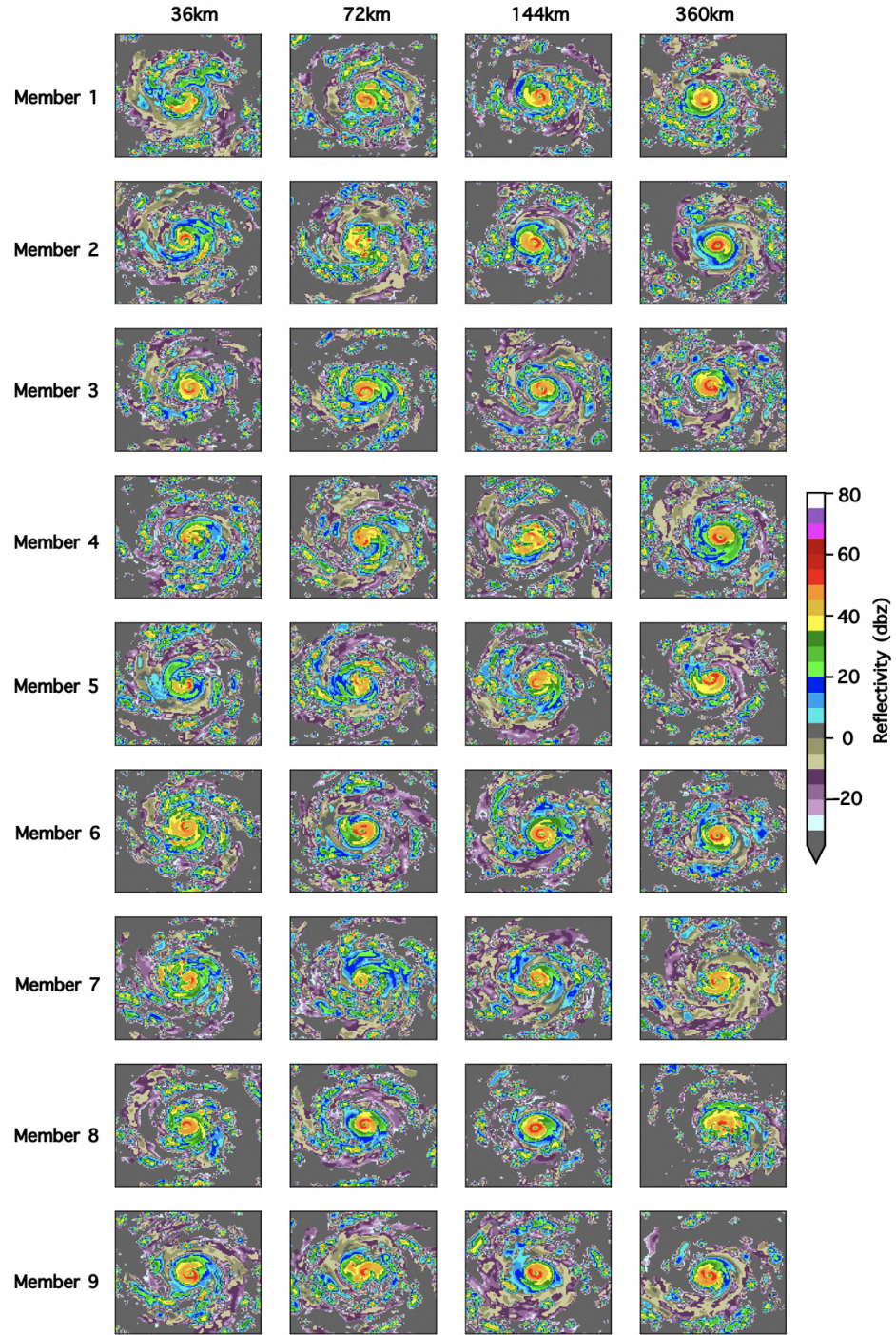


Figure 2.8. Ensemble plots of reflectivity (at 1 km height) on model day 3 for length scales of 36 km (first column), 72 km (second column), 144 km (third column) and 360 km (fourth column).

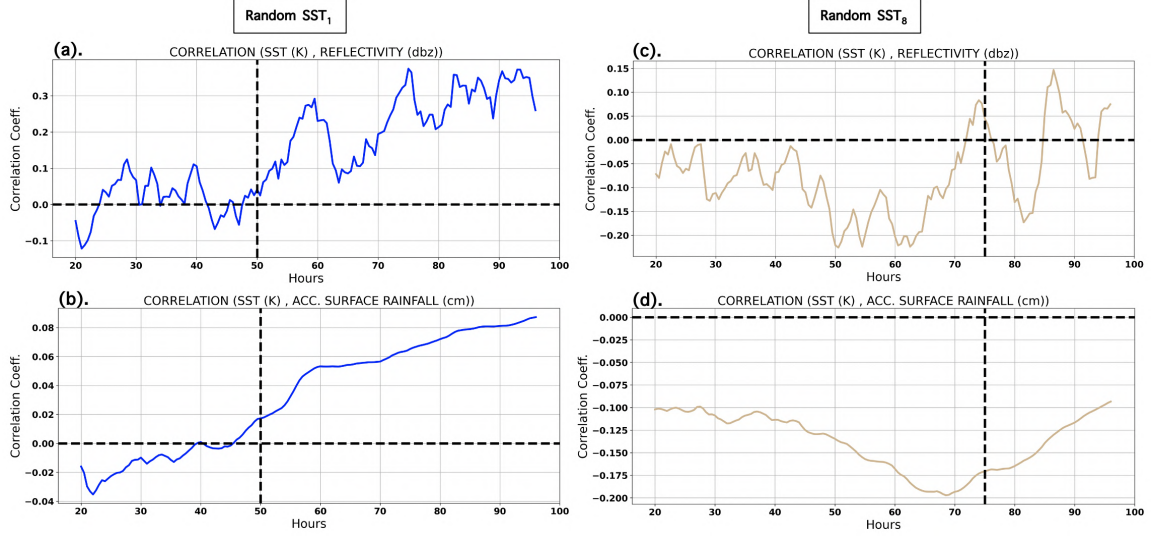


Figure 2.9. Plots of spatial correlation coefficient between SST & reflectivity (at 1km altitude) and SST & surface accumulated rainfall at for *Random SST<sub>1</sub>* and *Random SST<sub>8</sub>* shown in Fig. 2.11b and f respectively. The dashed vertical line shows the timing of RI onset for both simulations.

scales is explored in the following subsections.

To better quantify the preferential convective asymmetries induced by the SST anomalies about the storm RMW, plots of the Pearson's correlation coefficient between both SST and reflectivity as well as SST and surface accumulated rainfall are shown in Fig. 2.9. This was computed from the values of relevant variables (SST, reflectivity and surface accumulated rainfall) at each grid point spanning  $\approx 200\text{km} \times 200\text{km}$  square domain around the domain center, where the storm was initialized (shown in Fig. 2.7b and d). Figures 2.9a - d show time series between 20hrs (well after model spinup) and 100hrs (after RI), capturing the evolution of the relationships between SST and reflectivity as well as SST and total surface accumulated rainfall (where the vertical dashed line indicates the onset of RI and the horizontal dashed line indicates the zero correlation line). There is a distinct relationship between convective development and the distribution of SST, depicted by the non-zero

correlation coefficients. The case with the fastest RI onset,  $SST_1$ , shows a strong positive correlation as RI occurs and continues, with the same pattern seen in the correlation between SST and the surface rainfall. The case with the most delayed RI onset,  $SST_8$ , shows a generally weaker, but negative correlation, particularly in the hours leading up to RI.

### 2.3.1.2 Isolating the contribution of SST length scales

As introduced in model setup, the core strategy behind our approach is to explore realistic SST anomalies on storm RI, using a spatial stochastic process whose properties are a function of an observed parent field (in our case Hurricane Irma). According to observations, the variance of the SST anomalies is directly linked to their spatial size, as one might expect (Fig. 2.3). This raises the question, however, or whether the modification in RI onset timing seen in the previous section is due solely to the spatial extent and juxtaposition of the SST patches with the initial storm core (i.e., their size), or whether it is the magnitude of the SST anomalies that is the main contributor to the trends seen in RI timing (Fig. 2.6). Length scale experiment – B is designed to answer this question. Unlike length scale experiment – A described above, the ensembles for all length scales have the same SST variance, corresponding to the variance used in the 360 km field ( $0.114^{\circ}\text{C}^2$ ). With this analyses, we can isolate the impact of the spatial extent of SST anomalies versus their magnitude on the variance in RI onset timing.

Figure 2.10 presents a plot of the variance of maximum 10m windspeed (for length scale experiment – B) amongst the ensembles. Comparing Fig. 2.10 to Fig. 2.6a, we note that the impact of a constant variance in the ensemble SST field realization is primarily to increase the magnitude of the variance seen in RI onset timing for length scales of 144 km and 72km. This is somewhat unsurprising as we expect that using the exact same variance of the 360 km ensemble on the 144 km and 72 km fields

would result in the subsequent fields having sharper gradients between anomalies, and allowing an initial vortex to be positioned over relatively larger and smaller SST anomalies. Interestingly, this increase in SST variance has no effect on the magnitude of variance in RI onset amongst the 36km length scale ensemble. This suggests that below a certain length scale (36 km in this case), an increase in the variance of the SST field realization has no effect on RI onset timing (compare red lines in both Fig. 2.10 and Fig. 2.6a to the intrinsic variability).

In addition to results from Length scale experiment – A, Length scale experiment – B supports our hypothesis that SST length scales indeed does affect the variance in RI onset timing. This test shows that while the variance of the SST patches has a quantitative impact on the RI timing, it is the size that controls when the storm can respond. Thus for the remainder of this paper we continue to use the realistic SST variance-size relationship.

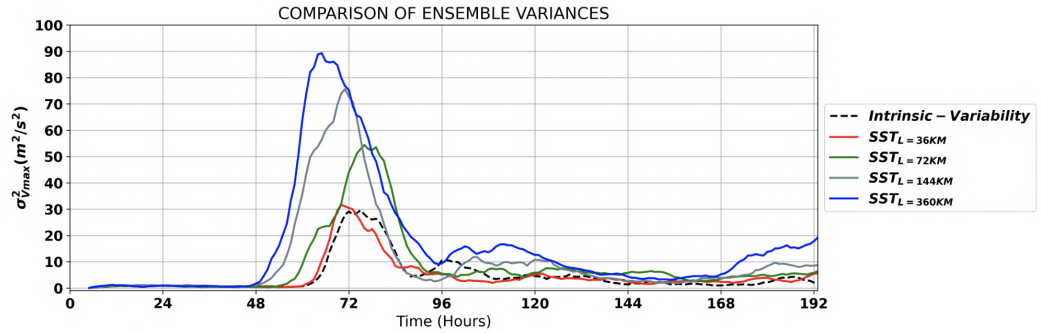


Figure 2.10. Same as Fig. 2.6a but using constant variance in SST fields.

### 2.3.1.3 The Influence of Scale-Induced Convective Asymmetries on RI Onset Timing

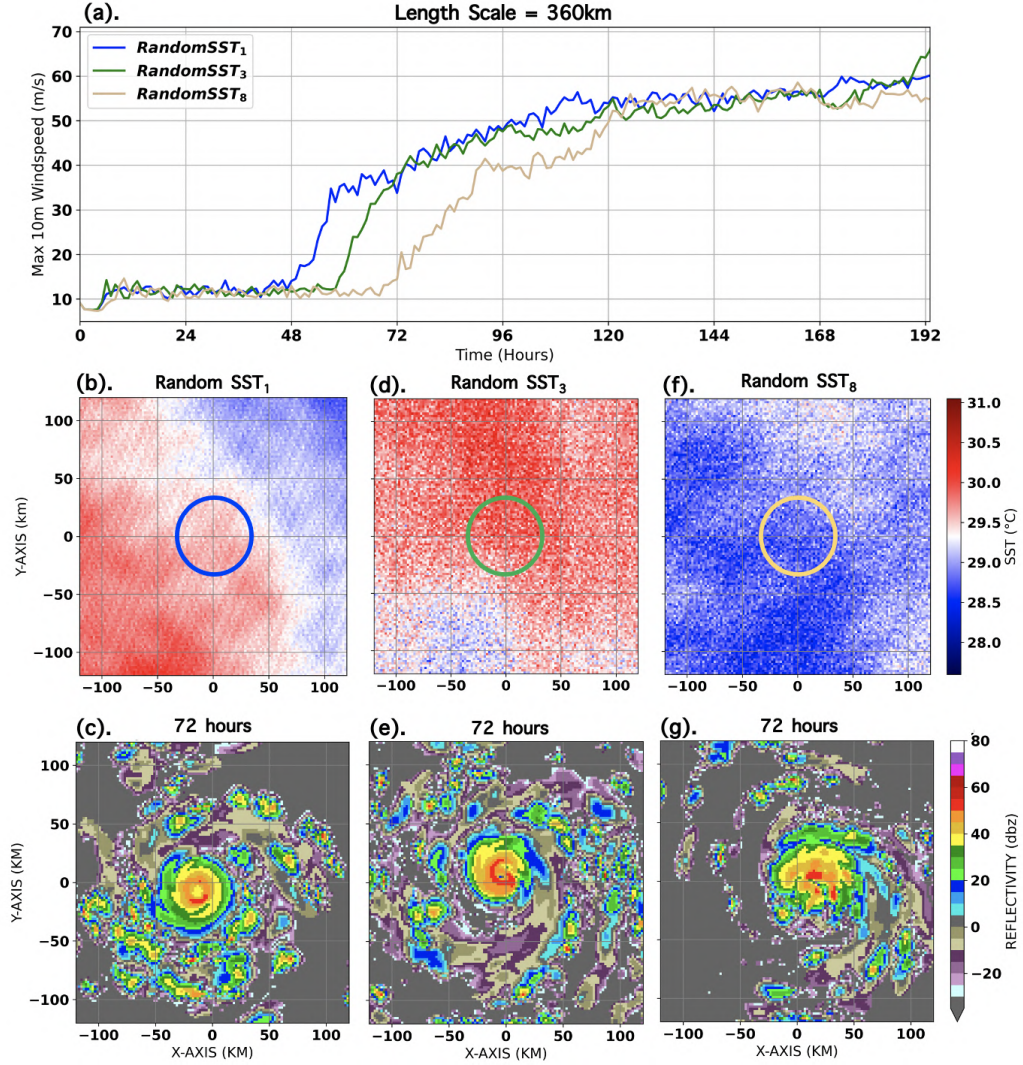


Figure 2.11. (a) Intensity plots of three selected simulations (*Random SST<sub>1</sub>*, *Random SST<sub>3</sub>* and *Random SST<sub>8</sub>*) with a length scale of 360 km, (b – d – f) Time-invariant SST fields for the selected three simulations shown in (a), (c – e – f) Simulated radar reflectivity at 72 hours for the selected three simulations shown in (a).

In this section, we address the dynamical pathways to intensification followed by the end members observed in Fig. 2.5, since these pathways are representative of the large variance in RI onset amongst ensemble members. Asymmetries in convection around the eyewall have been shown to influence intensification of TCs [144, 159, 133] depending on the spatial location and radial coverage of associated convective bursts (CB) relative to the TC eye, doing so by affecting the distribution of diabatic heating in the eyewall [10, 179, 219, 163]. Warm SST enhances the formation of these convective systems, hence a scale-dependent distribution of SST anomalies could induce preferential spatial distribution of convection, leading to asymmetries in convection close to the storm.

Figure 2.11a shows the end members (blue and light-gold solid lines) for simulations with SST length scale of 360 km that exhibit a delay of about 24 hrs between them. These ensemble members differ only by the spatial distribution of SST anomalies within the domain as seen in Fig. 2.11b-d-f. From Fig. 2.11c-e-g, there is a noticeable collocation of the 1 km simulated reflectivity signatures at 72 hrs in regions with relatively warmer SSTs (Fig. 2.11b-d-f). A comparison of Fig. 2.11b and c & Fig. 2.11f and g shows a relatively suppressed spatial distribution of convection in the S-W quadrant for the latter, with convection dominantly located towards the N-E quadrant where the SST progressively gets warmer. A similar pattern is visible in the former (Fig. 2.11b and c) where the N-E quadrant lacks as much convective clusters as the S-W quadrant. This suggests that the SST length scale can play an important role in the organization of convection around the storm center, with preferential development of convection over warmer SSTs leading to asymmetries in convective development. This variation in convective organization ultimately results in variance in the onset timing of RI as seen in seen in Fig. 2.11a.

Previous work [37, 117, 96, 108] has shown that warm SSTs underneath the eye/eyewall can play an important role in TC intensification. The results in Fig.

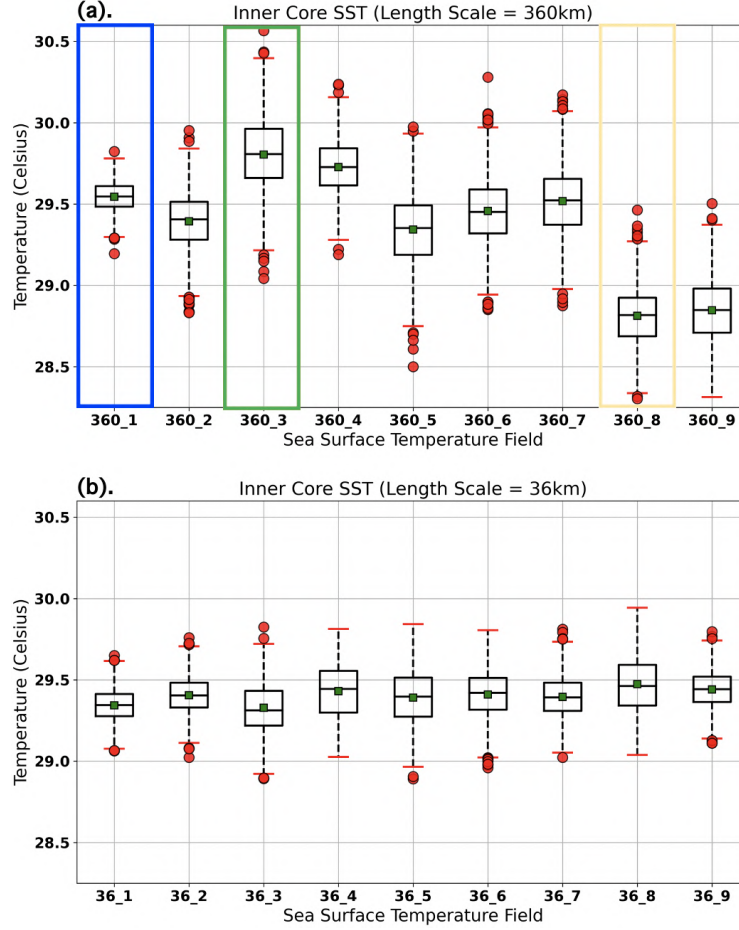


Figure 2.12. Box and whisker plots of SST values (for (a) 360 km and (b) 36 km length scale) within a 36 km radius beneath the domain center where the storm vortex was initialized. The nine box and whisker plots in each panel are for the nine ensemble members for each SST anomaly size.

2.11 suggest that a comparatively warmer SST in the inner core is a necessary but not sufficient condition to guarantee an earlier RI onset. To better quantify this, Figs. 2.12a and b present box and whisker plots of SST within a 36 km radius of the domain center for SST lengths scales of 360 km and 36km, respectively. These figures highlight a significant variance in SST for length scales of 360 km compared to length scales of 36 km. The highlighted box plots in Fig. 2.12a correspond to ensemble members *Random SST*<sub>1</sub>, *Random SST*<sub>3</sub> and *Random SST*<sub>8</sub> from Fig. 2.11.

The box plots demonstrate that a higher mean SST (indicated by the green marker in Fig. 2.12) within the radius of maximum wind for *Random SST*<sub>3</sub> did not necessarily lead to an earlier intensification compared to *Random SST*<sub>1</sub> with a lower mean SST. Although the strong link between SST in the eye-eyewall region and storm intensification [37, 220] is supported by our findings (*Random SST*<sub>1</sub>/*Random SST*<sub>8</sub> in Fig. 2.12 and the blue/light-gold lines in Fig. 2.11a), our results also suggest that this can be modulated by spatial heterogeneity in SSTs leading to asymmetry in convective development, which impacts subsequent intensification (Fig. 2.11b).

Comparing Figs. 2.5a & 2.12a to Figs. 2.5d & 2.12b, it is clear that the variance in SST, and not necessarily its mean value, at the core of the storm domain influences the variance in RI onset of the modeled storm. As the length scales of SST anomalies decrease from 360 km to 36 km, so does the propensity for convective asymmetries induced by the larger length scales, as can be seen in Fig. 2.8. This suggests that larger length scales of SST heterogeneities have sufficient extent to create asymmetries in convection that can influence RI onset, unlike at smaller SST length scales where the limited spatial extent of the SST anomalies is unable to induce coherent asymmetries in convection via preferential convective development over areas of higher SST. Hence, azimuthal asymmetry in convection occurring with larger SST length scales, as a result of strong asymmetry in SST around the eyewall, acts to influence RI consistent with the study by Martinez et al. [133].

To further investigate the symmetry of storm structure and possible relations to the intensification pathways shown in Fig. 2.11, we compare the azimuthally averaged vertical velocity for *Random SST*<sub>1</sub>, *Random SST*<sub>3</sub>, *Random SST*<sub>8</sub> respectively (Fig. 2.11) in Fig. 2.13. Comparing the first and third row in Fig. 2.13 (*Random SST*<sub>1</sub> and *Random SST*<sub>8</sub> respectively), we note that the storm initialized over a relatively warm SST anomaly (*Random SST*<sub>1</sub>) forms a distinct symmetric eye structure much earlier (60h), compared to the storm initialized over a relatively colder SST anomaly

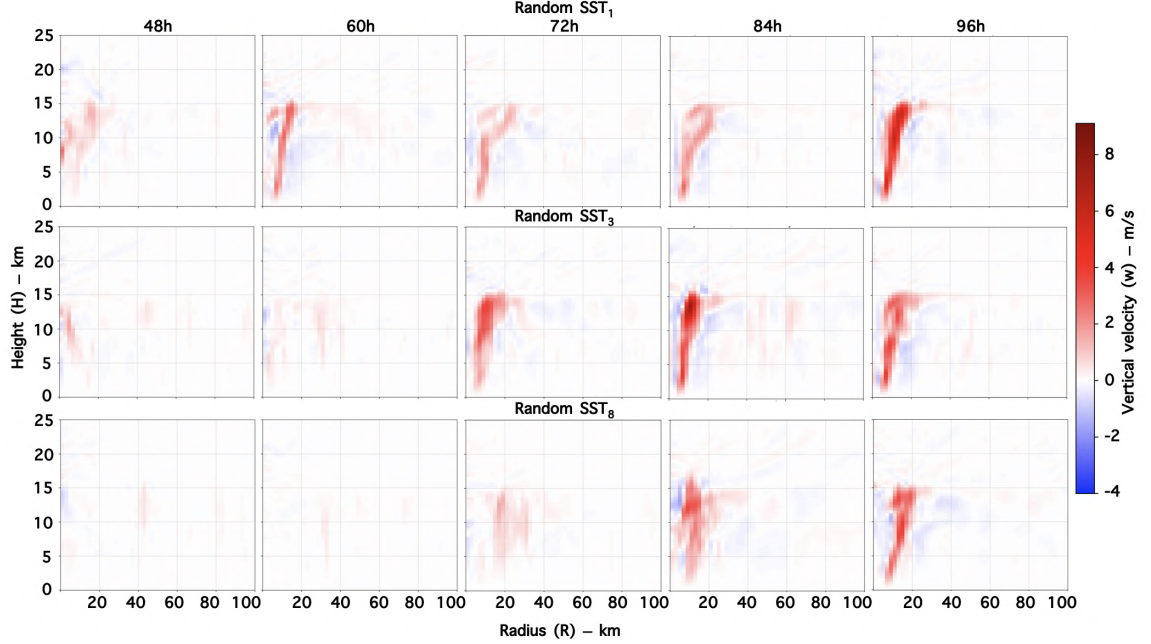


Figure 2.13. Azimuthally averaged vertical velocity ( $\text{m s}^{-1}$ ) from 48 - 96hrs (RI phase) for  $\text{RandomSST}_1$ ,  $\text{RandomSST}_3$  and  $\text{RandomSST}_8$  shown in Fig. 2.11.

( $\text{Random SST}_8$ ) as seen in Fig. 2.11. This symmetric eyewall supports the rapid intensification process of the modeled storm as seen in previous literature. Comparing the first and second row in Fig. 2.13 ( $\text{Random SST}_1$  and  $\text{Random SST}_3$  respectively), we note that even though the latter was initialized over SST conditions with high mean value (Fig. 2.11d and Fig. 2.12a), there is a noticeable delay in the timing of symmetric eyewall formation (72 hours compared to 60 hours for the former). Figures 2.11c and e again support this notion, with the  $\text{Random SST}_1$  showing a clear symmetric eyewall structure compared to  $\text{Random SST}_3$ . Interestingly, we note that despite the delayed RI, strength of eyewall symmetry is higher for  $\text{Random SST}_3$  than in  $\text{Random SST}_8$  as seen in Fig. 2.13. This suggests that the mean SST in the core most certainly influences storm intensity, however it may not be the dominant determining factor in RI onset timing.

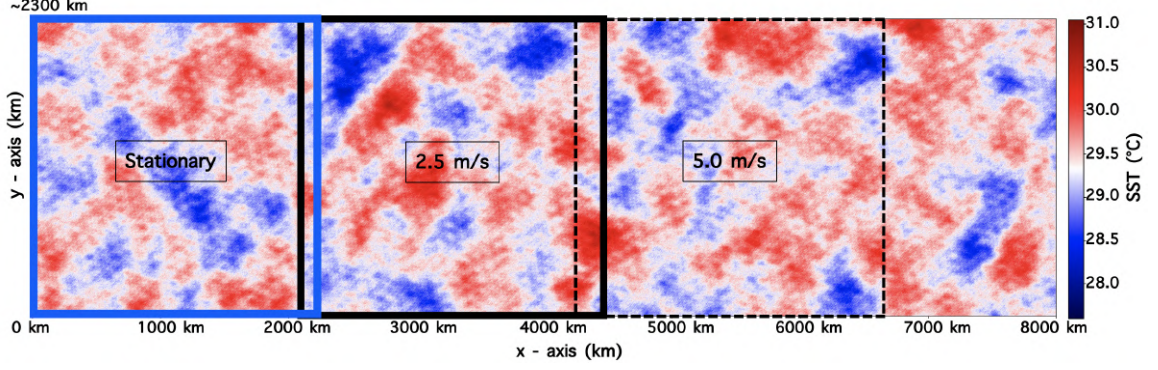


Figure 2.14. Illustration of the start (solid blue box) and end location of storms translating at  $2.5 \text{ m s}^{-1}$  and  $5.0 \text{ m s}^{-1}$  (solid and dashed black boxes respectively) over an SST field with length scale = 360 km for 10 days (zoomed view of stationary case shown in Fig. 2.11f).

### 2.3.2 Investigating the effect of storm translation speed on the variance in RI onset timing

Previous work focused on the interaction between a translating storm and the SST suggests that slower moving storms constrain their intensification pathway by prolonged exposure time to the self-induced cooler SST anomaly underneath the eye/eyewall itself, caused by upwelling and upper ocean mixing [169, 115]. Lin et al. [115] concluded that a typical translation speed of  $7 - 8 \text{ m s}^{-1}$  was sufficiently high to allow intensification up to category 5 given a shallow warm layer beneath, while slower translating storms (e.g., with translation speeds of  $2 - 3 \text{ m s}^{-1}$ ) require a much deeper warm upper ocean layer to reach the same intensity.

In this section, we investigate the influence of various translation speeds on the variance in RI onset timing using a suite of uncoupled simulations with varying SST length scales. Unlike the time-invariant SST experiments in Section 32.3.1 above (which were intended to isolate the contribution of the SST length scales to the variance in RI onset timing based on the storm's dynamical response to the underlying

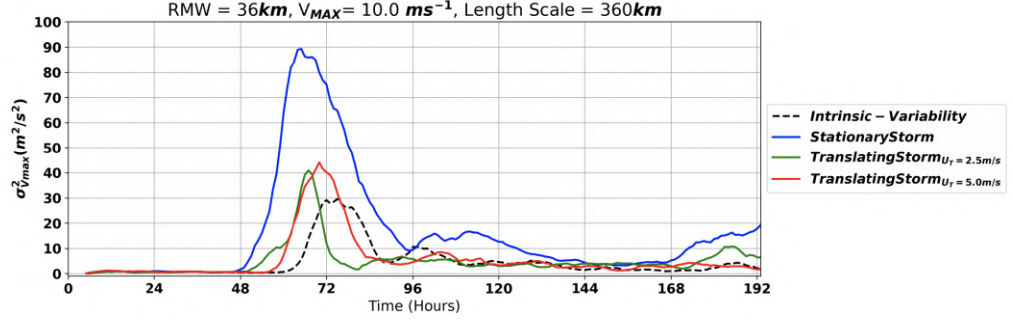


Figure 2.15. Line plots of variance in maximum 10-m wind speed amongst ensemble simulations for a stationary storm (solid blue line),  $2.5 \text{ m s}^{-1}$  translation speed (solid green line) and  $5.0 \text{ m s}^{-1}$  translation speed (solid red line), intrinsic variability (dashed black line). Experiments are for small sized storm (RMW = 36 km) translating over SST anomalies with a length scale of 360 km.

SST patterns), this section explores the role of the exposure time of modeled storms to changing length scales of SST anomalies.

Figure 2.14 provides a visual depiction of a sample storm translating from left to right at  $2.5 \text{ m s}^{-1}$  and  $5.0 \text{ m s}^{-1}$  across a domain with SST anomalies corresponding to a length scale equal to 360 km (*Random SST*<sub>8</sub> in Fig. 2.11). From Fig. 2.15, we see that storms translating at any speed ( $2.5 \text{ m s}^{-1}$  or  $5.0 \text{ m s}^{-1}$ ) have a generally lower variance in RI onset timing compared to stationary storm, and a higher variance compared to the model intrinsic variability — both behaviors are not unexpected. The magnitude of variance in RI onset timing is seen to be roughly the same between the  $2.5 \text{ m s}^{-1}$  translation speed to  $3.5 \text{ m s}^{-1}$  translation speed experiment. However, the variance in RI onset timing seems to occur a little earlier for the slowly translating storm ( $2.5 \text{ m s}^{-1}$ ), suggesting that the overall effect of storm translation is to reduce the time to the onset in variance in the timing of RI amongst ensembles. The effect on the magnitude of this variance is less clear.

To understand the dynamics at play here, we define a time scale  $\tau_e$ , characteristic

of the storm exposure time to SST anomalies of a given length scale ( $L$ ) and its initial RMW, given a translation speed ( $U_T$ ):

$$\tau_e = \frac{\sqrt{\frac{2 \times RMW \times L}{U_T^2}}}{3600}, \quad (2.7)$$

where  $\tau_e$  is the exposure time in hours.

Using the equation above, as expected, we see that the shortest exposure time ( $\tau_e = 8.9$  hrs) is attributed to the storm translating over SST fields with a length scale of 360km at the fastest translation speed ( $U_T = 5.0 \text{ m s}^{-1}$ ). On the other hand, the longest exposure time ( $\tau_e = 17.9$  hrs) is attributed to the storm translating at  $U_T = 2.5 \text{ m s}^{-1}$ .

Figure 2.15 suggests that for fast moving storms, shorter exposure times ( $\tau_e$ ) to SST anomalies delays the increase in  $\sigma_{V_{max}}^2$  as the storms have less time to adjust to the SST anomaly beneath. Thus, the stationary experiments have the highest variance in RI onset timing due to the fixed SST field beneath the storm initial location: extreme warm or cold SST anomalies can cause expedited or delayed RI (Fig. 2.11). On the other hand, all translating storms sample a range of SSTs during their lifetime, with fast translation speeds leading to reduced exposure time and lessening the impact of any single SST anomaly on storm development. In almost all cases, however, the variability is still larger than the intrinsic variability. In the limit of very fast translating storm translation, we would expect the solid lines in Fig. 2.15 to approach the model intrinsic variability (black dashed lines) since the model storm would never be able to adjust to the SST conditions beneath it before being exposed to new SST perturbations.

Figure 2.16 shows the 1 km reflectivity plot after 72 hrs for simulated storms translating at  $2.5 \text{ m s}^{-1}$  and  $5.0 \text{ m s}^{-1}$  across the domain. A comparison of Figs. 2.11c and 2.16a & b shows that convection is more symmetrically distributed about

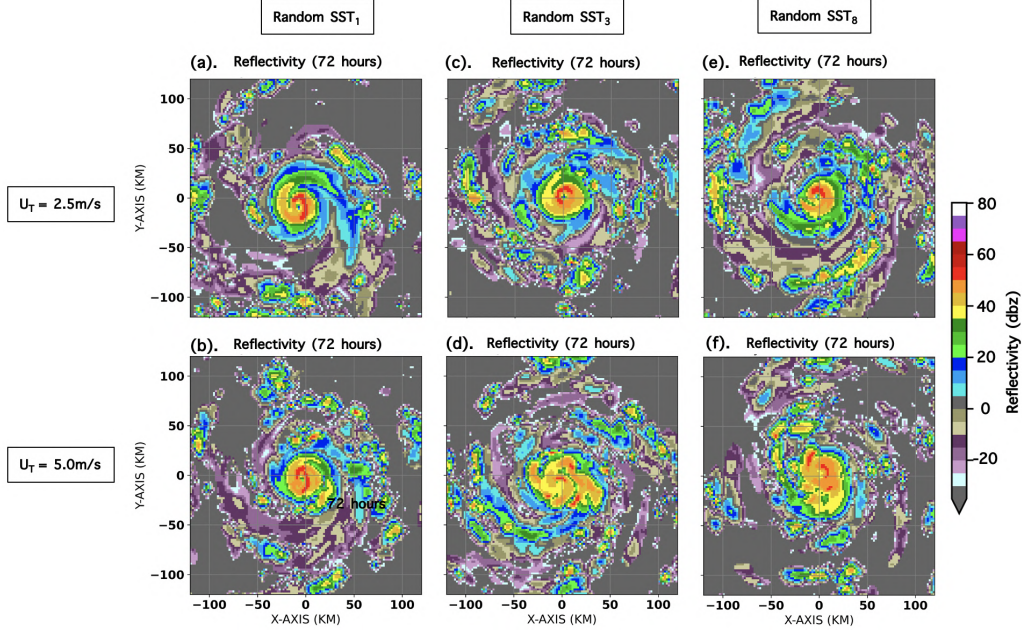


Figure 2.16. Same as Fig. 2.11 (c) - (e) - (g), but with the storm translating from left to right at  $2.5 \text{ m s}^{-1}$  and  $5.0 \text{ m s}^{-1}$ .

the storm translating at  $2.5 \text{ m s}^{-1}$  and  $5.0 \text{ m s}^{-1}$  across the domain across the domain. Similarly, comparing Figs. 2.11e and g to 2.16c and e, there is a significantly improved symmetricity of convection about the core of storms translating at  $2.5 \text{ m s}^{-1}$  compared to the stationary case. However, as the translation speed increases to  $5.0 \text{ m s}^{-1}$ , Figs. 2.16d and f shows a less symmetric eyewall structure with convection becoming less organized, suggesting that the storm structure (and by extension its intensity) does not respond linearly to increasing translation speed.

For *Random SST*<sub>8</sub>, the SST field shown in Fig. 2.14 provides more insight into the effect of storm translation over heterogeneous SST fields on eyewall symmetry and intensity. In this case, the stationary storm simulation has its core centered around a relatively cool SST anomaly, hence it forms the poorly organized eyewall convection seen in Fig. 2.11g at 72 hours. However, when this storm translates slowly at  $2.5 \text{ m s}^{-1}$ , it encounters mostly warm patches of SST anomaly, enhancing

convection and supporting eyewall symmetry. This, however, is not guaranteed for a faster translation speed ( $5.0 \text{ m s}^{-1}$ ), as it cuts across less warm anomalies. Thus, a translating storm interacting with alternating warm and cold patches of SST anomalies effectively feels the impact of the mean SST as it evolves, negating the impact of SST-induced convective asymmetries seen in the stationary case. However, the higher the translation speed, the higher the probability that the storm's core would encounter a drastically different SST conditions than where it started off. Furthermore, for the translating cases, the storm does not stay over a warm/cold patch long enough (i.e., shorter  $\tau_e$ ) to have its evolution significantly influenced by it. The variance amongst the ensemble simulations for a translating storm is thus seen to be consistently lower than that of the stationary experiments (albeit non-monotonically with the magnitude of storm translation speed), and is similar in magnitude to the stationary experiments with smaller length scales. This indicates that the net effect of a translating storm is analogous to that of reducing the SST length scale; i.e., reducing the variance in RI onset amongst the ensemble simulations by forcing an effective "mean" SST condition perceived by the evolving storm. Furthermore, we expect that for continuously increasing magnitudes of storm translation speed, the variance amongst the ensembles (red and green solid lines in Fig. 2.15) would collapse towards the model intrinsic variability (dashed black line).

Finally, a comparison of the last row in Figs. 2.13 and 2.17 illustrates the development of symmetry in vertical velocity evolving earlier for the translating storm compared to the stationary case, suggesting that delayed RI due to convective asymmetry seen in some of the stationary cases is counteracted by the translation of the storm across the domain. We note again, that (from Fig. 2.17), the storm translating at  $2.5 \text{ m s}^{-1}$  develops a more strongly symmetric eyewall structure (first row) compared to the storm translating at  $5.0 \text{ m s}^{-1}$  (first row), supporting the spatial reflectivity plots shown above in Fig. 2.16. Our hypothesis that storm translation

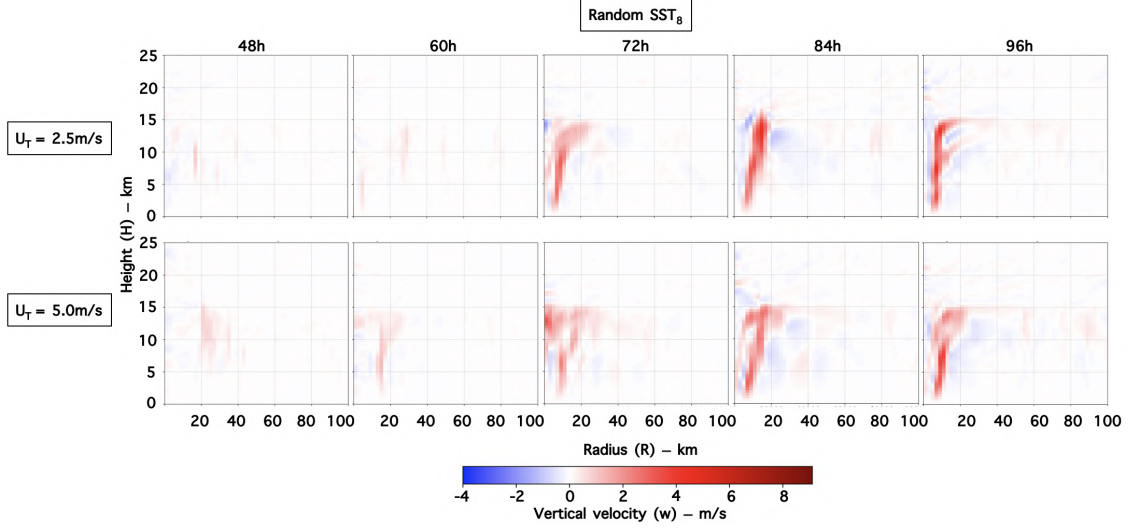


Figure 2.17. Same as the last row in Fig. 2.13, but for a storm translating from left to right at  $2.5 \text{ m s}^{-1}$  and  $5.0 \text{ m s}^{-1}$ .

induces an effective mean SST beneath the storm (thereby reducing asymmetries which negate RI onset) is supported by the intensity plot in Fig. 2.18 below, as we see that the same storm translating at  $2.5 \text{ m s}^{-1}$  intensifies roughly 10 - 15 hours earlier than when it is stationary. A closer look at Fig. 2.18 shows the storm with a slower translation speed of  $2.5 \text{ m s}^{-1}$  (solid black line) undergoing RI onset a few hours earlier than the storm with a faster translation speed of  $5.0 \text{ m s}^{-1}$ . As previously explained, this is most likely due to the fact that for this specific case, the eye of the former is exposed to warmer patches between its starting and end location (Fig. 2.14). Another potential reason for this could be the ease of symmetric eye formation for slowly translating storms ( $2.5 \text{ m s}^{-1}$ ).

## 2.4 Conclusions

Geospatial statistical techniques were used to generate multiple realizations of SST fields with realistic length scales characteristic of the SST conditions during hurricane Irma's (2017) rapid intensification. With these, we investigated the influ-

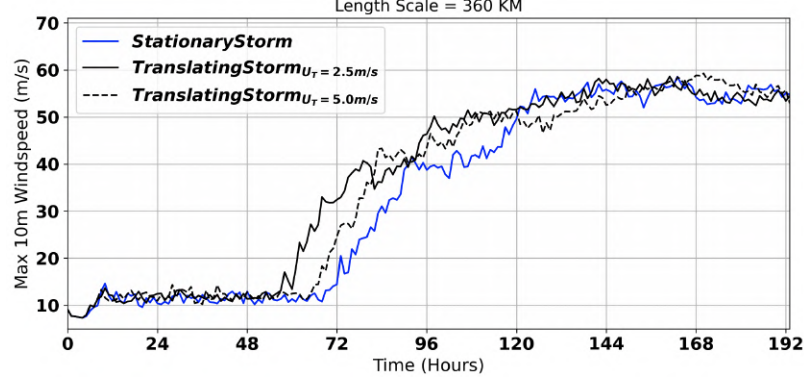


Figure 2.18. Comparing the intensity evolution of a stationary and translating storm, same as the golden line plot (*Random SST<sub>8</sub>*) in Fig. 2.11a but with plots of the effect of various translation speeds included as solid ( $2.5 \text{ m s}^{-1}$ ) and dashed ( $5.0 \text{ m s}^{-1}$ ) black lines.

ence of SST length scales on the variance in the timing of RI onset for stationary and translating storms. We ran a total of 90 simulations, comprising 36 suites of experiments with 9 ensemble members in each experiment, varying the length scale of SST heterogeneities and storm translation speed. This methodology allowed for a comprehensive study of the resulting variance in RI onset timing and the dynamics responsible for the different intensification pathways seen. Analyses of the variance in RI onset were based on the spatial distribution of SST and convection relative to the storm center, as well as the azimuthally averaged vertical velocity.

In agreement with previous studies, our results show that the magnitude of SST anomalies underneath the eye–eyewall region plays an important role in modulating the timing of the onset of RI. Beyond this, however, we find that SST anomalies with length scales exceeding the initial RMW induce asymmetries in convection which can act to delay RI despite the presence of favourable SST conditions within the eyewall, and despite the same domain-averaged mean SST. Furthermore, the reduced exposure time of a translating storm to SST anomalies of a prescribed length, compared to a stationary storm, is seen to modulate the effect of the SST anomalies on storm

development. At higher translation speeds, the storm feels the effect of a particular SST anomaly for a relatively short time, rather experiencing the effective mean SST conditions, akin to the small SST length scale experiments in Sect. 2.2.5.3b. Thus higher translation speeds reduce azimuthal asymmetries in convection by preventing the preferential development of convection over stationary warm SST anomalies, which removes a potential barrier to intensification.

An interplay between the above processes is seen to modulate the variance in RI onset timing amongst the ensemble members. Key findings from this study are summarized below:

1. For stationary storms in the presence of SST anomalies (Fig. 2.19a and b), we find that the magnitude of the SST anomaly underneath the eye-eyewall region alone does not control the RI regime seen in modeled storms. However, in addition to this, the length scale of these anomalies modulates the preferential distribution of convective development beyond the eyewall, creating asymmetries that significantly influence the timing of RI onset amongst the ensemble members. Smaller length scales lack the spatial extent to induce these convective asymmetries (Fig. 2.19a), hence ensembles in a small length scale field “feel” an effective mean SST.
2. The variance in RI onset timing amongst ensembles of translating experiments is seen to be lower than that of the stationary storm experiments, irrespective of the translation speed. Furthermore, we find that the storm exposure time to SST anomalies ( $\tau_e$ ), plays a crucial role in the dynamics seen for translating storms.
3. For translating storms in the presence of SST anomalies (Fig. 2.19c), the convective asymmetries induced in the stationary case (Fig. 2.19b) is minimal. This suggests that the net effect of translation over warm and cold patches is to reduce the variance in RI onset timing amongst ensembles by forcing the storm to experience a net “mean” SST analogous to the stationary case over small length scales of SST anomalies (as illustrated in Fig. 2.19a and c).

Figure 2.19 shows a conceptual framework of the key findings in this study, summarizing points 1 - 3 above. In agreement with previous work [144], our results demonstrate that pre-existing anomalies in underlying ocean conditions (in our case, SST perturbations) can have significant impacts for the intensification of tropical

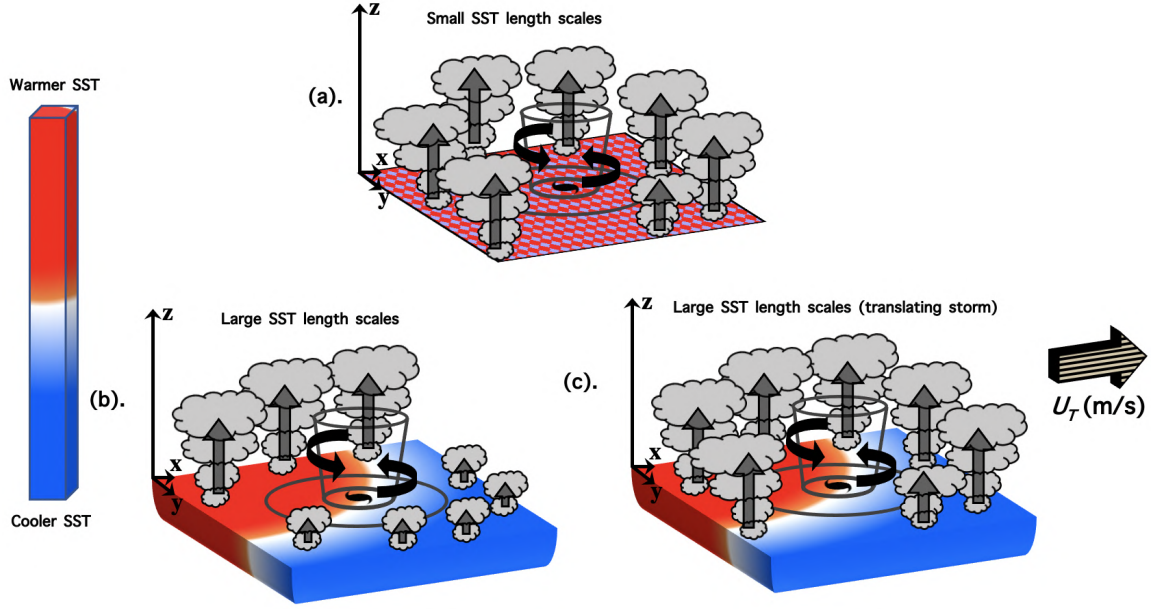


Figure 2.19. Schematics showing updraft and spatial distribution of convection and convective bursts induced by the magnitude of SST length scales for (a) Small length scales, (b) Larger length scales and (c) Larger length scales with a storm translating at  $U_T$ , relative to the storm center. The red and blue region represent relatively warmer and cooler SSTs.

cyclones through imposed convective asymmetries. The consequence of our findings for the predictability of TC RI is that storms encountering multiscale SST anomalies would have a variance in RI onset timing that would be higher for larger SST length scales (specifically those exceeding  $2 \times \text{RMW}$ ). The speed of TC translation reduces this variance and thus increases predictability but does not eliminate it. Thus, in favorable atmospheric conditions, RI predictability is highest in near-homogeneous SST conditions (in an uncoupled model) or for SST anomalies (or eddies) that are much less than mesoscale ( $\sim 100\text{km}$  or greater). One possible direct application of the findings from this study is the inclusion of horizontal gradient/length scales of SST anomalies in statistical-dynamical models which include SST as a predictor like the Statistical Hurricane Intensity Prediction Scheme (SHIPS) [45, 46] or SHIPS-RII.

Conclusively, this study shows that convective organization relative to the storm center can significantly influence intensification even in the presence of warm inner core SST conditions.

While this study details the importance of SST length scales in modulating RI onset timing, it is important to acknowledge that the use of an idealized model setup favourable for RI onset does not always represent realistic conditions in the TC environment. Limitations in the numerical setup used here include the exclusion of vertical wind shear, which if present can limit TC intensification through dry air intrusion into the core and vortex tilting [244, 61, 213, 9]. Furthermore, all simulations presented here are uncoupled (not including an ocean model or mixed layer model). Nevertheless, our results provide evidence for the importance of SST length scales on air–sea interaction and subsequent TC intensification, and this factor should be considered in ongoing efforts to understand the dynamics of RI and better predict it.

## 2.5 Acknowledgments

The authors would like to acknowledge George Bryan of the National Center for Atmospheric Research (NCAR) for making the model code (CM1) used in this study publicly available. We also acknowledge Drs. Steven Jayne and Elizabeth Sanabia for providing the ALAMO float dataset shown in this study. We acknowledge the ONR N00014-19-S-B001 grant for financial support under the Tropical Cyclone Rapid Intensification (TCRI) campaign. Computing and storage resources used for all simulations presented in this study were made available through the University of Notre Dame Center for Research Computing (CRC). We acknowledge useful conversations with Dr. David Nolan.

## CHAPTER 3

### THE ROLE OF TURBULENCE IN AN INTENSE TROPICAL CYCLONE: MOMENTUM DIFFUSION, EDDY VISCOSITIES, AND MIXING LENGTHS

The research in this chapter was carried out in collaboration with George H. Bryan, Richard Rotunno, Peter P. Sullivan, and David H. Richter. It has also been published in the Journal of the Atmospheric Sciences (<https://doi.org/10.1175/JAS-D-23-0209.1>).

#### 3.1 Introduction

Accurate prediction of hurricane intensity continues to lag behind track prediction [177, 47, 27], partly due to the lack of sufficiently high resolution spatio-temporal observations of small scale processes within the hurricane boundary layer (HBL) [250, 53], defined roughly as the first kilometer above the surface in TCs. Incomplete representation of turbulence and its various parameterized roles in numerical weather models may be a substantial source of hurricane-intensity forecast error, especially in the short time range (e.g., rapid intensification events). This is partly because turbulent fluxes in the hurricane boundary layer, which are mostly parameterized using schemes developed for non-hurricane wind conditions [34, 32], modulate enthalpy, moisture, and momentum exchange between the storm and the underlying ocean surface. Flight-level and ground-based observations of the near-eyewall region in intense hurricanes have alluded to the existence of organised turbulent structures in the hurricane boundary layer [147, 132, 3]. These structures, sometimes identified as coherent eddies [75, 171], tornado-scale vortices [237], mesovortices [105, 8],

or boundary-layer roll vortices [238, 151, 121, 64, 63] based on their sizes, orientation, intensity, and proximity to the eyewall [110], can have important implications ranging from modulating the severity of damage caused by hurricanes during landfall [237, 184] to endangering research flight missions [132, 251]. In addition, these structures could have significant influence on the magnitude of the fluxes in the HBL [151], thereby affecting the overall storm dynamics. Very few crewed aircraft missions have been able to observe these structures, especially within the intense turbulence regime of the hurricane inner eyewall. One such mission flown by the National Oceanic and Atmospheric Administration (NOAA) WP-3D research aircraft encountered a series of intense updrafts and downdrafts while penetrating the eyewall of Hurricane Hugo (1989) – a Category 5 storm – causing the loss of one of its four engines [136, 132]. Since then, small uncrewed aircraft system (sUAS) [38, 39, 7, 43, 191] and mobile Doppler radars [238, 103, 237] have been deployed within the inner eyewall region of intense hurricanes, in an attempt to safely understand the role of these structures in modulating the storm dynamics and the HBL in general.

The HBL has been previously shown to play an important role in mixing and energy transport which modulates the intensity of hurricanes [58, 23, 199, 21]. Using a series of numerical simulations, [21, 181] concluded that the parameterization of turbulence (in the horizontal direction) in the HBL substantially affects the maximum intensity of simulated storms. [178] showed that the turbulence kinetic energy (TKE) is maximized in the hurricane eyewall and “corner” region (where the mean flow changes from primarily horizontal towards the TC center, to primarily upward in the eyewall). These studies provide quantitative evidence for the inhomogeneous nature of hurricane turbulence. Furthermore, studies have shown a height- [26] and radius- [211] dependent transition from 3D to 2D turbulence in TCs, suggesting an inverse (upscale) energy cascade above  $\approx 150\text{m}$  in the TC boundary layer as well as in the inner-core region (i.e.,  $< 1.5 \times$  the radius of maximum winds). Since organized

turbulent structures are prevalent in the HBL, it is necessary to understand their characteristic scales and roles in flux/energy flow (into and away from the HBL) in order to understand the dynamics of intensity changes in hurricanes.

Although many important aspects of hurricane structure and behavior have been discovered using aircraft observations [1], the general distribution of turbulence in hurricanes has only recently been analyzed. [122] used airborne Doppler radar to provide, for the first time, the radial-height distribution of TKE in a number of hurricanes. *In situ* turbulence measurements [251, 248] have been used to estimate the eddy diffusivity in the hurricane boundary layer and eyewall. Although these particular measurements are more localized within the hurricane, they suggest that hurricane turbulence may be strongly anisotropic in that the horizontal diffusivity in the eyewall was found to be approximately an order of magnitude greater than the vertical diffusivity in the boundary layer. Using the Imaging Wind and Rain Airborne Profiler (IWRAP) with a horizontal and vertical resolution of 250m and 30m respectively, [75] documented that the most intense coherent eddy activities were preferentially located in the inner edge of the eyewall after the concentric eyewall replacement cycle stage of Hurricane Rita (2005), with typical radial wavelengths of  $\sim 1\text{--}3\text{km}$  and a depth of  $\sim 1.5\text{km}$ .

Numerical models have also been used extensively to study the evolution of the HBL and intensity changes in hurricanes. However, they are sensitive to the parameterization of turbulence, particularly that of horizontal turbulent diffusion [23, 181]. [183] pointed out the absence of any observational, experimental or theoretical basis for existing parameterizations of horizontal diffusion and promoted using the technique of large-eddy simulation (LES) for an idealized hurricane to obtain a physically based representation. In the years since that paper was published, there have been major advances in computer power and the use of LES for atmospheric applications [141]. With LES, the large energy-containing turbulent eddies responsible for most

of the energy production are explicitly resolved [as opposed to the planetary boundary layer (PBL) parameterization schemes used by traditional numerical weather prediction (NWP) models], while only small and much-less-energetic eddies are parameterized.

Using a horizontal grid interval of 100m in the innermost domain of the Weather Research and Forecast Large Eddy Simulation (WRF-LES), [254] analyzed the existence of the so-called coherent large eddy circulations (LECs) and concluded that they exist as well-defined updraft-downdraft couplets that enhance the exchange of energy, moisture and momentum. [92] identified the existence of small-scale coherent structures and three types of roll structures (depending on proximity to the hurricane eye), using the Japan Meteorological Agency Non-Hydrostatic Model (JMA-NHM) run at a horizontal grid interval of 100m. [235] and [236] identified tornado scale vortices (TSVs) in their 37-m WRF-LES simulations having a horizontal scale of  $\approx 1\text{km}$  with associated updrafts of  $>15\text{m/s}$ , occurring preferentially in the inner edge of the eyewall; they noted that each TSV comprised of a couplet of narrow intense updraft and a broad downdraft. Using a WRF-LES simulation with a 31-m grid interval, [29] simulated the evolution of Hurricane Irma (a Category 5 storm), showing that extreme wind gusts ( $\approx 132\text{m/s}$ ) were associated with multiple sub-tornadic scale vortices. [118] examined the relationship between tornado-scale vortices (TSVs) and enhanced surface wind gusts using a one-way nested WRF-LES simulation (with a horizontal grid interval of 37m in the innermost domain). Most recently, [110] characterized roll vortices and associated turbulent eddies aloft within a 20 – 40km radii of a simulated landfall of Hurricane Harvey (using data from a WRF-LES simulation with a 100-m grid interval), reporting a mean wavelength of 0.9 – 1.1km for turbulent eddies and 0.8km for roll vortices.

Clearly, understanding the prevalence and role of these coherent turbulent structures in the hurricane eyewall is not only pertinent to research flight safety, but also

to the understanding of heat, momentum and moisture flux which determines the bounds of storm intensity predictability [55, 84]. Most importantly, regarding HBL parameterizations, understanding the complex interaction among turbulent eddies of varying scales is a critical task in order to account for the net vertical fluxes which affect the storm. In the present study, LES of the inner core (i.e., eye, eyewall, and nearby rainbands) is utilized to characterize the behaviour of coherent turbulent eddies responsible for vertical and horizontal fluxes within a simulated Category 5 hurricane and their role in the budget of the mean wind field. Specific objectives of this study include:

1. Understanding the effects of turbulence on the mean wind field of an intense tropical cyclone.
2. Examining the validity of the widely used down-gradient eddy-viscosity hypothesis.
3. Analyzing the vertical and horizontal turbulence momentum fluxes in the TC boundary layer, with implications on effective eddy viscosity and mixing length, specifically in the highly turbulent eyewall region of the storm.

The remainder of this paper is organized as follows: Section 2 describes the LES modeling framework used in this study to investigate the existence of turbulence and coherent eddies in the HBL. Section 3 reports the major results of this study and these results are further discussed and summarized with concluding remarks in Section 4.

### 3.2 Simulation Methodology

This study uses the same simulation as in [232], Stern and Bryan [204], Stern et al. [206], and Richter et al. [173]. Specifically, Cloud Model 1 (CM1) [22, 23] was used to simulate an idealized Category 5 hurricane at turbulence-resolving horizontal and vertical grid intervals ( $\Delta x = \Delta y = 31.25\text{m}$ ,  $\Delta z = 15.625\text{m}$ ), utilizing the modeling framework described in [24]. The simulation, although idealized, was inspired by

Hurricane Felix (2007), which was a Category 5 storm with a comparatively small radius of maximum reflectivity of about 11 km [3].

Figure 3.1 summarizes the idealized hurricane LES setup, as also described in [24] for tornadoes. The three-dimensional model is initialized with output from an axisymmetric CM1 simulation, which in this case was run for 12 days until a quasi-steady state is reached. Time-averaged variables were then used to initialize the LES run. The initially axisymmetric eyewall convection quickly (within about 10 min) transforms into three-dimensional motion. The simulated storm takes roughly 1 h to adjust from the axisymmetric initial state with parameterized turbulence to a 3D flow with resolved turbulence; our analysis excludes this period of adjustment.

The 3D LES simulation was run for a total of 6 h, reaching a statistically steady state (defined below) after about 1 h of model integration. By design, the present idealized hurricane is statistically homogeneous in the azimuthal direction as the vortex is not translating relative to the lower boundary nor are the beta-effect or vertical wind shear included. The entire model domain spans  $3000\text{km} \times 3000\text{km} \times 25\text{km}$ , which is large enough to contain the full hurricane and its environment including the inner core and nearby rainbands. However, the LES subdomain is a smaller subset ( $80\text{km} \times 80\text{km} \times 3\text{km}$ ), which is large enough to produce turbulence from the eye to about 3 times the radius of maximum winds. Within the inner LES subdomain, a constant grid interval of 31.25m and 15.625 m is used in the horizontal and vertical respectively. For the subgrid turbulence within the fine-mesh domain, a two-part subgrid-scale turbulent kinetic energy (TKE) model based on the Deardorff TKE scheme is used [44, 25]. Outside of the fine-mesh LES domain, where turbulence is parameterized using the Louis PBL scheme [123, 100], the stretched horizontal grid reaches 15km grid spacing at the edge of the domain, while the vertical grid spacing stretches to 500m at 8km height, staying constant at 500m up to the top of the model domain.

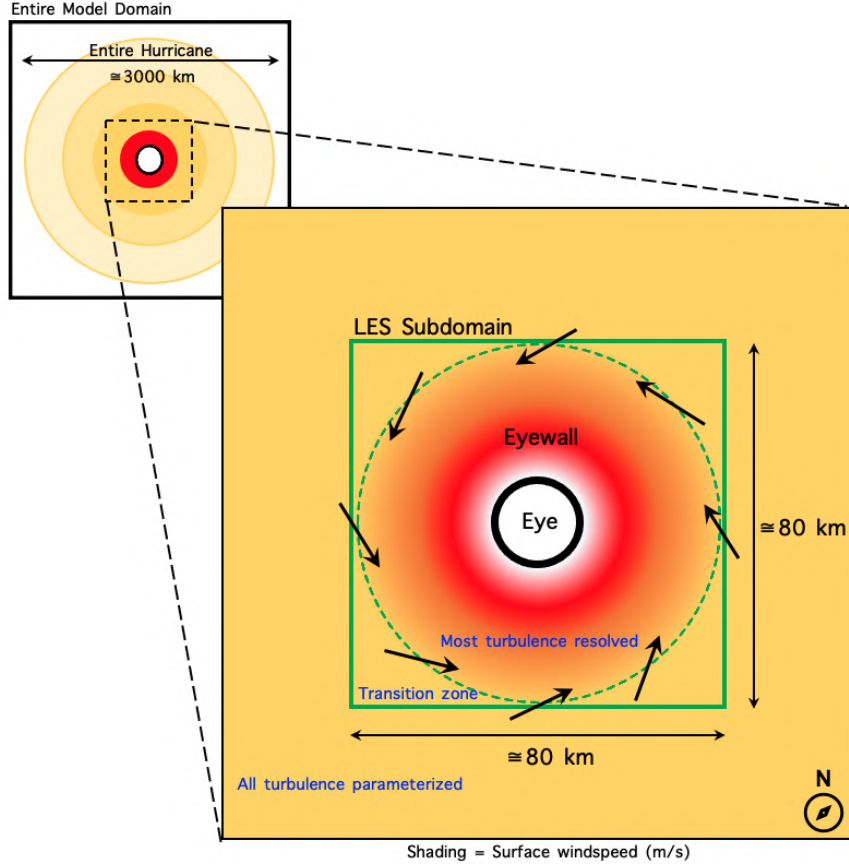


Figure 3.1. Schematic showing the model-simulation setup. The green box (LES subdomain) represents the region on which the analysis presented in this study is focused. Color shading qualitatively represents near-surface wind speed, with red colors being the highest values.

One of the challenges for LES in a domain where the flow enters without turbulence from a coarser-grid domain [e.g., 155, 154, 209] is for the model to develop realistic, resolved turbulence quickly given an air parcel’s short transit time through the fine-grid domain (green box in Fig. 3.1). To make sure the boundary-layer turbulence becomes fully developed as the boundary-layer flow transitions from the coarse grid to the fine, a separate precursor LES of the hurricane boundary layer for the flow beyond the LES subdomain is used to initiate turbulence in a transition zone (Fig. 3.1) [see details in [24]].

For cloud microphysics, the double-moment scheme of [149] is used in the entire simulation domain. The parameterization of surface stress is described in Bryan et al. [25]; most of the LES subdomain has average 10-m wind speed above  $25 \text{ m s}^{-1}$ , for which the surface roughness length  $z_0$  is constant at 2.8 mm. Surface heat fluxes assume a constant exchange coefficient of  $1.2 \times 10^{-3}$ . No radiation scheme is used, although the simple relaxation method of Rotunno and Emanuel [182] (hereafter RE87) is used for temperature; this tendency is negligibly small in the LES subdomain. Further details of the modeling setup, as well as additional analyses of this simulation, are available in Stern and Bryan [204].

When analyzing turbulent flows, it can be challenging to obtain robust results that reveal insights into the role of the turbulent eddies in a seemingly chaotic flow [e.g., 141]. Typically, a combination of space- and time-averaging is used to define mean fields, with perturbations from those means being used to define turbulent fluxes and variances. Large datasets are often required to obtain reliable results. To this end, for analyses presented in the following section, the model was “restarted” after 4 hours and integrated for an additional 1 hour with output every 30 s. Hence, there are 121 snapshots of simulation output from  $t=14,400\text{s}$  to  $t=18,000\text{s}$  for the following analyses. The analysis procedure is nearly the same as in Section 4 of Nolan et al. [160]. First, all variables are time averaged at relevant points on the model’s C-staggered Cartesian grid. At this stage, the exact same numerical methods that were used in the model integration (e.g., Wicker and Skamarock 231) are used in the analysis, e.g., for interpolation on the staggered grid; we find this approach to be necessary to yield small residuals in budgets of mean model variables (e.g., winds, temperature, and moisture). Then, perturbations from this time-averaged state are calculated at all time levels and are used to calculate second-order statistics such as vertical flux of momentum (e.g.,  $u'w'$ ); these results are then time-averaged to obtain average turbulence fluxes and variances at each grid point. Lastly, all

variables are azimuthally averaged and presented in radius-height  $(r, z)$  coordinates; this last step is effective as a “smoother” of the results because there are many (i.e., thousands) of time-averaged profiles in original model coordinates with this resolution. The resulting mean field from this procedure for quantity  $\chi(x, y, z, t)$  is denoted by  $\langle\chi\rangle(r, z)$  and perturbations by  $\chi' = \chi - \langle\chi\rangle$ .

Resulting mean-field budgets, described in the next section and the Appendix (C), have very small residuals; the sum of all terms on the RHS of the mean-velocity budget equations peaks at  $0.02 \text{ m s}^{-2}$  (not shown). In comparison, the inertial terms in the budget exceed  $0.2 \text{ m s}^{-2}$ , and the LHS of these budgets (the change of  $\langle\chi\rangle$  over the analysis time) are of-order  $0.001 \text{ m s}^{-2}$  (hence the flow is not strictly steady, but can be considered practically steady state). The smallness of the budget residual and the time-tendency terms provide confidence in the methodology described in the previous paragraph.

### 3.3 Results

Figure 3.2 shows sample horizontal slices at  $z \approx 40\text{m}$ ,  $100\text{m}$ ,  $700\text{m}$  and  $1500\text{m}$  of the vertical velocity field  $w$  [m/s] in the S-W quadrant of the storm center, where the solid vertical line roughly cuts through the center ( $r \approx 0\text{km}$ ) of each slice. From Fig. 3.2, it is clear that vertical velocity fluctuations close to the surface ( $z \approx 40\text{m}$  and  $100\text{m}$ ) are weaker than at the upper levels ( $z \approx 700\text{m}$  and  $1500\text{m}$ ), indicating the influence of the surface boundary [165, 166]. The horizontal scale of turbulent velocity structures is seen to increase with distance from the surface. In addition, at  $z \approx 700\text{m}$  and  $1500\text{m}$ , the eyewall of the TC is clearly defined by the predominantly positive vertical velocity values around the eye, indicative of strong updrafts. Furthermore, above the lower levels, ‘streaks’ (defined here as a linear organization) in the patterns of  $w$  are seen outside the eyewall region. The vertical velocity field is clearly turbulent, with different scales of spatial coherence ranging from well-organized elongated

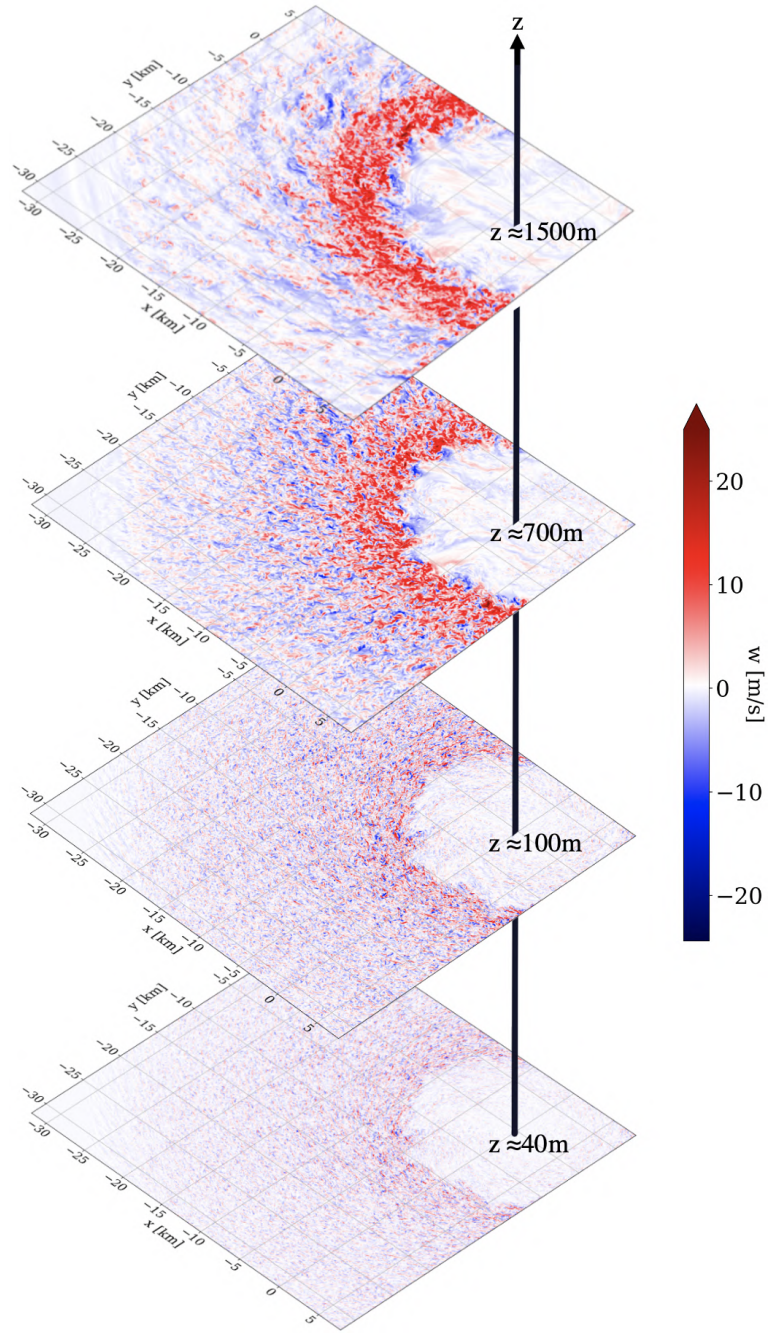


Figure 3.2. Horizontal cross sections of the vertical velocity field  $w$  [m/s] around the SW quadrant of the storm, at different heights. The black vertical arrow passes through the eye of the storm.

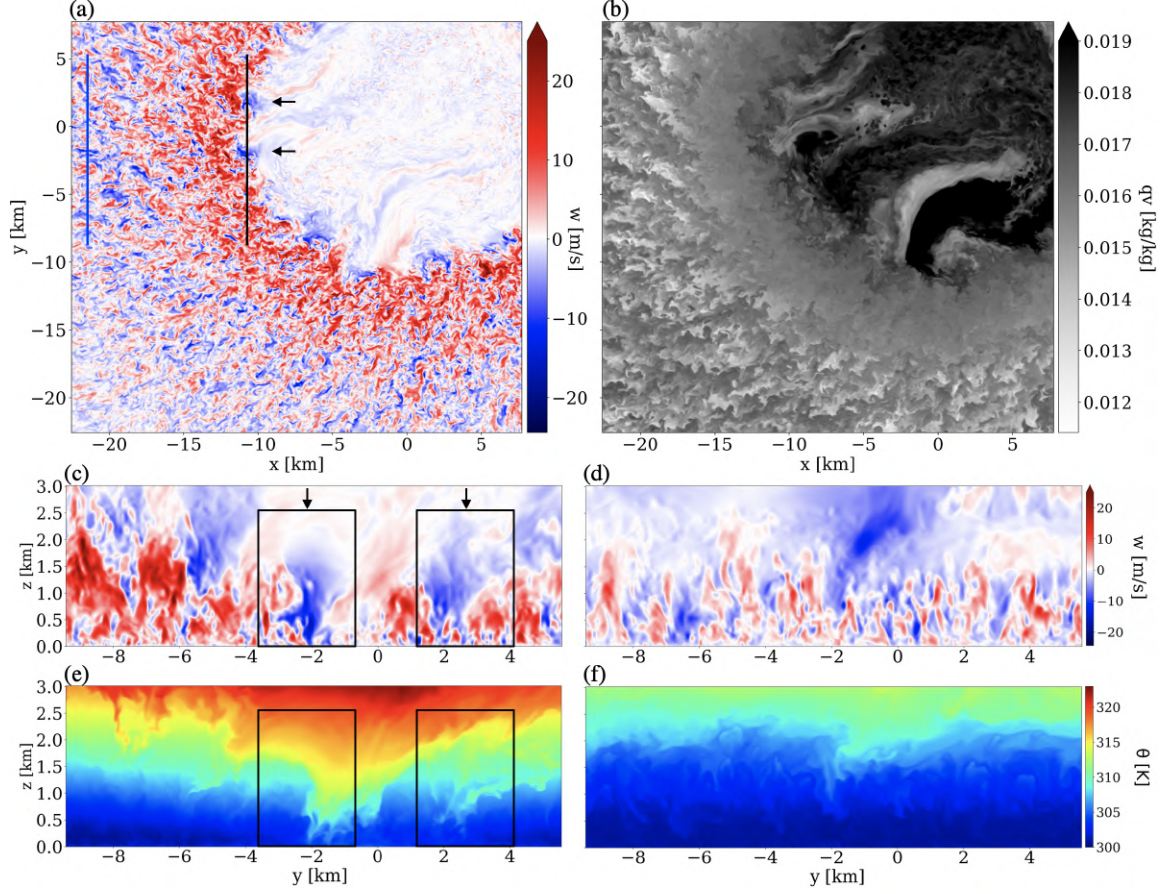


Figure 3.3. Windowed-in horizontal cross sections of (a) vertical velocity [m/s] in the southwest quadrant of the LES model domain and (b) water vapor mixing ratio [kg/kg], at  $z \approx 700\text{m}$ . Vertical cross sections of (c) vertical velocity [m/s] and (e) potential temperature [K] in the inner eyewall ( $r \approx 11\text{km}$ ). Vertical cross sections of (d) vertical velocity [m/s] and (f) potential temperature [K] outside the eyewall ( $r \approx 22\text{km}$ ). The black and blue lines in (a) represent the locations (inner eyewall and outside the eyewall respectively) from which the vertical sections in (c) & (e) and (d) & (f) are plotted, respectively. The boxes in (c) and (d) highlight the vertical extent of two kilometer-scale intense downdraft features in (a).

streaks to seemingly unorganized patches of updrafts and downdrafts.

Focusing on  $z \approx 700\text{m}$ , Figs. 3.3a-b show a windowed-in sample of the vertical velocity and water vapor mixing ratio fields for just the S-W quadrant of the storm (same as Fig. 3.2). In Fig. 3.3a, there are a number of kilometer-scale intense updraft-

downdraft couplets in the inner edge of the eyewall (two of which are highlighted by the arrows), with changes in the magnitude of  $w \geq 10\text{m/s}$  across the couplets, in some cases. The magnitude of these updraft-downdraft pairs seen here are also similar to those seen in field observations of intense storms [205]. For example, in Hurricane Felix (a Cat 5 storm in 2007), the NOAA42 research aircraft experienced a sequence of  $10\text{m/s}$  downdraft,  $31\text{m/s}$  updraft and  $7\text{m/s}$  downdraft within 1 minute [3]. These features, distributed along the inner edge of the eyewall, are also quite similar to those documented in several observations of intense storms [2, 218]. The sizes of these coherent velocity structures appear to decrease with increasing radial distance from the storm center. In addition, visibly elongated streaks of negative velocity signatures are seen farther from the eye, roughly inclined towards the eye of the storm. The shape of these quasi-linear streaks quickly deform from their elongated form farther from the eye, to a more compact cellular form in the inner edge of the eyewall region. In the simulated mixing ratio ( $q_v$ ) plot shown in Fig. 3.3b, the structure in the southern part of the inner eyewall, i.e., ranging from  $x \approx -5\text{km}$  to  $5\text{km}$  at  $y \approx -12\text{km}$ , is qualitatively similar to the mesovortices (MVs) identified in the inner eyewall of Hurricane Harvey (a Category 4 storm in 2007) by [237] and [8] using Doppler radar, as is the associated collocated vertical velocity signature in Fig. 3.3a. The MVs documented by [8] were found to be associated with intense updrafts (quite similar to our study), around wind field perturbations of about  $5 - 10\text{m/s}$ . In a quantitative study of eyewall MVs (using the Himawari-8 satellite imagery) and their role in the enhancement of inner-core rotation by angular momentum transport, [218] also identified features rotating in the inner eyewall of Typhoon Lan (2017) which are strikingly similar to Fig. 3.3b. Similar features (i.e., large scale MVs of  $\approx 20 - 30\text{km}$  in size) were also documented in Hurricane Karl (2010) by [74], adjacent to convective bursts, and were shown to be transporting air across the eye – eyewall interface. These types of features are clearly present in this simulation.

A vertical cross section through these structures in the vertical velocity field at  $r \approx 11\text{km}$  (inner eyewall – black line) and  $r \approx 22\text{km}$  (outside the eyewall – blue line) is shown in Figs. 3.3c-d, respectively. Two intense downdrafts (highlighted by the arrows in Fig. 3.3a) are identified in Fig. 3.3c, showing a vertical extent of  $\approx 2.5\text{km}$  and associated vertical transport indicated by the signatures from the cross section of potential temperature at the same location and time (Fig. 3.3e). Farther from the inner eyewall (blue line at  $r \approx 22\text{km}$  in Fig. 3.3a), a vertical cross section of the same variables (Figs. 3.3d and f) show a smaller and weaker updraft-downdraft couplet.

From Figs. 3.2 and 3.3, it is clear that this simulation produces several mesovortex-type structures and coherent turbulent eddies whose magnitude, spatial distribution, and associated updraft-downdraft couplets are consistent with observational studies (see animations of Figs. 3.3a and b in the supplementary materials section). These figures and animations also reveal a potential disadvantage of our analysis methodology (Section 2), in that all of these coherent structures are included in our analysis, even though some km-scale features may not be considered “turbulence” by traditional textbook definitions. Indeed, some of these features could be resolvable using even 1-km horizontal grid spacing, and would not need to be included in a turbulence (i.e., PBL) parameterization. Nevertheless, we see no easy way to remove the km-scale features from our analysis, and the resulting analyses are insightful, even if the direct application to operational PBL parameterization is uncertain. The rest of this paper is focused on understanding the roles of these turbulent eddies in modulating the mean flow around the TC eyewall region.

### 3.3.1 The Mean Velocity Fields

Before addressing the role of turbulence on the mean field, it is important to have a clear picture of the mean flow field itself. The geometry of a mature TC makes the cylindrical coordinate system particularly useful in representing its dynamics.

Here, we discuss the magnitude and direction of the azimuthally and time-averaged velocity components in Fig. 3.4. Figures 3.4a-c show the radius – height plots of the azimuthally and time-averaged velocity components, showing the expected radial variation of velocity fields seen in observations [e.g., 178, 253]. Figure 3.4a shows that the maximum tangential velocity is at a radius of  $r \approx 11 \text{ km}$  near the surface, and slopes outwards with height. Mean tangential velocity decreases steadily with increasing radii beyond the eyewall, while also decreasing to zero towards the eye ( $r \approx 0 \text{ km}$ ). Figure 3.4b shows that the radial velocity is negative close to the surface, indicating strong inflow towards the eyewall region, which decreases with height until it becomes positive aloft, typical of the HBL. The level of maximum inflow is 50–75 m, slightly lower but consistent with observations [252, 140, 6, 253]. Figure 3.4c shows that the mean vertical velocity is weak in most of the HBL except in the eyewall ( $r \approx 10\text{--}17 \text{ km}$  – highlighted by the black solid contour), where it is clearly positive, indicating a strong mean updraft characteristic of intense eyewall convection. A notable mean downdraft (indicated by negative vertical velocity – blue shading) is seen just outside of the eyewall ( $r \approx 21 \text{ km}$ ).

Together, the azimuthally and time-averaged velocity field plots shown in Figs. 3.4a-c (summarized in Fig. 3.4d) indicate maximum radial inflow and weak vertical velocity at the outer edge of the eyewall ( $r \approx 17 \text{ km}$ ) and close to the surface. As the mean radial inflow approaches the inner eyewall ( $r \approx 11 \text{ km}$ ), it reduces to zero in the corner flow region — the region within the inner edge of the eyewall where the strong radial inflow slows down and turns upwards through mass continuity; here the vertical velocity substantially increases to a maximum above the BL (which we define roughly as the first 1 km above the surface). This flow pattern shows that the mean trajectory of air parcels follows an inflow path towards the core, followed by a deceleration and a sharply defined mean updraft in the eyewall region, consistent with previously well-established understanding of the mean structure of the TC boundary

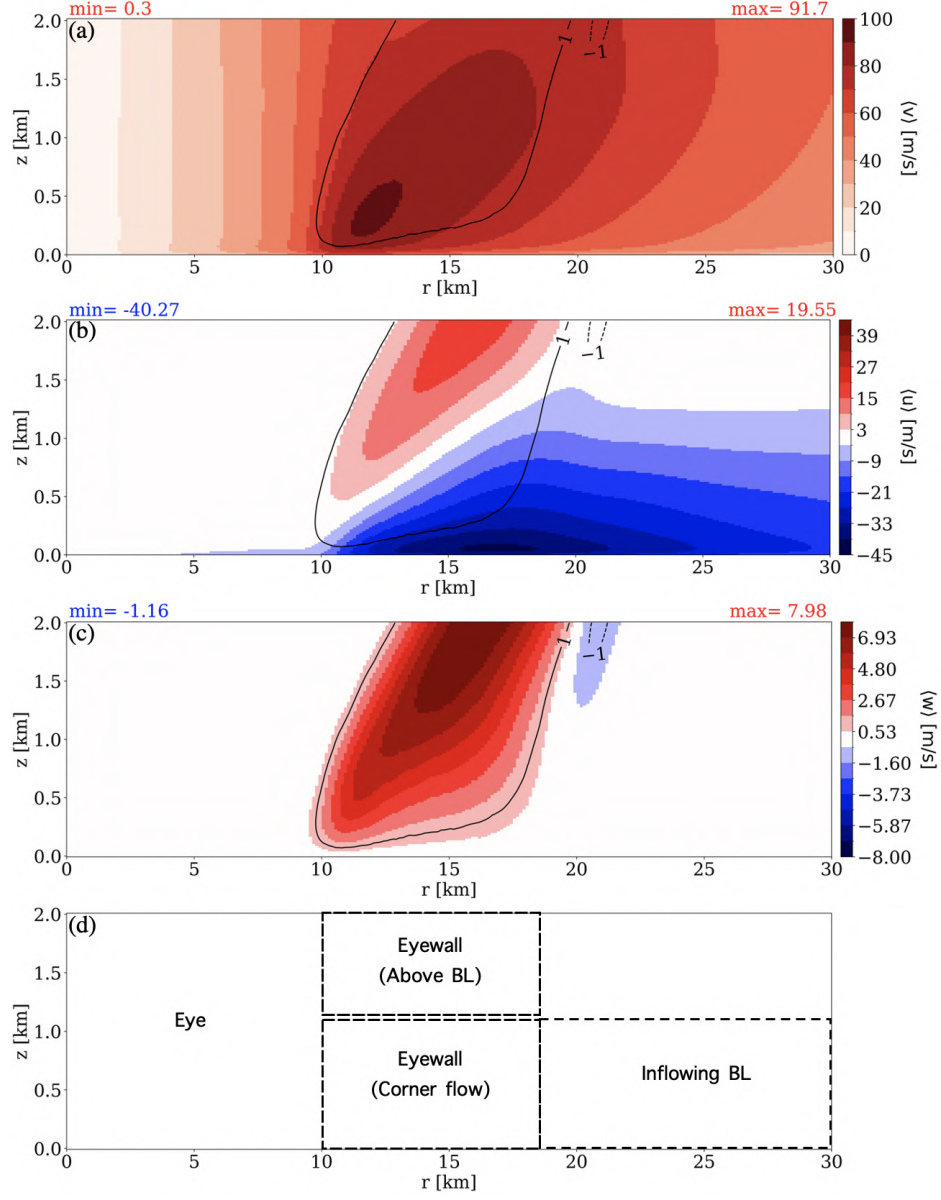


Figure 3.4. Plots of the azimuthally and time-averaged velocity components for (a) tangential velocity  $\langle v \rangle$ , (b) radial velocity  $\langle u \rangle$  and (c) vertical velocity  $\langle w \rangle$ , all in [m/s]. The solid and dashed black contour lines in each panel indicates  $\langle w \rangle$  at  $\pm 1.0$  m/s, highlighting the eyewall region and a significant downdraft feature just outside the eyewall, respectively. (d) Plot showing the nomenclature used in the identification of regions in the simulation; the top of the boundary layer (BL) is considered to be roughly (but not strictly) at 1 km.

layer [195, 131, 99, 200, 178, 167, 145, 146]. We now move towards understanding the impact of turbulence on this mean flow.

### 3.3.2 Mean Field Budget - The Role Of Turbulent Eddies

As shown above, coherent turbulent velocity structures are prevalent in the TC boundary layer, particularly in the eyewall. The question thus arises as to what role they play in the budget of the mean wind field equations. Do they act to enhance momentum in the eyewall or do they act to weaken it? To clarify the role of turbulent eddies, we derive the azimuthally and time-averaged momentum equations [in cylindrical coordinates, similar to [82, 72, 203, 160]], and compute each term appearing on the right hand side from the model simulation output:

$$\begin{aligned} \frac{\partial \langle u \rangle}{\partial t} = & -\langle u \rangle \frac{\partial \langle u \rangle}{\partial r} - \langle w \rangle \frac{\partial \langle u \rangle}{\partial z} - \underbrace{\frac{1}{r} \frac{\partial}{\partial r} \langle r u'^2 \rangle}_{T_r^u} - \underbrace{\frac{\partial}{\partial z} \langle u' w' \rangle}_{T_z^u} + \frac{\langle v \rangle^2}{r} + \frac{\langle v'^2 \rangle}{r} - \frac{\partial \langle \phi \rangle}{\partial r} \\ & + f \langle v \rangle + \langle F^u \rangle, \end{aligned} \quad (3.1)$$

$$\begin{aligned} \frac{\partial \langle v \rangle}{\partial t} = & -\langle u \rangle \frac{\partial \langle v \rangle}{\partial r} - \langle w \rangle \frac{\partial \langle v \rangle}{\partial z} - \underbrace{\frac{1}{r^2} \frac{\partial}{\partial r} \langle r^2 u' v' \rangle}_{T_r^v} - \underbrace{\frac{\partial}{\partial z} \langle v' w' \rangle}_{T_z^v} - \frac{\langle u \rangle \langle v \rangle}{r} - f \langle u \rangle + \\ & \langle F^v \rangle, \end{aligned} \quad (3.2)$$

$$\begin{aligned} \frac{\partial \langle w \rangle}{\partial t} = & -\langle u \rangle \frac{\partial \langle w \rangle}{\partial r} - \langle w \rangle \frac{\partial \langle w \rangle}{\partial z} - \underbrace{\frac{1}{r} \frac{\partial}{\partial r} \langle r u' w' \rangle}_{T_r^w} - \underbrace{\frac{\partial}{\partial z} \langle w'^2 \rangle}_{T_z^w} - \frac{\partial \langle \phi \rangle}{\partial z} + F_b + \langle F^w \rangle. \end{aligned} \quad (3.3)$$

Because this simulation is statistically steady, the LHS of the equations above are negligible (see Section 2). The symbols  $u$ ,  $v$ , and  $w$  represent the radial, tangential,

and vertical velocity components;  $r$  is the radius;  $f$  is the Coriolis parameter;  $\phi$  is the density-normalized pressure;  $F_b$  is buoyancy [see 22] and the terms with a prime (') indicate differences from the mean. The symbols  $F^u, F^v, F^w$  represent contributions from the LES subgrid tendencies. In (1)-(3), the third and fourth terms ( $T_r^{u/v/w}$  and  $T_z^{u/v/w}$ ) on the RHS represent the momentum tendencies due to divergence of the turbulent-eddy fluxes in the radial and vertical directions, respectively. To understand the role of the turbulence in the evolution of the mean wind field, we evaluate the contributions of these turbulent tendencies below. In all of the plots shown in Fig. 3.5, the subgrid contribution (in the radial  $\langle F_r^{u/v/w} \rangle$  and vertical  $\langle F_z^{u/v/w} \rangle$  directions) - which are negligible except in the lowest few model levels - are included with the resolved terms. See Appendix C for a comparative analysis of resolved and parameterized turbulent tendencies on the mean flow where the subgrid part is seen to be relevant only in the lowest model levels. In Appendix C, we also briefly comment on the tendencies from the mean advection and other non-turbulence terms which appear in (3.1) – (3.3).

For the  $\langle u \rangle$  budget in (3.1), Figs. 3.5a-b show the contribution to the mean flow by the turbulence flux divergences in the radial and vertical directions. The black contours indicate the mean radial velocity  $\langle u \rangle$  (with a contour interval of 5m/s). Both radial and vertical eddy tendencies act to weaken the magnitude of the radial velocity in the inflow region. From Fig. 3.5a, the radial tendency field is a dipole at  $r \approx 11\text{km}$ , indicating diffusion of radial inflow along the strong gradient of  $\langle u \rangle$ . Furthermore, the vertical eddy-flux divergence (Fig. 3.5b) primarily acts to diminish the magnitude of radial inflow close to the surface (from the inflow BL to the corner flow), ultimately leading to the loss of momentum due to drag. A comparison of the radial and vertical eddy tendencies here indicate that the weakening role (red shading) of the vertical term is significantly larger, especially closer to the surface (below the height of maximum radial inflow).

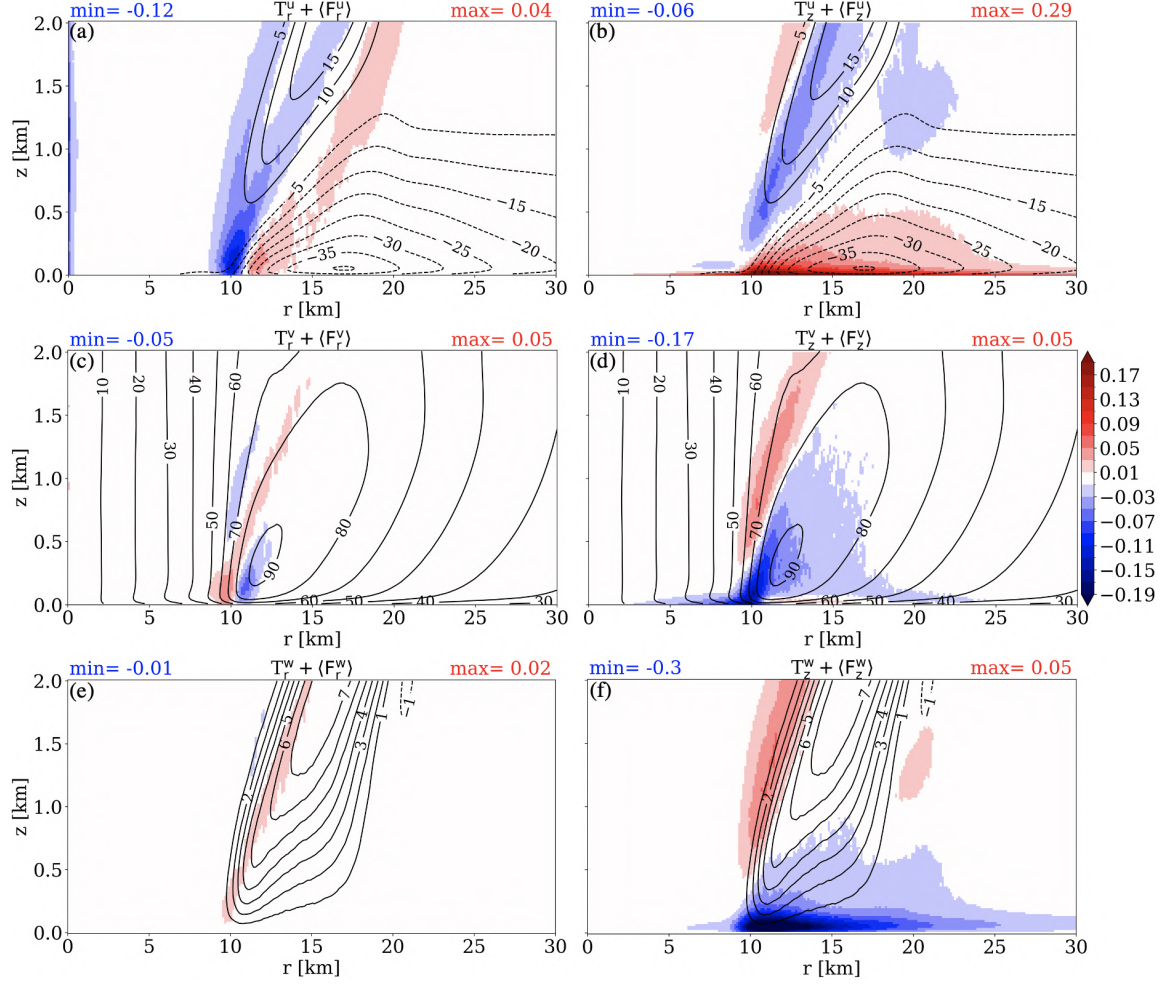


Figure 3.5. Contour plots of azimuthally and time-averaged radial velocity field  $\langle u \rangle$ , overlain with shadings from the contributions due to turbulent eddy tendencies in the (a) radial ( $T_r^u + \langle F_r^u \rangle$  in  $ms^{-2}$ ) and (b) vertical ( $T_z^u + \langle F_z^u \rangle$  in  $ms^{-2}$ ) directions. Panels (c) (for  $T_r^v + \langle F_r^v \rangle$ ) and (d) (for  $T_z^v + \langle F_z^v \rangle$ ) represent analogous plots for the average tangential velocity field  $\langle v \rangle$ . Panels (e) (for  $T_r^w + \langle F_r^w \rangle$ ) and (f) (for  $T_z^w + \langle F_z^w \rangle$ ) represent analogous plots for the average vertical velocity field  $\langle w \rangle$ .

For the  $\langle v \rangle$  budget, Figs. 3.5c-d show the contribution to the mean flow by the turbulence flux divergences in the radial and vertical directions. The black contours indicate the azimuthally and time-averaged tangential velocity  $\langle v \rangle$  which peaks near the inner edge of the eyewall. Because of the negative values of eddy tendencies in

the vicinity of  $V_{max}$ , both the radial and vertical eddy tendencies act to weaken the maximum value of the tangential wind speed. In Fig. 3.5c, the radial eddy tendency is a dipole just inward of the eyewall ( $r \approx 10\text{km}$ ), and thus acts to diffuse momentum at the eye/eyewall interface. The vertical eddy tendency (Fig. 3.5d) primarily diffuses momentum along and just inward of  $V_{max}$ . In addition, the vertical eddy tendency primarily acts to reduce momentum along most of near-surface boundary leading to the eyewall (weak blue shading in Fig. 3.5d outside of  $V_{max}$ ). We also note that in Figs. 3.5c-d, the eddy-flux divergences along the  $V_{max}$  contour (blue shading) are accompanied by a momentum “spin up” in the inner edge of  $V_{max}$  towards the eye (red shading) which extends to a height of  $\approx 2\text{km}$ . This “spin up” extends closer to the surface, by the role of the radial eddy tendencies (Fig. 3.5c). In a related budget analyses, a similar role of radial eddy tendencies (i.e., their simultaneous “spin up” – “spin down” activity) around  $V_{max}$  was documented by [167] in both 3D and axisymmetric model configurations. Additionally, [58] showed using a theoretical model, that due to the flow transition from the TC eyewall to the eye being strongly frontogenetic (for angular momentum and moist entropy), radial turbulent momentum diffusion at the eye–eyewall interface consequently allows a mechanism for the mechanical spin-up of the eye. These patterns from our turbulence-resolving simulation reflect the diffusion of mean angular velocity [see next subsection] away from its peak, and agrees with the idea that the “spin up” of the TC eye and the turbulence-induced diffusive “spin down” of the eyewall ( $V_{max}$ ) is indeed a feature of TCs [58, 167] even in LES.

Curiously, near the surface, there is a weak positive contribution to  $\langle v \rangle$  (light red shading in Fig. 3.5d) just outside of  $V_{max}$  ( $r \approx 11\text{--}17\text{km}$ ) below the height of maximum radial inflow ( $z < 50\text{m}$ ). This weakly positive anomalous tendency suggests a weak enhancement of tangential velocity by turbulent eddies. Figures 3.6a–c show that, at the inner edge of the eyewall (Fig. 3.6a) and outside the eyewall (Fig. 3.6c), the

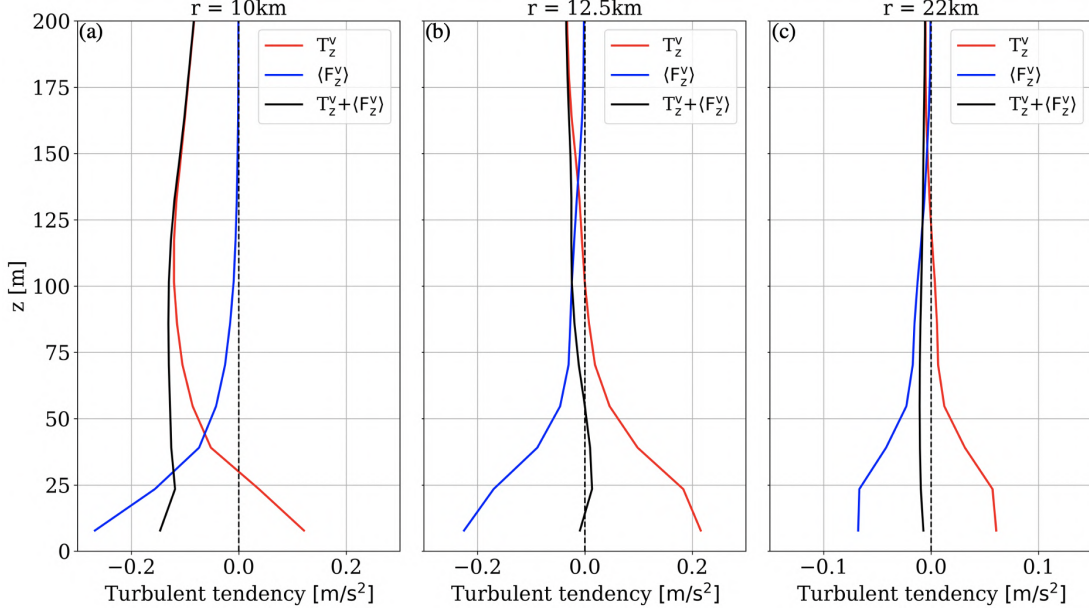


Figure 3.6. Profiles for  $z = 0 - 200\text{m}$ , of resolved ( $T_z^v$  in  $[ms^{-2}]$  - red line), parameterized ( $\langle F_z^v \rangle$  in  $[ms^{-2}]$  - blue line) and total ( $T_z^v + \langle F_z^v \rangle$  - black line) turbulent tendencies in the vertical direction for the tangential velocity (shown in Fig. 3.5d) at (a)  $r=10\text{km}$ , (b)  $r=12.5\text{km}$  and (c)  $r=22\text{km}$ .

total turbulence tendency (black line) is clearly negative. In contrast, within the eyewall (Fig. 3.6b) the total turbulence tendency is slightly positive. We do not have a definitive explanation for this feature, although we note that, in a parcel-following (Lagrangian) perspective, the resolved component  $T_z^v$  increases notably as parcels near the surface enter the corner-flow region, whereas the subgrid component  $F_z^v$  varies smoothly in the same region. This feature might be related to the inhomogeneous conditions, which could violate the assumptions of the surface-layer model, as noted for tornadoes by Wang et al. [225].

Finally, considering the  $\langle w \rangle$  budget, Figs. 3.5e-f show the contribution of the radial and vertical eddy tendencies to the mean flow. The radial eddy tendency (Fig. 3.5e) is small compared to the vertical eddy tendency (Fig. 3.5f) which is significantly negative in the lowest region of the inner eyewall and roughly balances the sum of

the buoyancy contribution and the vertical gradient of the normalized pressure term (see Fig. C.3). The vertical eddy tendency acts to diminish the strength of the mean upward flow of the vertical velocity in the eyewall. In other words, it opposes the mean eyewall updraft, reducing the magnitude of mean vertical velocity near the surface in the eyewall.

The foregoing analysis indicates that the net effect of the turbulent eddy tendencies in the eyewall region is essentially diffusive in nature – acting to reduce  $V_{max}$ , weaken the strength of the radial inflow close to the surface, as well as the upward flow of air in the eyewall. We also find, from the magnitude and spatial distribution of the eddy tendency terms in the budget equations, that the turbulence tendencies in the vertical direction ( $T_z^{u/v/w} + \langle F_z^{u/v/w} \rangle$  i.e., Figs. 3.5b-d-f ) are generally larger and more spatially prevalent in most of the simulated HBL than those in the radial direction ( $T_r^{u/v/w} + \langle F_r^{u/v/w} \rangle$  i.e., Figs. 3.5a-c-e), consistent with conventional boundary layer theory. In the localised region around  $r \approx 11\text{km}$ , however, the radial tendencies ( $T_r^{u/v} + \langle F_r^{u/v} \rangle$ ) become comparable in magnitude to the vertical ( $T_z^{u/v} + \langle F_z^{u/v} \rangle$ ) in terms of their influence on the mean field. In other words, in the inflowing boundary layer (Fig. 4d), the turbulence plays a role similar to a typical PBL, while in the eyewall a more complex picture emerges. The role of turbulent eddies in the mean budget analyses carried out in this study is qualitatively similar to the findings from a similar budget analysis for a tornado by [160].

### 3.3.3 The Validity Of Eddy Viscosity Hypothesis & Estimates Of Effective Mixing Lengths

Now that we have established that the turbulence tendencies primarily act to diffuse the mean momentum fields, we now examine a simple turbulence parameterization of eddy fluxes in the hurricane boundary layer. As a consequence of their relatively coarse resolution ( $>1\text{km}$ ), operational weather forecast models must param-

eterize the role of turbulence. Traditionally, using the molecular diffusion analogies for the eddy fluxes [Anthes 12; RE87; Stull 208], the down-gradient hypothesis is assumed for the unresolved momentum fluxes. In principle, each flux term can be parameterized by its own eddy viscosity as shown in (3.4) – (3.6), where  $K_z^u$ ,  $K_z^v$  are effective eddy viscosities for vertical fluxes of  $u$  and  $v$ , and  $K_h$  is an effective eddy viscosity for the  $\langle u'v' \rangle$  term:

$$\langle u'w' \rangle \approx -K_z^u \frac{\partial \langle u \rangle}{\partial z}, \quad (3.4)$$

$$\langle v'w' \rangle \approx -K_z^v \frac{\partial \langle v \rangle}{\partial z}, \quad (3.5)$$

$$\langle u'v' \rangle \approx -K_h r \frac{\partial \langle v \rangle}{\partial r} \frac{1}{r}. \quad (3.6)$$

Since the eddy viscosity is indicative of the “strength” of mixing, it plays a role in the qualitative description of turbulence intensity in the HBL. Here, we evaluate the validity of the widely used down-gradient hypothesis, namely whether or not it leads to nonphysical negative values of the eddy viscosity. [It should be noted that in the fluxes ( $\langle u'w' \rangle$ ,  $\langle v'w' \rangle$ , and  $\langle u'v' \rangle$ ) discussed below, both the resolved and subgrid flux components – which is only significant in the lowest model levels – are combined and presented].

Figure 3.7a shows the vertical flux of radial velocity  $\langle u'w' \rangle$  (shaded) and mean radial velocity  $\langle u \rangle$  (black contours). The vertical flux  $\langle u'w' \rangle$  is generally negative in most of the hurricane boundary layer and at most radii (apart from close to the surface and aloft in the inner eyewall,  $z \geq 700\text{m}$  and  $r \approx 11\text{km}$ ). The negative-flux region collocates with regions of positive vertical gradient in radial velocity (Fig. 3.7b), while the regions of positive fluxes close to the surface coincide with negative gradients, suggesting the down-gradient hypothesis is indeed valid. To show this relation more clearly, the effective eddy viscosity  $K_z^u = -\langle u'w' \rangle / \frac{\partial \langle u \rangle}{\partial z}$  is plotted in

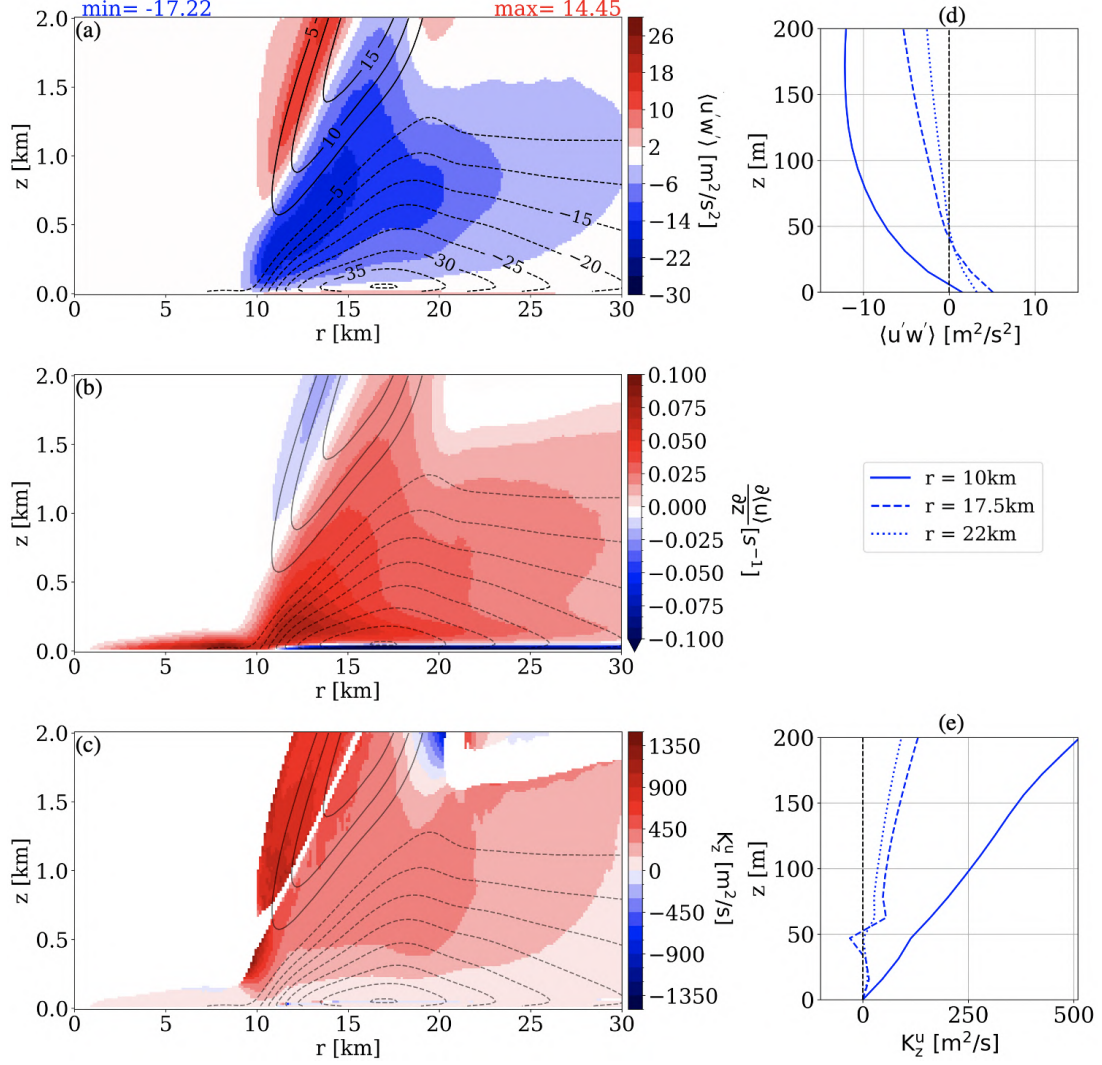


Figure 3.7. Contour plots of mean radial velocity  $\langle u \rangle$  in [m/s], overlain by shadings of (a) azimuthally and time-averaged vertical fluxes of radial velocity  $\langle u'w' \rangle$  in [ $m^2 s^{-2}$ ], (b) the vertical gradient of mean radial velocity  $\frac{\partial \langle u \rangle}{\partial z}$  in [ $s^{-1}$ ] and (c) the effective eddy viscosity  $K_z^u$ , in [ $m^2 s^{-1}$ ]. [Plots (b) and (c) use the same contour interval for  $\langle u \rangle$  as in (a)]. Panels (d) and (e) show near-surface profiles of  $\langle u'w' \rangle$  and  $K_z^u$  respectively, for the first 200m height, at  $r=10$ km (solid-blue line),  $r=17.5$ km (dashed-blue line) and  $r=22$ km (dotted-blue line).

Fig. 3.7c, showing positive values in most of the TC boundary layer, indicative of down-gradient turbulent transport. A thin region of negative  $K_z^u$  is seen at the top of the inflow BL at about  $r \approx 20$ km, close to the weak gradient,  $\frac{\partial \langle u \rangle}{\partial z} \approx 0$ , zone in

Fig. 3.7b. We note that in computing  $K_z^u$ , gradients which are less than 3% of the maximum  $|\frac{\partial \langle u \rangle}{\partial z}|$  are excluded because the down-gradient hypothesis is not applicable in regions with near-zero mean gradients, which would lead to nonphysically large eddy viscosity values. Figures 3.7d and e shows near-surface profiles of  $\langle u'w' \rangle$  and  $K_z^u$ , respectively, at specific radii of interest. From Fig. 3.7d (at  $r \approx 17.5\text{km}$  and  $r \approx 22\text{km}$ ), weakly positive vertical momentum flux is seen below the height of maximum radial inflow ( $z < 50\text{m}$ ). Just above, near the level of maximum inflow where the mean gradient is small, Fig. 3.7e indicates a weak region of counter-gradient flux denoted by negative  $K_z^u$ . In contrast, the profile at  $r \approx 10\text{km}$  (solid blue lines in both Figs. 3.7d and e) shows a steady increase of  $\langle u'w' \rangle$  and  $K_z^u$  with height, with  $K_z^u$  staying positive, as this profile was located slightly inwards of the eyewall where the maximum value of inflow is at the surface.

For the vertical flux of tangential velocity  $\langle v'w' \rangle$ , Fig. 3.8a shows that negative values at the lower heights ( $z \leq 500\text{m}$ ) correspond to regions of positive vertical gradients (Fig. 3.8b), while positive-flux values are generally associated with the negative gradients where there is outflow above the boundary layer. Plotting  $K_z^v = -\langle v'w' \rangle / \frac{\partial \langle v \rangle}{\partial z}$  in Fig. 3.8c, again the down-gradient hypothesis is seen to be valid for most of the HBL, except for a narrow band of negative eddy viscosity (counter-gradient flux) which extends from the inner eyewall to a radius of  $\approx 30\text{km}$ . Again, mean gradients  $< 3\%$  of  $\max|\frac{\partial \langle v \rangle}{\partial z}|$  are excluded here. A closer look at the vertical gradient field  $\frac{\partial \langle v \rangle}{\partial z}$  shown in Fig. 3.8b indicates that this region of counter-gradient flux (seen in Fig. 3.8c) coincides with a region of comparatively weak vertical velocity gradient of tangential velocity along the inflow boundary, similar to the results for radial velocity above. Figures 3.8d and e show near-surface profiles of  $\langle v'w' \rangle$  and  $K_z^v$ , respectively, at specific radii of interest ( $r=10\text{km}$ ,  $12.5\text{km}$  and  $22\text{km}$ ). The height of counter-gradient flux (i.e., negative  $K_z^v$ ) at  $r=10\text{km}$  (solid blue line in Fig. 3.8e) corresponds to the height where the mean velocity gradient (Fig. 3.8b) transitions

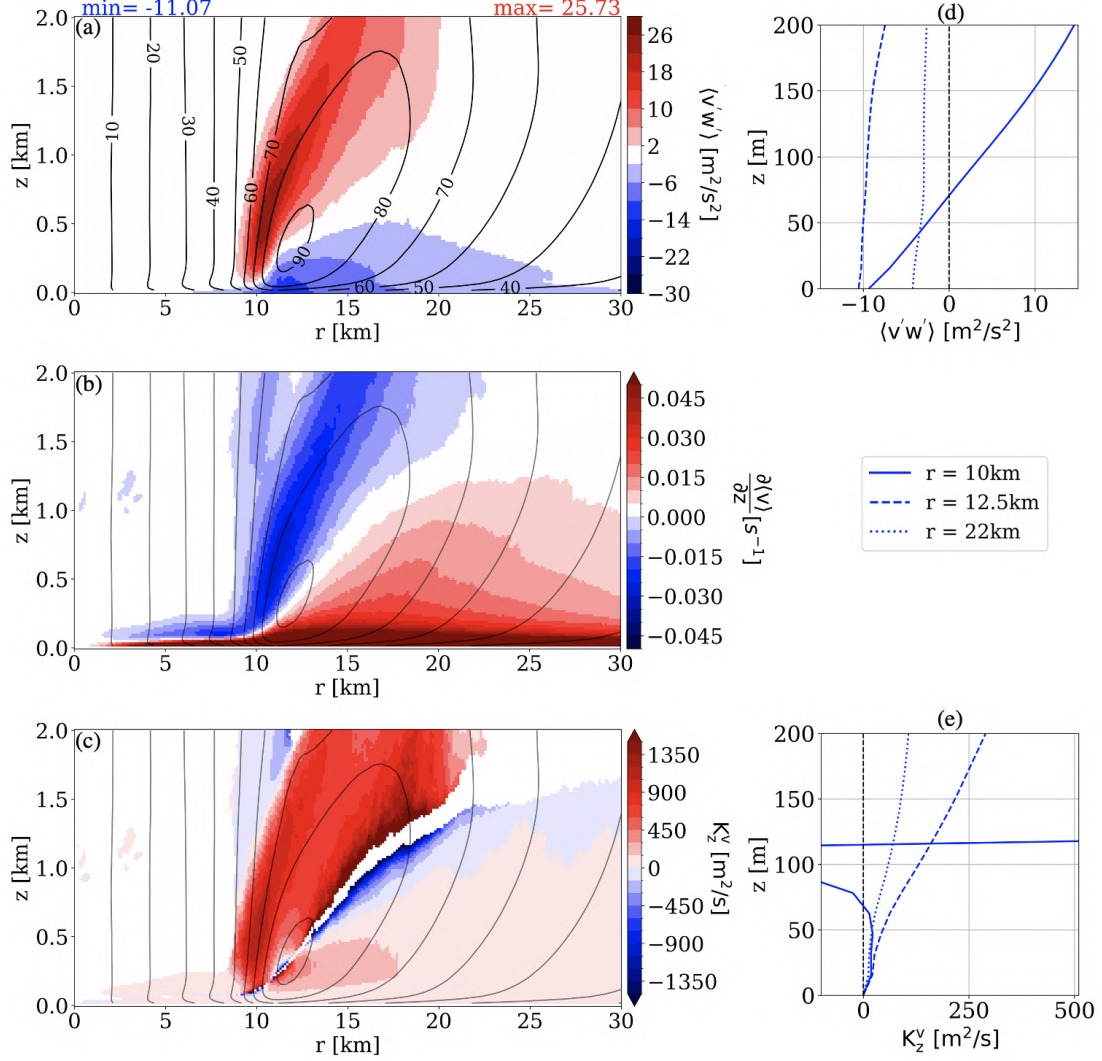


Figure 3.8. Contour plots of mean tangential velocity  $\langle v \rangle$  in  $[m/s]$ , overlain by shadings of (a) azimuthally and time-averaged vertical fluxes of tangential velocity  $\langle v'w' \rangle$  in  $[m^2 s^{-2}]$ , (b) the vertical gradient of mean tangential velocity  $\frac{\partial \langle v \rangle}{\partial z}$  in  $[s^{-1}]$  and (c) the effective eddy viscosity,  $K_z^v$  in  $[m^2 s^{-1}]$ . [Plots (b) and (c) use the same contour interval for  $\langle v \rangle$  as in (a)]. Panels (d) and (e) show near-surface profiles of  $\langle v'w' \rangle$  and  $K_z^v$  respectively, for the first 200m height, at  $r \approx 10$  km (solid-blue line),  $r \approx 12.5$  km (dashed-blue line) and  $r \approx 22$  km (dotted-blue line).

from positive to negative, similar to the behaviour seen in  $K_z^u$  above, at  $r = 17.5$  km and  $r = 22$  km (Fig. 3.7e).

These results highlight that, although the down-gradient hypothesis is largely

valid in the HBL according to this simulation, regions near weak mean gradients can be problematic. This is in agreement with a recent LES study in sheared environments by [229], where counter-gradient fluxes of  $\langle v'w' \rangle$  near the top of the HBL were associated with a weak vertical gradient in the tangential velocity. We note, however, that regions of counter-gradient fluxes in Figs. 3.7c and 3.8c correspond to regions where the contribution of the turbulent tendencies ( $T_z^u$  and  $T_z^v$ ) to the mean field budgets in Figs. 3.5b and d, respectively, are not substantial, suggesting that down-gradient diffusion is sufficient for parameterization of the inner core of strong hurricanes. Of course, further analysis is needed with different types of storms (e.g., larger, weaker, sheared, etc.) to test the robustness of this conclusion.

This analysis of  $K_z^u$  and  $K_z^v$  helps clarify vertical turbulent flux distribution in and around the TC eyewall, where the flow becomes complex near the corner flow region. For PBL parameterizations, however, consolidating  $K_z^u$  and  $K_z^v$  into one effective eddy viscosity for momentum fields is common practice, in order to reduce the number of parameters. To characterize this type of effective eddy viscosity, we use the equation:

$$K_{\text{eff}}^v = \frac{\sqrt{\langle u'w' \rangle^2 + \langle v'w' \rangle^2}}{\sqrt{(\partial \langle u \rangle / \partial z)^2 + (\partial \langle v \rangle / \partial z)^2}}, \quad (3.7)$$

The spatial pattern of  $K_{\text{eff}}^v$  in Fig. 3.9 shows that the strongest turbulence is along the inner edge of the eyewall ( $r \approx 10\text{km}$ ), with values as high as  $\approx 1000\text{m}^2\text{s}^{-1}$ . A vertical profile of  $K_{\text{eff}}^v$  at this location is shown in Fig. 3.9b, indicating eddy diffusivity values exceeding  $1000\text{m}^2\text{s}^{-1}$  at  $z \approx 500\text{ m}$ , with values  $\approx 250\text{m}^2\text{s}^{-1}$  for  $z > 1.5\text{km}$  in the eyewall. The high  $K_{\text{eff}}^v$  in this region (the corner flow) is likely explained by the inhomogeneous conditions here, evident in the sharp deceleration of the radial inflow accompanied by increasing vertical velocity. Horizontal velocity gradients, as well as the mean vertical velocity field, are typically assumed to be negligible in boundary layer parameterizations, but in the eyewall of TCs they play a substantial role in the

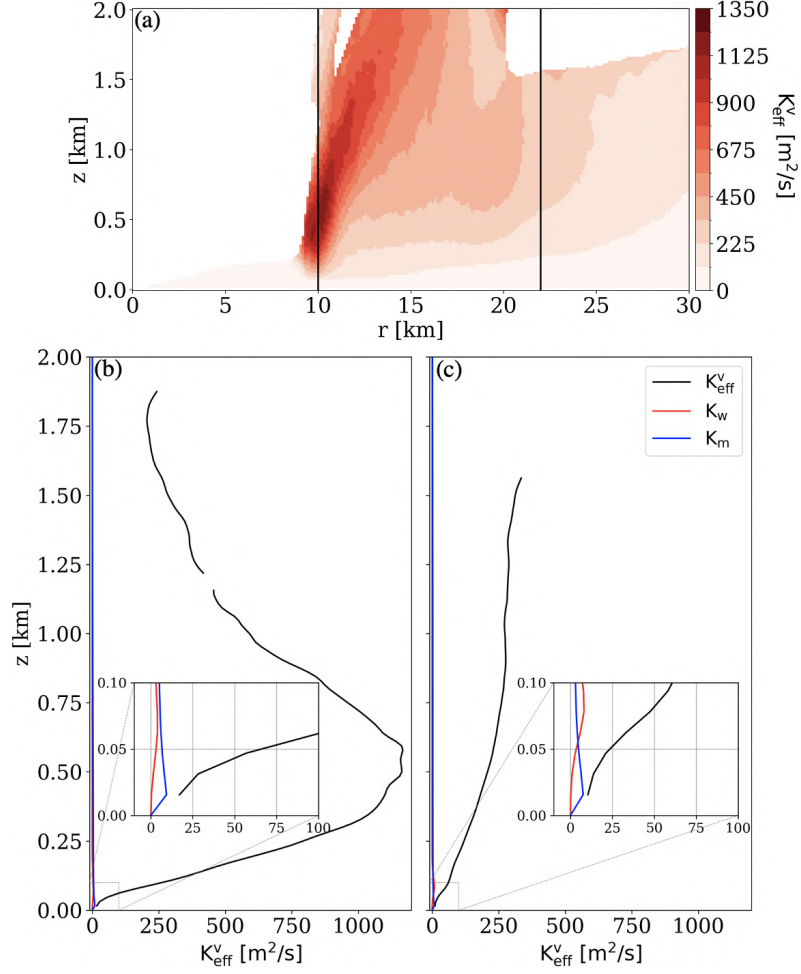


Figure 3.9. (a) Plot of effective eddy viscosity,  $K_{\text{eff}}^v$  in  $[m^2 s^{-1}]$ . Vertical profiles of  $K_{\text{eff}}^v$  – black line,  $K_w$  – red line and  $K_m$  – blue line at (b)  $r \approx 10 \text{ km}$  and (c)  $r \approx 22 \text{ km}$ . [The black vertical lines in (a) indicate the radii where the black profiles in (b) and (c) are plotted]. The insets in (b) and (c) show windowed-in plots of the first 100m height of the BL.

generation of TKE (not shown). Outside the eyewall ( $r \approx 22 \text{ km}$ ), the vertical profile in Fig. 3.9c shows a steady increase of  $K_{\text{eff}}^v$  from the surface to about  $z \approx 500 \text{ m}$ , after which  $K_{\text{eff}}^v$  stays nearly constant with height at a value of  $\approx 300 m^2 s^{-1}$ . In both Figs. 3.9b and c, the insets show that  $K_m$  (the standard subgrid-scale eddy viscosity model) and  $K_w$  (the two-part near-wall subgrid model) are only non-negligible in the lowest few model levels.

The mean values for eddy viscosity ( $\approx 40 - 130 m^2 s^{-1}$ ) reported by [251] using a  $\approx 450$ -m flight-level dataset through the intense eyewall of two Category 4/5 storms are similar to the values ( $\leq 180 m^2 s^{-1}$ ) found in the present study, at a similar height ( $z \leq 0.5$  km) just outside the eyewall (Fig. 3.9c). A similar observational study by [202] using aircraft data from eyewall penetrations of four TCs (at  $\approx 600$ – $650$  m height), found effective vertical eddy viscosity  $> 200 m^2 s^{-1}$  in the eyewall region, well within the range of values seen in the present study.

[246] computed the vertical distribution of eddy diffusivities from observations, using in-situ aircraft data collected during four intense storms. In their study, using data collected during the Coupled Boundary Layers/Air-Sea Transfer Defense Research Initiative (CBLAST) field campaign [18, 66, 51], they found no clear evidence of counter-gradient momentum fluxes. We however note that the data used in their study were far from the storm center, in the outer rainband region of the storms. The analysis presented in this study focuses on the eyewall/inflow BL region of the storm. Additional flights (possibly using unmanned aircrafts) into the most-turbulent regions of the storm at low altitude are needed to further confirm the validity of the down-gradient eddy viscosity hypothesis for momentum fluxes in the inner core of hurricanes.

Going further, simple parameterizations for eddy diffusivity often use a mixing length,  $l$ , e.g.,

$$K_v = l^2 |S_v| \quad (3.8)$$

following the Smagorinsky formulation [197], where  $S_v$  is the deformation [also see 214, pg. 49]. (The effects of buoyancy are neglected for simplicity). Having highlighted the distribution of effective eddy viscosity, we proceed with investigating the spatial distribution of the effective vertical mixing length ( $L_{\text{eff}}^v$ ) in the tropical cyclone BL.

We begin first by computing the effective mixing length using (3.8) and substi-

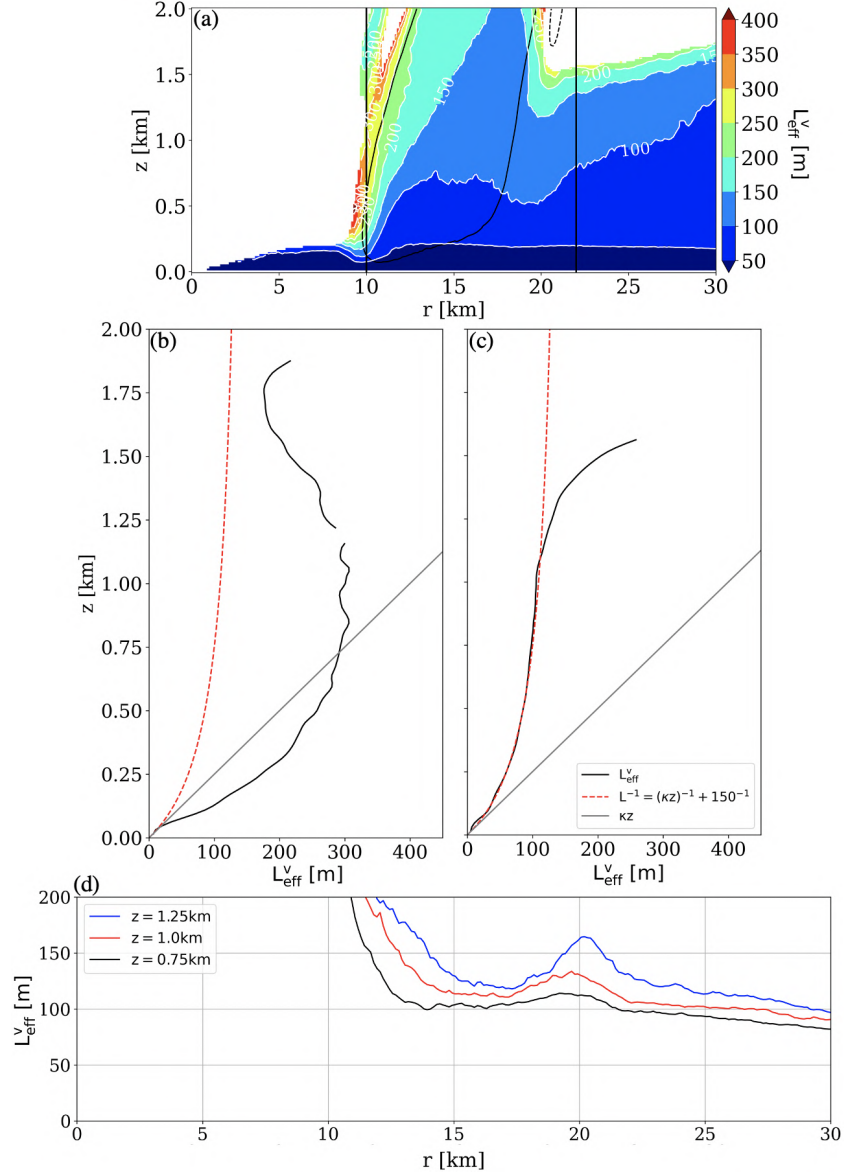


Figure 3.10. Plots of the effective mixing length ( $L_{\text{eff}}^v$ ) in meters. (a) Radius–height plot. (b)–(c) Vertical profiles of  $L_{\text{eff}}^v$  (black line) and analytical Louis-type profiles (red dashed lines, with  $L_{\infty} = 150$  m) and the Prandtl theoretical surface layer relations (gray line) at (b)  $r = 10$  km and (c)  $r = 22$  km. (d) Radial variation of  $L_{\text{eff}}^v$  at  $z = 0.75, 1.0$  and  $1.25$  km (black, red and blue lines respectively). [The black vertical lines in (a) indicate the locations of the profiles in (b) and (c). The solid and dashed black contours in (a) indicate  $\langle w \rangle$  at  $\pm 1.0$  m/s.]

tuting the effective eddy viscosity (3.7) for the LHS:

$$L_{\text{eff}}^v = \left( K_{\text{eff}}^v / \sqrt{(\partial \langle u \rangle / \partial z)^2 + (\partial \langle v \rangle / \partial z)^2} \right)^{1/2} \quad (3.9)$$

The result (Fig. 3.10a) shows that at  $r > 11\text{km}$ ,  $L_{\text{eff}}^v$  increases monotonically with height from 0 at the surface to  $\approx 100\text{m}$  from 1 km above the surface. A vertical profile of  $L_{\text{eff}}^v$  taken at  $r = 10\text{km}$  is shown in Fig. 3.10b, revealing a non-monotonic behavior with height, and relatively high values of  $L_{\text{eff}}^v$  ( $\approx 300\text{m}$ ) between  $z \approx 500\text{m}$  and  $1000\text{m}$ . On the other hand, a vertical profile of  $L_{\text{eff}}^v$  at  $r = 22\text{km}$ , shown in Fig. 3.10c, indicates that the effective mixing length increases more slowly and monotonically from  $\approx 0\text{m}$  at the surface to about  $\approx 100\text{m}$  at  $z \approx 500\text{m}$ , where it remains constant with height up until  $z \approx 1\text{ km}$ . Above  $z \approx 1000\text{m}$ , at the location of this vertical profile, the value of  $L_{\text{eff}}^v$  increases sharply (possibly due to the decreasing vertical wind shear at the exact same location seen in Fig. 3.7b and Fig. 3.8b) until it becomes undefined. This region also coincides with the top of the inflow layer (Fig. 3.4b). The range ( $\approx 35 - 55\text{m}$ ) of  $L_{\text{eff}}^v$  estimated by [246] is comparatively smaller (about half) of the LES derived values from outside the eyewall ( $r \approx 22\text{km}$  and  $0\text{km} \leq z \leq 1.0\text{km}$  – Fig. 3.10c) in the present study, most likely due to the relatively low surface wind regime (18m/s to 30m/s) between the TC outer rainbands where their data were collected. [251] estimated vertical mixing lengths of  $\approx 100\text{m}$  in the eyewall region of Hurricane Hugo (1989) and Allen (1980) at  $\approx 450\text{-}500\text{m}$  flight height.  $L_{\text{eff}}^v$  from our study, in the eyewall region (see Fig. 3.10a), agrees well with the observational estimates by [251]. We also note that [251] documented, with some caveats (i.e., including flight segment cutting through the eyewall vorticity maxima [EVM]), vertical mixing length of  $\approx 220\text{m}$  from eyewall-penetrating flight legs into Hurricane Hugo (1989).  $L_{\text{eff}}^v$  from our study indeed approaches and exceeds  $\approx 220\text{m}$  at the inner edge of the eyewall. In this sense, the present study provides guidance on the vertical and horizontal

distribution of  $L_{\text{eff}}^v$  in the most intense region of the TC environment.

Various analytical estimates of  $L_{\text{eff}}^v$  have been formulated and employed in the parameterization of TC boundary layer behaviour [19, 123, 135, 23, 100]. A widely used PBL model, the Louis scheme, often uses the formulation in Eq. (3.10) and is based on [19]:

$$\frac{1}{L} = \frac{1}{\kappa z} + \frac{1}{L_{\infty}}, \quad (3.10)$$

where  $\kappa$  and  $L_{\infty}$  represent the von Kármán constant ( $\approx 0.4$ ) and the asymptotic length scale (prescribed by the user), respectively.

In Fig. 3.10c, we find that the analytical formulation using  $L_{\infty} = 150\text{m}$  (red dashed line) captures well the vertical variation of the effective mixing length ( $L_{\text{eff}}^v$ ) outside the eyewall, from the surface to  $z \approx 1000\text{m}$ . Interestingly, this same value ( $\approx 150\text{m}$ ) for  $L_{\infty}$  was recommended in one of the earliest reformulations of the Louis scheme [124]. In their study, [246] found that a large number of estimated  $L_{\infty}$  values fall between 40 – 80m – also about half of  $L_{\infty} = 150\text{m}$  seen to be a reasonable fit in the present study at  $r \approx 22\text{km}$ , Fig. 3.10c – although a few values as high as  $\approx 140\text{m}$  were found. This discrepancy between our results and [246] could be a consequence of multiple factors, including the sample size used in their study, the intensity of different storms on which the analyses were based as well as the proximity to the intense eyewall region. A comparison of the Prandtl theoretical surface layer relation, [168] (grey line in Fig. 3.10c) and the model computed  $L_{\text{eff}}^v$  (black line), indicates that the simulation roughly captures the behaviour of the theory very close to the ground — an expected behaviour widely seen in simple boundary layer flows [180, 190, 19, 17] — above which the model-derived value approaches an asymptotic value.

However, in the inner eyewall (Fig. 3.10b), the Louis scheme profile with  $L_{\infty} \approx 150\text{m}$  does not capture the vertical variation of  $L_{\text{eff}}^v$  found in the present study, even qualitatively.  $L_{\text{eff}}^v$  from the present study (black solid line) is consistently higher than the analytical profile across most of the BL height, suggesting that the widely used

asymptotic formulation of the effective mixing length (Eq. (3.10)) under-predicts the magnitude of the effective mixing length in the most intense regions of the TC. Furthermore, unlike outside the eyewall (Fig. 3.10c),  $L_{\text{eff}}^v$  seen here is notably larger than the Prandtl surface layer relation (grey line) as  $z$  increases from the ground up until  $z \approx 0.75\text{km}$ . These results suggest that the nature of turbulence in the corner flow of the TC eyewall may be fundamentally distinct from traditional boundary layer turbulence. We suspect that contributions from *horizontal* gradients, which can be quite strong in hurricane eyewalls but are neglected in traditional boundary layer equations, are probably responsible for these different results in the corner-flow region.

Fig. 3.10d shows the radial variation of  $L_{\text{eff}}^v$  at  $z = 0.75, 1.0$  and  $1.25\text{km}$  (black, red and blue solid lines respectively). At all heights, outside the eyewall ( $r > 20\text{km}$ ),  $L_{\text{eff}}^v$  is seen to decrease steadily with increasing radii, with values generally less than  $120\text{m}$ . In the inner half of the eyewall ( $r < 15\text{km}$ ), however,  $L_{\text{eff}}^v$  increases rapidly with decreasing radii. This sharp increase in the magnitude of  $L_{\text{eff}}^v$  in the corner flow region is again attributed to the non-traditional behaviour of turbulence in this region relative to the inflowing boundary layer. The local peak in the values of  $L_{\text{eff}}^v$  at  $r = 20\text{km}$ , appears to be associated with the downdraft feature (dashed black contour in Fig. 3.10a).

In most boundary-layer parameterization schemes, the horizontal momentum flux  $\langle u'v' \rangle$  is assumed to be smaller than the vertical momentum fluxes  $\langle u'w' \rangle$  and  $\langle v'w' \rangle$  [e.g., 130]. However, in the corner flow region of the storm, [248] suggest that horizontal mixing may become just as important as vertical mixing in terms of its effect on the vortex dynamics (this is confirmed in the analyses of the flux divergences presented in Fig. 3.5). [23], [181], and [21] pointed out the importance of horizontal momentum diffusion and associated mixing lengths on the maximum intensity of simulated storms. Comparing Fig. 3.11a to Fig. 3.7a and Fig. 3.8a, it is seen that in the

corner flow region, the horizontal momentum flux is significantly ( $\approx 3$  times) greater than the vertical momentum fluxes. Figs. 3.11a and b also show that regions of positive horizontal momentum flux correspond to regions of negative radial gradient  $\left(r \frac{\partial}{\partial r} \frac{\langle v \rangle}{r}\right)$ , again confirming mostly down-gradient transport of horizontal momentum.

Interestingly, a plot of the effective radial eddy viscosity ( $K_h = -\langle u'v' \rangle / r \frac{\partial}{\partial r} \frac{\langle v \rangle}{r}$ ) in Fig. 3.11c shows that the regions of counter-gradient fluxes (blue shading; negative values of eddy viscosity) are located close to the surface region ( $z \leq 100\text{m}$ ) and near the inner edge of the eyewall ( $r \approx 10\text{--}11\text{km}$ ), extending up to the top of the boundary layer ( $z \approx 2\text{km}$ ). For the near-surface region, where the magnitude of negative eddy viscosity is comparatively smaller, the counter-gradient fluxes are clearly seen to be below the height of maximum radial inflow (black dashed contour in Fig. 3.7a) where momentum is most likely being lost to the surface due to friction. For the region near the inner edge of the eyewall, however, the counter-gradient flux signatures do not entirely coincide with weak radial gradient zones, and are comparatively significant in magnitude and spatial extent at the top of the BL. Again, we note that the contributions of the turbulent tendency to the mean flow (Fig. 3.5c) around the region where the counter-gradient fluxes are found here, is not substantial and thus may not significantly influence the storm mean wind field. A closer look at the mean radial velocity field (black contour in Fig. 3.7a) reveals that this region of counter-gradient flux at the top of the BL actually coincides with the outflow region. This result would imply that the counter-gradient fluxes seen in this region (Fig. 3.11c) may be related to large eddies that span the interface between the weak negative inflow region and the outflow at the top of the HBL. Furthermore, the counter-gradient flux signatures slightly inwards of the inner edge of the eyewall ( $r < 10\text{km}$ ), extending from the surface to top of the BL, could also be related to large eddies at inner edge of the eyewall (Fig. 3.3a).

A comparison of the magnitudes of  $K_h$  with  $K_z^u$  and  $K_z^v$  in Fig. 3.11c, Fig. 3.7c,

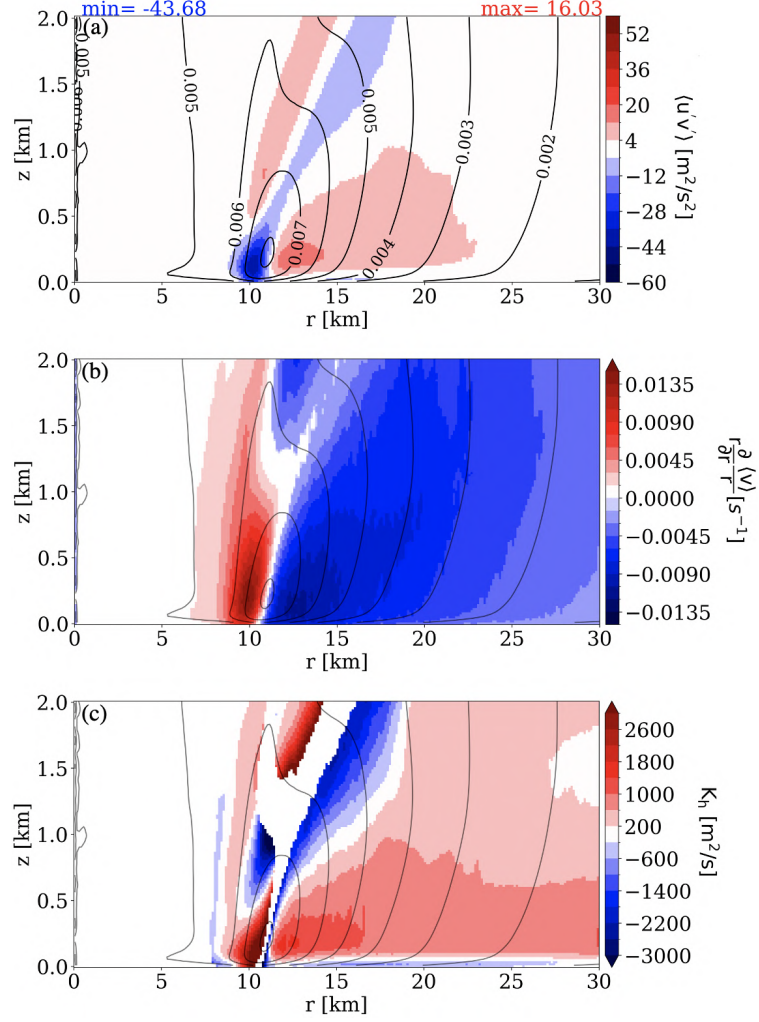


Figure 3.11. Contour plots of  $\frac{\langle v \rangle}{r}$  in  $[s^{-1}]$ , overlain by shadings of (a) azimuthally and time-averaged radial fluxes of tangential velocity  $\langle u'v' \rangle$  in  $[m^2 s^{-2}]$ , (b)  $r \times$  the radial gradient of rotation rate  $r \frac{\partial \langle v \rangle}{\partial r}$  in  $[s^{-1}]$  and (c) the effective eddy viscosity,  $K_h$  in  $[m^2 s^{-1}]$ . [Plots (b) and (c) use the same contour interval for  $\frac{\langle v \rangle}{r}$  as in (a).]

and Fig. 3.8c, respectively, suggests the anisotropic nature of turbulence processes in the corner flow region of a TC. The values of  $K_h$  found in the present study are similar to the observation measurements ( $\approx 1500 m^2 s^{-1}$ ) recorded by [248] using aircraft measurements flown at about  $\approx 500 m$  height into the eyewall of three intense storms (Category 5 – Hurricane David [1979], Category 4 – Hurricane Allen [1980] and Cat-

egory 5 – Hurricane Hugo [1989]). This result confirms the importance of horizontal diffusion in the corner flow region of the hurricane boundary layer, supporting the findings from previous observational [248] and numerical [23, 21, 247] studies.

In summary, the down-gradient eddy viscosity hypothesis is valid in most of the boundary layer according to this simulation, although regions of counter-gradient fluxes are noted in regions of weak gradient near the eyewall and inflow layer top. The magnitude and spatial distribution of  $K_h$  also indicates that the down-gradient hypothesis is largely valid, except for certain regions within the eyewall. That said, in the context of the turbulence tendencies (shown in Fig. 3.5), we find that these counter-gradient regions may not actually significantly alter the mean fields. A more systematic study of counter-gradient fluxes in the HBL [possibly using higher order closure models [e.g., 157] or mass-flux schemes [77, 33]], in addition to novel high-resolution observations, would be needed to further clarify this conclusion.

### 3.3.4 A Revised Formulation Of Eddy Viscosities

The simple parameterization of radial flux (3.6) only considers the shear stress term  $\langle u'v' \rangle$ . However, (3.1)-(3.3) indicates that this is not the only turbulent stress term acting in the radial direction (see Fig. 3.5a) — terms containing  $\langle u'^2 \rangle$  and  $\langle v'^2 \rangle$  also influence the mean flow. Thus, the eddy viscosity  $K_h$  shown previously in Fig. 3.11 only accounts for a portion of the radial turbulence transport. A similar approximation was made by Zhang and Montgomery [248].

In their axisymmetric numerical model, RE87 developed and presented relationships for separate eddy viscosities in the radial and vertical directions. They noted following [134] that having a significantly larger horizontal grid spacing (compared to the vertical) necessitates the need for different parameterizations in these two directions in mesoscale models. In the present study, with the turbulent stresses mostly resolved in the corner flow region (and the horizontal grid spacing being similar to

the vertical), we can evaluate their formulations for an effective radial eddy viscosity which includes all components of the Reynolds stresses relevant to mixing in the radial direction.

Following RE87 (pg. 545), we form a turbulent kinetic energy equation assuming equilibrium conditions, i.e., a balance between production and dissipation. For the radial direction, we have

$$-\langle u'v' \rangle r \frac{\partial}{\partial r} \frac{\langle v \rangle}{r} - \langle u'^2 \rangle \frac{\partial \langle u \rangle}{\partial r} - \langle v'^2 \rangle \frac{\langle u \rangle}{r} - \langle w'^2 \rangle \frac{\partial \langle w \rangle}{\partial z} = \epsilon. \quad (3.11)$$

The production terms [LHS of (3.11)] are essentially the same as those leading to RE87's equation (29), except for two important differences: 1) we do not invoke any parameterization for the Reynolds stresses, and 2) we include a term with  $\frac{\partial \langle w \rangle}{\partial z}$ , which is needed for consistency in the complete stress tensor [e.g., 221].

Next, as in RE87, we assume based on dimensional grounds that dissipation has the form

$$\epsilon = (K_{\text{eff}}^h)^3 / l_h^4 \quad (3.12)$$

where  $K_{\text{eff}}^h$  is an effective eddy viscosity in the radial direction, and  $l_h$  is an associated effective length scale. Further, we assume  $l_h$  is related to  $K_{\text{eff}}^h$  and the horizontal deformation  $S_h$  via a traditional ‘‘Smagorinsky’’ model,

$$K_{\text{eff}}^h = l_h^2 S_h, \quad (3.13)$$

where  $S_h^2 \equiv \left( r \frac{\partial}{\partial r} \frac{\langle v \rangle}{r} \right)^2 + 2 \left[ \left( \frac{\partial \langle u \rangle}{\partial r} \right)^2 + \left( \frac{\langle u \rangle}{r} \right)^2 + \left( \frac{\partial \langle w \rangle}{\partial z} \right)^2 \right]$ . Using (3.13) to eliminate  $l_h$  from (3.12), the resulting equation for the RHS of (3.11) leads to a relation for

effective horizontal eddy viscosity:

$$K_{\text{eff}}^h = \frac{\left( -\langle u'v' \rangle r \frac{\partial \langle v \rangle}{\partial r} - \langle u'^2 \rangle \frac{\partial \langle u \rangle}{\partial r} - \langle v'^2 \rangle \frac{\langle u \rangle}{r} - \langle w'^2 \rangle \frac{\partial \langle w \rangle}{\partial z} \right)}{\left[ \left( r \frac{\partial \langle v \rangle}{\partial r} \right)^2 + 2 \left( \frac{\partial \langle u \rangle}{\partial r} \right)^2 + 2 \left( \frac{\langle u \rangle}{r} \right)^2 + 2 \left( \frac{\partial \langle w \rangle}{\partial z} \right)^2 \right]}. \quad (3.14)$$

This formulation now includes contributions from all terms associated with turbulence tendencies in the radial direction. It reduces to (3.6) if all terms except those with  $\langle u'v' \rangle$  and  $r \frac{\partial \langle v \rangle}{\partial r}$  are neglected.

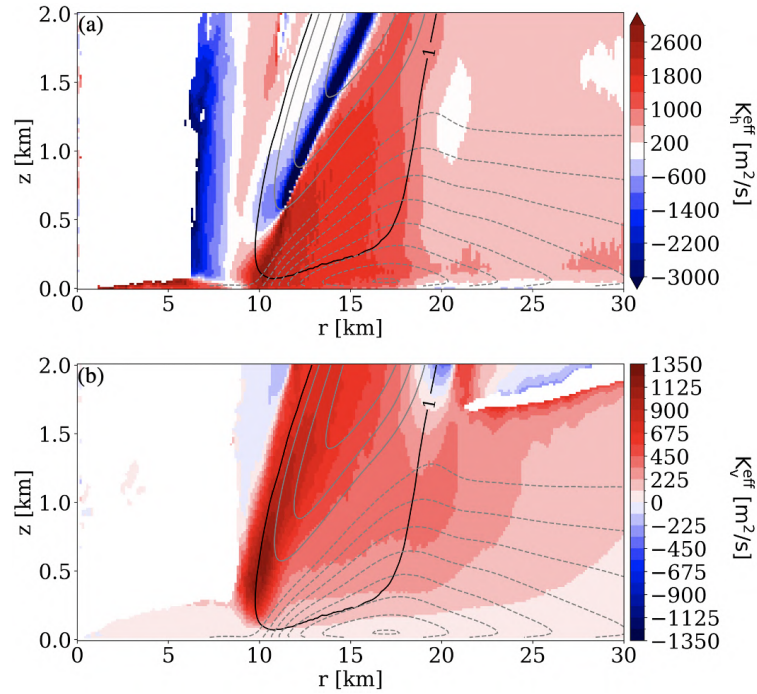


Figure 3.12. Plots of (a) effective radial eddy viscosity,  $K_{\text{eff}}^h$  in  $[m^2s^{-1}]$  using (3.14) and (b) effective vertical eddy viscosity,  $K_{\text{eff}}^v$  in  $[m^2s^{-1}]$  using (3.15). The solid black contour line in each panel indicates  $\langle w \rangle$  of +1.0m/s, highlighting the eyewall region. The solid and dashed gray contour lines in each panel show the mean radial velocity  $\langle u \rangle$ , using the same contour interval as in Fig. 3.7(a).

Fig. 3.12a shows a plot of  $K_{\text{eff}}^h$  determined using (3.14). This result is much less complicated than that shown in Fig. 3.11c, particularly in the eyewall. Fig. 3.12a also shows that the down-gradient eddy viscosity hypothesis is valid for most of the HBL, except in two thin regions: within the eye (where the blue shading extends from the surface to the top of the plot); and within the inner edge of the eyewall for  $z > 500$  m. For the region in the eye, the counter-gradient radial flux region has negligible effect on the mean flow, since the turbulent tendencies there are so small (Fig. 3.5). We also note that the location and scale of the counter-gradient flux signature seen in the eye suggest that they are possibly related to the coherent turbulent structures seen in Fig. 3.2 & 3.3 and in a recent work by [171]. For the eyewall, the counter-gradient fluxes seem to reside above the inflow layer (dashed gray contour lines) and may be related to the transition from an inflowing to outflowing flow pattern in the TC eyewall; in other words, there may be a turbulence “memory” effect (see [83]) as air parcels move through the corner-flow region.

Following a similar procedure, an effective eddy viscosity in the vertical direction can be derived:

$$K_{\text{eff}}^v = \frac{\left(-\langle u'w' \rangle \frac{\partial \langle u \rangle}{\partial z} - \langle v'w' \rangle \frac{\partial \langle v \rangle}{\partial z}\right)}{\left[\left(\frac{\partial \langle u \rangle}{\partial z}\right)^2 + \left(\frac{\partial \langle v \rangle}{\partial z}\right)^2\right]}. \quad (3.15)$$

The result, shown in Fig. 3.12b, is quite similar to the previous result (shown in Fig. 3.9a), except that this newer formulation allows for the existence of counter-gradient flux regions. Furthermore, the magnitudes of both formulations are quite similar (with the Fig. 3.9a being slightly higher). From Fig. 3.12b, the down-gradient eddy viscosity hypothesis is again seen to be valid in most of the BL, while small regions of counter-gradient flux signatures are seen above the inflowing BL, outside the eyewall and slightly inward of the inner eyewall ( $z \geq 1\text{km}$ ).

### 3.4 Conclusions and Discussion

Turbulence in the inner core of an idealized Category 5 Hurricane is analysed using large eddy simulation (LES) model output with a horizontal grid size of 31.25m. Intense updrafts/downdrafts with a vertical scale  $\approx 1.5 - 2.5$ km scales, similar to those seen in research flight missions into intense Category 4/5 storms, are ubiquitous at the inner edge of the eyewall, decreasing in vertical extent with radial distance from the storm center. The role of turbulence on the mean momentum fields is shown to be primarily down-gradient in nature. Azimuthally and time-averaged momentum flux provide insights into the nature of turbulent fluxes in the HBL, which are summarized below:

1. Turbulent eddy tendencies in the inner core (i.e., eye, eyewall, and nearby rainbands) of intense hurricanes primarily act diffusively on the mean velocity fields, acting to weaken the strength of the eyewall, decreasing the mean radial inflow and the updraft strength in the corner flow region of the eyewall.
2. In most of the HBL, the down-gradient hypothesis is valid for vertical and horizontal momentum fluxes  $\langle u'w' \rangle$ ,  $\langle v'w' \rangle$  and  $\langle u'v' \rangle$ . Near the top of the boundary layer, a distinct counter-gradient region is noted for  $\langle v'w' \rangle$  where the vertical gradient of tangential velocity  $\frac{\partial \langle v \rangle}{\partial z}$  is weak. Similarly, for the horizontal momentum flux  $\langle u'v' \rangle$ , counter-gradient flux signatures are seen in parts of the eyewall. However, their effect on the mean wind field is minimal, as they are around zones where the relevant turbulent tendencies in the mean budget equations are negligible. We note that the azimuthally averaged results presented in this study apply most directly to axisymmetric models, and thus applicability to 3D NWP models is unclear.
3. Analytical formulations for  $L_{\text{eff}}^v$ , used in the Louis scheme, is shown to perform well outside the eyewall, but underestimates the LES derived values by about half in the inner edge of the inner eyewall. Additionally, we provide estimates of the effective vertical mixing lengths ( $L_{\text{eff}}^v$ ) in the most intense regions of TCs.
4. A complete formulation of the effective horizontal eddy viscosity (accounting for typically ignored stress terms) is presented, showing the validity of the down-gradient eddy viscosity hypothesis in most of the HBL, except along a narrow regions in the eye and at the eye-eyewall interface.

From our findings, we propose a simple conceptual framework for understanding

the role of turbulence in the hurricane boundary layer: the mean velocity field brings in air parcels from the outer eyewall, converging in the inner eyewall which acts as a frontal system for angular momentum and entropy [58]. It should be noted that the argument for the frontogenetic nature of the TC eyewall–eye transition was previously suggested by [52] pg. 286, [164] pg. 486 but more rigorously shown by [58]. In the inner eyewall, we find that turbulent eddies act to diffuse momentum. We show, unambiguously, that turbulence acts to weaken the frontal gradient (eyewall), enhancing mixing into the eye, while simultaneously weakening the strength of radial inflow. The divergence of the turbulent momentum fluxes is more pronounced in the eyewall but is notable in the inflowing boundary layer as well. The complex distribution of effective eddy viscosity in the eyewall re-emphasizes the need for a more complete parameterization of turbulent momentum fluxes in this region for mesoscale forecast models [183], which should account for horizontal gradients and associated turbulent fluxes [e.g.,  $\langle u'v' \rangle$ ,  $\langle u'u' \rangle$ , and  $\langle v'v' \rangle$ ].

Understanding the magnitude and distribution of turbulent fluxes in the eyewall region and the HBL in general is the subject of ongoing research and remains highly relevant for a better understanding of intensity changes in hurricanes. The recent use of small uncrewed aircrafts systems (sUAS) in the inner core of intense storms shows great potential in complementing the use of manned-aircraft missions [39]. Although this study presents results for a single intense TC, we have shown that turbulence (which remains largely parameterized in current weather forecast models) plays a non-negligible role in the modification of the TC mean wind fields. The role of turbulence on temporarily evolving (i.e., intensifying/weakening) storms remain to be clarified. Possible future research opportunities thus lie in the investigation of the evolution of TC turbulence under moderate to strong vertical wind shear.

### 3.5 Acknowledgments

We acknowledge useful personal correspondence with Dr. Stephen Guimond and Dr. Ralph Foster. We also acknowledge ONR grants N00014-19-S-B001 to the University of Notre Dame and N00014-20-1-2071 to NCAR/UCAR for financial support under the Tropical Cyclone Rapid Intensification (TCRI) campaign. George Bryan, Richard Rotunno, and Peter Sullivan were also supported by the NSF under Cooperative Agreement No. 1852977. We also acknowledge high-performance computing support from Cheyenne (doi:10.5065/D6RX99HX) provided by NSF NCAR's Computational and Information Systems Laboratory. Finally, the corresponding author would like to recognize the NCAR Advanced Study Program (ASP) Graduate Visitor Program (GVP) from which a collaborative research visit to NCAR was supported.

## CHAPTER 4

### NEAR-SURFACE COHERENT STRUCTURES IN AN INTENSE TROPICAL CYCLONE: CONDITIONAL EDDIES AND VERTICAL MOMENTUM FLUXES

The research in this chapter was carried out in collaboration with George H. Bryan, Peter P. Sullivan, and David H. Richter. It is planned for submission to the Journal of Fluid Mechanics (JFM) soon.

#### 4.1 Introduction

Traditional approaches to turbulence research in meteorology, involving Reynolds averaging and other eddy-mean partitioning methodology, only ever address turbulence in the *mean* sense; rarely confronting the intermittency of coherent turbulent structures and their potential roles. We ask: in the context of hurricane dynamics, how much of our current understanding of the role of turbulence remains constrained by this bulk treatment of turbulent processes? This question becomes increasingly pertinent in the face of various observational evidence of organized turbulent structures in the hurricane boundary layer (HBL).

The first observational evidence of coherent structures in the HBL was reported by [238] in their study of Hurricane Fran (1996). Using the high resolution Doppler on wheels (DOW) ( $\approx 75\text{m}$  resolution), they noted the presence of sub-kilometer scale roll vortices, approximately aligned with the mean tangential winds. In the years since that paper was published, the improvement of remote sensing technologies enabled the identification of HBL roll vortices in ground-based doppler radars [151, 121], spaceborne sythentic aperture radar (SAR) imagery [111, 88, 89, 41] and aircrafts

[249, 212]. A rigorous examination of such structures and a theoretical framework for their prediction was presented by [64], using linear stability theory. Several modeling studies [156, 67, 68, 70, 69, 112, 110] have since been carried out in an attempt to understand the origin and influence of roll vortices in the HBL, with a growing consensus on their role in enhancing momentum fluxes. Although roll vortices appear to be the most discussed form of coherent structure in the HBL, several other types have also been documented e.g., inner-core fingers/striations [20, 2, 218], mesovortices [106, 105, 237, 8], tornado scale vortices [237], coherent turbulent eddies [75, 171] etc.

The study of coherent structures in the near-wall turbulent region, however dates farther back to its first mention by [215, 216] when *horse-shoe*-like vortex filament structures were investigated using smoke visualizations and shown to participate actively in fluid transport. Reports of streaks (zones of comparatively weak stream-wise momentum) in the near wall region were then presented by [102] using their Hydrogen bubbles experiments. Thereafter, [217] proposed the *attached eddy* phenomenology for dominant structures in the turbulent near-wall region, defining "active motions" as ones leading to strong correlations in turbulent velocity components, producing Reynolds stress. Using large eddy simulation (LES), a series of studies by [142, 143, 101] showed, for the first time, the existence of hairpin vortices and omega ( $\Omega$ ) like structures in instantaneous fields of a turbulent channel flow. The direct numerical simulation (DNS) of a low Reynolds number boundary layer [201] was extensively analyzed by [174, 176], thereafter noting the presence of a suite of structures: quasi-streamwise vortices (rolls) and archs with the horse-shoe/hairpin vortices being less frequently seen as previously suggested. Several studies have since then explored the existence of coherent structures in a variety of simple wall-bounded engineering turbulent flows, emphasizing the roles they play in enhancing momentum transport [91, 15, 198, 78, 16, 125, 59, 73, 192, 224]. However, these evidences for the prevalence of coherent structures in simple flows do not imply the existence of similar structures

in more complex, realistic environmental flows.

Using a LES, [113] investigated the dynamics of coherent structures in a neutrally stratified planetary boundary layer (PBL), documenting the existence of coherent vortical structures (horse-shoe & quasi-streamwise) and their relationship to intense momentum fluxes. Along the same lines, [65] showed that the coherent structures associated with extreme vertical momentum fluxes were closely related to the streaks seen in their 3D LES of a neutrally stratified atmospheric boundary layer (ABL). Recently, [187] showed that the inclusion of a velocity scale for Large and Very Large Scale Motions (LSMs and VLSMs) in a revised formulation of the Monin-Obukhov similarity theory (MOST) led to an improvement in the prediction of the atmospheric surface layer flux-gradient relationship, even though it had been previously noted by [196] that models without explicitly resolved coherent structures accurately predict the mean Reynolds stress profiles. In much more complex flow regimes where coherent structures produced by the mean flow can be advected over considerable distances (e.g., in hurricanes – Fig. 4.1), the prediction of momentum flux transport may be inaccurate without the explicit inclusion of the role of coherent structures. A similar idea was also alluded to by [86] pg. 31.

The current study, thus, aims at understanding the relationship between coherent structures and intense vertical momentum flux occurrence in the HBL. To the authors’ knowledge, this is the first time that a treatment of the kinematics of coherent structures – and their relationship to Reynolds Stress occurrence in different regions of the HBL – have been presented in a turbulence resolving simulation of a hurricane. It is the hope of the authors’ that this study would rekindle interests in the possible inclusion of the role of coherent structures in revised formulations of near-surface flux-gradient relationships in complex terrains. To this end, we pose the following research question: What form do the coherent structures responsible for extreme Reynolds stress events take, and how do they vary with storm location?

## 4.2 Methodology

### 4.2.1 Numerical Model And Dataset Description

This study uses a dataset from the LES of an idealized Category 5 hurricane detailed in [232], [204], [206], [172] and [162]. The Cloud Model 1 (CM1) [22, 23] was used with horizontal and vertical grid spacing of  $\Delta x = \Delta y = 31.25\text{m}$ ,  $\Delta z = 15.625\text{m}$  respectively, utilizing the eddy injection methodology described in detail in [24].

We focus on a 1hr evolution of the storm at steady state intensity, within a  $\approx 50\text{km} \times 50\text{km}$  subset (Fig. 4.1(a)) of the full LES subdomain  $80\text{km} \times 80\text{km}$  (see Figure 1 of [162]). We analyze 61 snapshots of simulation output (1 minute temporal frequency) for the discussions herein. Figure 4.1 shows a horizontal section of the vertical velocity field  $w$  [m/s] at  $\approx 700\text{m}$  height, showing the variety of resolved turbulent structures in the model output. These structures are qualitatively similar to those documented observationally (see a more detailed discussion in [162]). Figures 4.1(b)-(c) shows the windowed-in views of the radial variation in the organization of turbulent structures (in the vertical velocity field at  $\approx 700\text{m}$  height) between the inflowing boundary layer (Fig. 4.1(b)) and the eye-eyewall region (Fig. 4.1(c)). We note that in Fig. 4.1(b), the streaky pattern of turbulence organization is visible and has been documented extensively in marine atmospheric boundary layer (MABL) [226, 227, 207]. In Fig. 1(c) however, the vertical velocity field is less linearly organized, possibly due to the increased tangential velocity (compared to the radial velocity) and vertical velocity in the near-eyewall region. Qualitatively speaking, there is a clear transition in the flow regime between Fig. 4.1(b) and Fig. 4.1(c). The isosurfaces of vertical velocity ( $w = -8\text{ms}^{-1}$ ), in Fig. 4.2, shows the temporal evolution of one prominent coherent velocity structure (identified in Fig. 4.1(c)) over  $\approx 1\text{min}$  duration. Fig. 4.2 shows clearly that there is a continuous cycle of "merging" and "disintegration" of turbulent structures in the eyewall of the simulated Tropical Cyclone (TC), supporting arguments for the

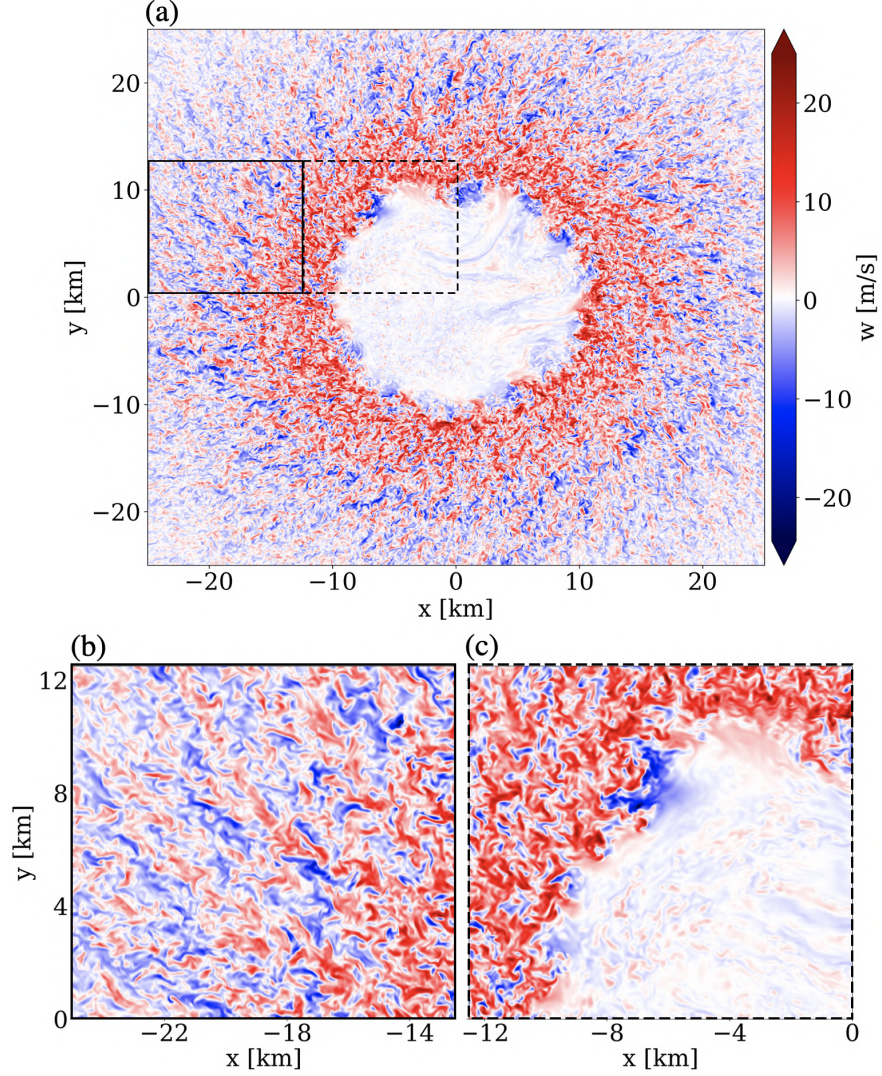


Figure 4.1. (a) Horizontal cross section of the vertical velocity field at  $z \approx 700\text{m}$ . (b) and (c) show windowed-in regions of the N-W quadrant illustrating the organization of turbulent velocity structures in the outer eyewall and eye-eyewall interface respectively. [A plane view of the 3D vertical velocity isosurface (for (c)) is shown in Fig. 2 below (bottom-center panel i.e.,  $T_4$ )].

intermittency of coherent structures. These velocity structures are most certainly qualitatively intriguing, however, the present study will be focussed on near-surface Reynolds stresses, as they are more relevant to the description of turbulence in the HBL.

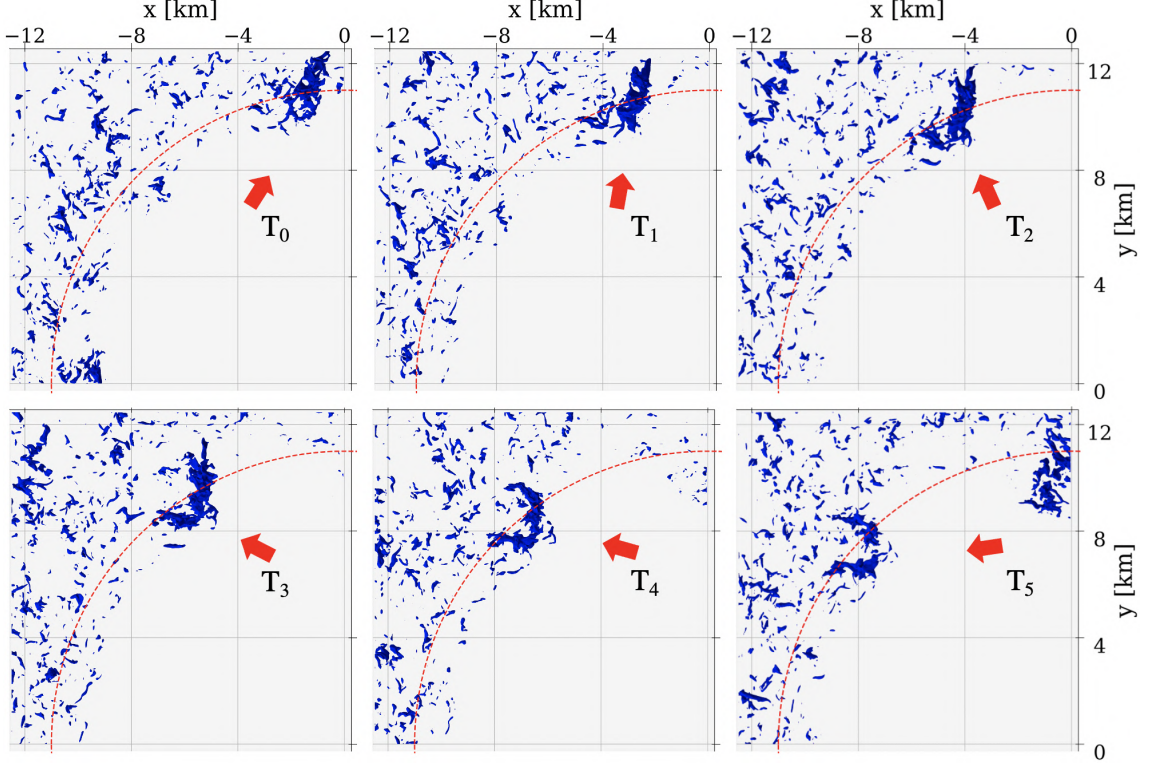


Figure 4.2. Three-dimensional isosurfaces (plan view) of instantaneous velocity structures (i.e., intense downdrafts with  $w = -8 \text{ m s}^{-1}$ ) advected – from  $T_0$  to  $T_5$  – along the eye-eyewall interface of the simulated Category 5 hurricane. The interval between each time step ( $\Delta T$ ) is 20s and the red-dashed line in all panels marks  $r \approx 11 \text{ km}$ , indicating the eye-eyewall interface. [The bottom-center panel, marked  $T_4$ , shows the same time instance as Fig. 1(c) above].

For the analyses presented in this study, all 61 snapshots of instantaneous fields ( $\chi(x, y, z, t)$ ) are first time averaged in the native cartesian coordinate, after which the turbulent fields are obtain by subtracting the time-mean field from each instantaneous fields  $\chi' = \chi - \langle \chi \rangle$ . These turbulent fields are then interpolated into a cylindrical coordinates with radial grid points of  $r = \Delta x, 2\Delta x, 3\Delta x \dots$  to  $r \approx 30 \text{ km}$ . There are about 6800 data points at each radii in the azimuthal direction after interpolation, sufficiently sampling the space which serve as data points. These interpolated turbulent fields (in cylindrical coordinates) are then used for our analyses.

#### 4.2.2 Conditional Averaging and Compositing

The closure problem in the Reynolds Averaged Navier-Stokes (RANS) momentum equations (see Eqns. 1 – 3 in [162]) necessitates the approximation of the ensuing averaged correlation between the turbulent velocity components (i.e.,  $\langle u'w' \rangle$ ,  $\langle v'w' \rangle$ ,  $\langle u'v' \rangle$ ,  $\langle u'u' \rangle$ ,  $\langle v'v' \rangle$ ,  $\langle w'w' \rangle$ ), unlike in LES/DNS where these terms are resolved. The divergences of these correlation terms have been shown to play a significant role in modulating the TC mean wind fields, as clearly shown in [162]. Furthermore, seeing that the product of the average of this correlation terms (Reynolds stresses) and the mean velocity gradient is responsible for the turbulence production (in the turbulent kinetic energy budget equation), a study of the kinematics of extreme Reynolds stress occurrences could provide insights on the production of turbulence in the HBL.

The idea that the nature of eddies which produce Reynolds stresses could be deduced by analysing the average flow field around a point in the flow, was promoted by [5]. Thus, by conditionally averaging the field around extreme Reynolds stress events, one can extract a "conditional eddy" representative of the average field associated with the Reynolds stress occurrence. At this point, we would like to emphasize that the deduced conditional eddy structure is strongly dependent on the condition upon which the averaging is performed [4]. Although extreme Reynolds stress events is a common metric used in deducing conditionally averaged eddy structures [65, 125, 49, 126, 73, 128], several other metrics for conditional averaging have been used in the past including: pressure perturbations in vegetation canopy flows,  $p_T$  [62, 60, 13], inter-scale energy transfer,  $\Pi$  [79, 158, 87, 50, 228] etc. Seeing that the mechanism for the production of extreme Reynolds stress events is the focus of this study, it is imperative that we clearly define a "trigger" value to identify these events. We pick this trigger value – as the top 99.9 percentile – from the distribution of the Reynolds stresses at a given height and radii range of interest.

The methodology for conditional averaging used in this study follows a two-step

procedure:

(i) Identification of the extreme occurrences of vertical momentum fluxes ( $u'w'$ ,  $v'w'$ ): At a given height in the domain, values of instantaneous vertical momentum fluxes exceeding a given trigger value are identified. Upon identification, a  $1\text{km} \times 1\text{km} \times 0.3\text{km}$  rectangular volume is cut out. This volume of instantaneous turbulent field is centered around the extreme event, unless the height of analysis is close to the surface, in which case the volume lies above the extreme event. Grid points within this isolated volume are excluded from subsequent searches for more extreme Reynolds stress events. At the end of this procedure, a number of 3D volumes of instantaneous fields centered around extreme Reynolds Stress events are obtained.

(ii) Compositing: The 3D volumes of instantaneous turbulent fields from the above step are ensemble averaged in a new coordinate  $r'[\text{m}]$ ,  $\phi'[\text{m}]$ ,  $z'[\text{m}]$ . This ensemble averaged volume represents the conditional eddy, from which quantities like vorticity ( $\omega$ ), vortex identification criteria (e.g., Q-criteria) etc., are computed to further characterize the structure of the eddy.

## 4.3 Results

### 4.3.1 Near-surface mean velocity fields & turbulent fluxes

Before addressing the presence of coherent turbulent structures, we aim, first, to understand the mean wind conditions around the height where our analyses is focused ( $z \approx 63\text{m}$ ). For the discussions in the rest of this study, we divide this near surface region of the HBL into three distinct zones i.e., inner eyewall ( $r \approx 10 - 13\text{km}$ ), outer eyewall ( $r \approx 14 - 17\text{km}$ ) and inflowing BL ( $r \approx 22 - 30\text{km}$ ), based on behaviour of the mean velocity fields discussed below and the inflow angle (not shown).

Figure 4.3(a) shows a horizontal profile of the mean velocity components. The radial velocity ( $\langle u \rangle$  – red solid line) is seen to be entirely negative, indicative of

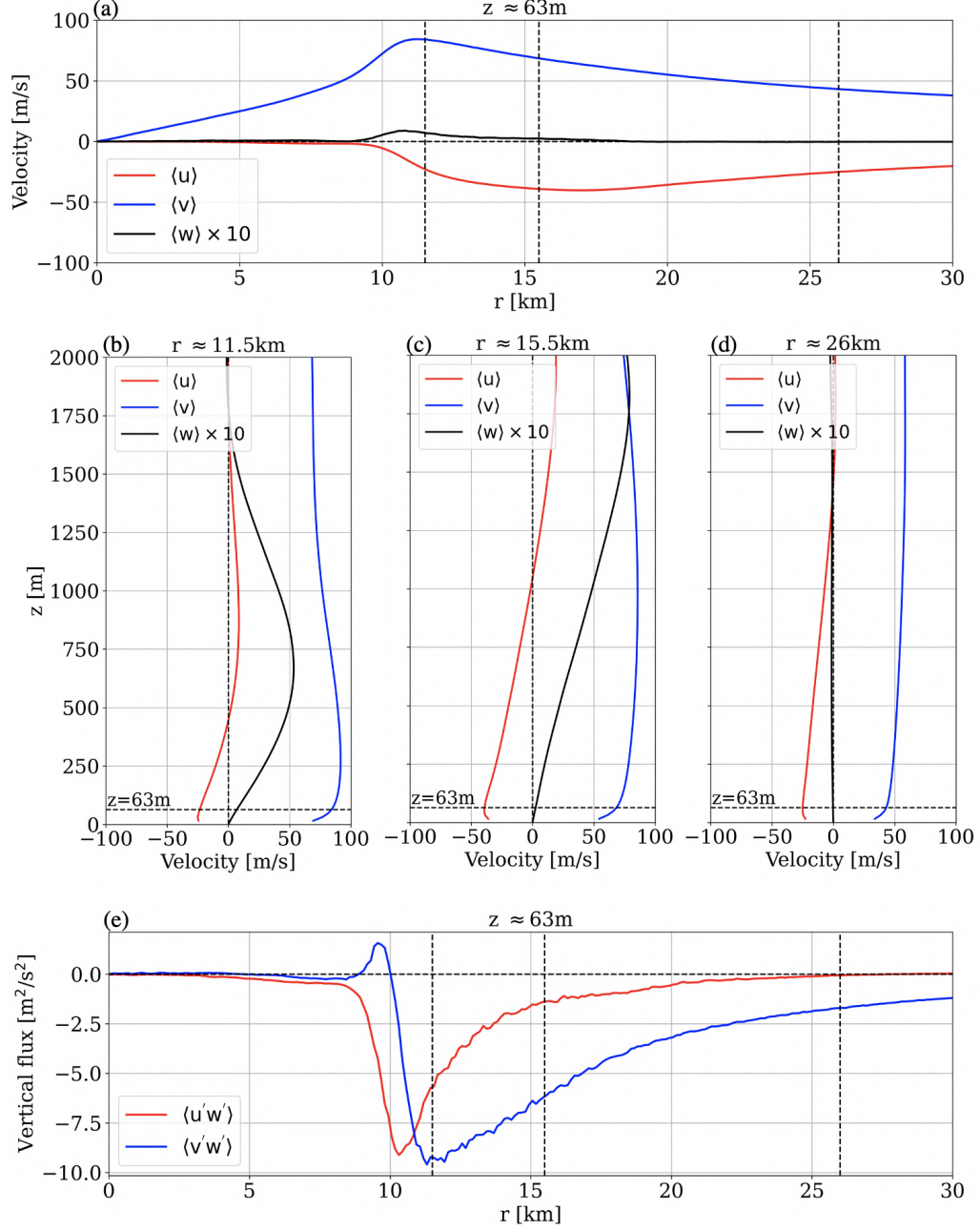


Figure 4.3. (a) Horizontal profiles of the azimuthally and time-averaged radial  $\langle u \rangle$  (solid red line), tangential  $\langle v \rangle$  (solid blue line) and vertical  $\langle w \rangle$  [multiplied by a factor of 10 for visibility] (solid black line) velocity components (all in m/s) at  $z \approx 63\text{m}$  height, with the dashed black lines indicating the radii (11.5km, 15.5km and 26km) where the vertical profiles in (b), (c) and (d) are plotted. (d) Horizontal profiles of the azimuthally and time-averaged vertical fluxes of radial velocity (red line -  $\langle u'w' \rangle$ ) and tangential velocity (blue line -  $\langle v'w' \rangle$ ).

radial inflow towards the eye, peaking in outer the eyewall region, before decreasing towards the inner eyewall. The tangential velocity ( $\langle v \rangle$  – blue solid line) is maximum at the inner edge of the eyewall ( $r \approx 11\text{km}$ ), decreasing steadily away from the eye and sharply towards the eye. The vertical velocity ( $\langle w \rangle$  – black solid line) is seen to be near zero at this height, across all radii. For visibility,  $\langle w \rangle$  plotted in Fig. 4.3(a) is multiplied by a factor of 10.0 and is seen to only become slightly significant towards the inner edge of the eyewall (i.e.,  $r \approx 11\text{km}$ ). The analyses presented in this study focuses on understanding the near surface behaviour of coherent structures in regions of of HBL with notably different environmental conditions, partly to clarify how the kinematics of these structures may/may not vary across different flow regimes. Therefore three vertical profiles from the inner eyewall (Fig. 4.3(b)), outer eyewall (Fig. 4.3(c)) and inflowing BL (Fig. 4.3(d)) respectively are shown below. From these profiles, focussing on  $z \approx 63\text{m}$  – dashed black line, the only notable change in  $\langle v \rangle$  (solid blue line) between Figures 4.3(b)-(c)-(d) is the significant increase in its magnitude as the eye is approached, almost doubling in magnitude between Figures 4.3(d) and (b). The mean radial velocity –  $\langle u \rangle$  (solid red line) – follows a similar trend, except that its magnitude is seen to reduce as towards the inner eyewall (Fig. 4.3(b)) compared to the outer eyewall (Fig. 4.3(c)). Similarly, the vertical velocity –  $\langle w \rangle$  (solid black line) multiplied by a factor of 10 – remains negligible at  $\approx 63\text{m}$  in the inflowing BL (Fig. 4.3(d)), increasing slightly in the outer eyewall (Fig. 4.3(c)), until its peak as the inner edge of the eyewall is approached (Fig. 4.3(b)). In summary, the most significant changes in the mean velocity fields between the inflowing BL and the eyewall (inner and outer), appears to be a mere amplification of the radial and tangential velocity fields, with the mean vertical velocity being comparatively negligible. We note that at  $z \geq 750\text{m}$ , the difference between the profiles in Figs. 4.3(b)-(c)-(d) are more complicated than a mere increase: Specifically, in the inner eyewall,  $\langle u \rangle$  switches from inflow (negative) to outflow (positive) while  $\langle w \rangle$  becomes

non-negligible. We suspect that the findings detailed in the rest of this study (focused on the near surface region,  $z \approx 63\text{m}$ ) may therefore differ from greater heights where the mean conditions are much complicated. In this sense, the present study aims to provide a base understanding for future work.

Fig. 4.3(e) shows horizontal profiles of the azimuthally and time averaged vertical momentum fluxes (red line –  $\langle u'w' \rangle$ , blue line –  $\langle v'w' \rangle$ ). It is clear that: in most of the near surface HBL, the mean vertical momentum flux remains mostly negative from the inflowing BL to the inner eyewall. A comparison of the red and blue lines indicate that: in most of the inflowing BL, the vertical momentum flux of tangential velocity ( $\langle v'w' \rangle$ ) is comparatively larger than for the radial velocity ( $\langle u'w' \rangle$ ), which is near zero. As the outer eyewall is approached,  $\langle u'w' \rangle$  increases steadily until it becomes comparable to  $\langle v'w' \rangle$  in the inner eyewall. These profiles do not, however, offer up any information on the kinematics of the flow peculiar to extreme cases of instantaneous fluxes which have been averaged out to produce these profiles, nor a breakdown of the negative fluxes (i.e.,  $-u'w'$  and  $-v'w'$ ). To address clarify these further, we explore the quadrant distribution of the fluctuating velocity fields below.

#### 4.3.2 Quadrant analysis

Quadrant analysis, introduced first by [223] and employed extensively in turbulence research [193, 175, 174, 98, 161, 222, 109] is useful in addressing the issue above, in that the negative vertical momentum fluxes (i.e.,  $-\langle u'w' \rangle$  and  $-\langle v'w' \rangle$ ) can be further broken down into ejection/sweep pairs (i.e.,  $Q_2$ :  $[-u', +w']$ ,  $[-v', +w']$  and  $Q_4$ :  $[+u', -w']$ ,  $[+v', -w']$  respectively) in addition to the so called "outward" ( $Q_1$ :  $[+u', +w']$ ,  $[+v', +w']$ ) and "inward" ( $Q_3$ :  $[-u', -w']$ ,  $[-v', -w']$ ) interactions. In the context of the mean fields discussed in Figs. 4.3(a)-(d), an ejection of radial velocity fluctuation (i.e.,  $[-u', +w']$ ) implies stronger-than-average inward flowing air parcels are being tossed upwards by positive fluctuating vertical velocity, while sweep events

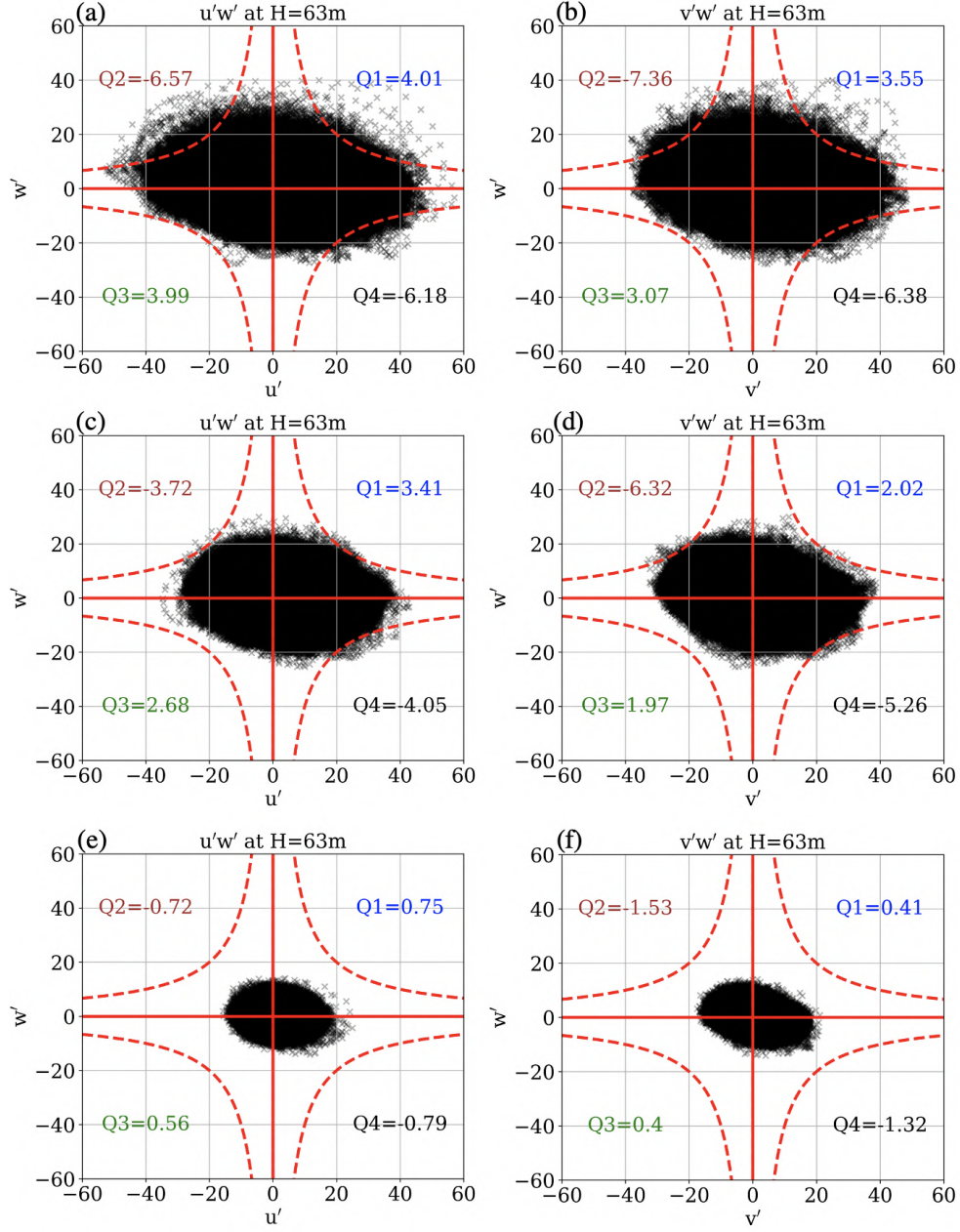


Figure 4.4. Quadrant distribution of fluctuating velocity components ( $u'$ ,  $v'$  and  $w'$ ) in the inner eyewall ( $r \approx 10 - 13\text{km}$  – (a),(b)), outer eyewall ( $r \approx 14 - 17\text{km}$  – (c),(d)) and inflowing boundary layer ( $r \approx 22 - 30\text{km}$  – (e),(f)), at 63m height above the surface. The red dashed curves in each panel represents arbitrary hyperbolic curves to visually identify extreme events. The blue, brown, green and black numbers in each quadrant denotes the mean flux components from the  $Q_1$ ,  $Q_2$ ,  $Q_3$  and  $Q_4$  quadrant respectively.

(i.e.,  $[+u', -w']$ ) indicate outflowing air aloft being pulled down to the surface by negative fluctuating vertical velocity. Similarly, an ejection (sweep) of tangential velocity fluctuations indicate low (high) momentum air being lofted (pulled) upwards (downwards). In this section we take the analysis presented in Fig. 4.3(e) a step further by investigating individual contributions of different quadrants to the mean vertical momentum flux. In all panels shown below (Fig. 4.4), the mean flux in each quadrant is noted in blue, brown, green and black, while the dashed red line is a hyperbolic function used to identify extreme instantaneous events.

Figures 4.4(a) and (b) show that the mean fluxes in the  $Q_2$  and  $Q_4$  quadrants dominate mean flux fields. A closer look at the scatter plot in both figures indicate that there are significant extreme  $Q_1$  events i.e.,  $[+u', +w']$  and  $[+v', +w']$  exceeding the dash red lines. This suggests that these few extreme cases, though visually noticeable, are still insufficient to account for a mean greater flux than seen for the  $Q_2/Q_4$  quadrants. Using the same hyperbolic function in Figures 4.4(c) and (d), it is seen that there are less extreme events exceeding the dashed red lines in the outer eyewall than in the inner eyewall (Figures 4.4(a) and (b)). In addition, we note that  $Q_2/Q_4$  quadrant events dominate the mean flux fields in the outer eyewall, similar to the inner eyewall. Similarly, in the inflowing BL, Figures 4.4(e) and (f) shows that there are comparatively much less extreme occurrences of extreme fluxes. In Fig. 4.4(e), the  $Q_2/Q_4$  quadrant pair dominate, however, we also note that the mean flux from  $Q_1$  events (top right quadrant in blue) slightly exceeds the ejection quadrant ( $Q_2$ ) event. In Fig. 4.4(f), the  $Q_2/Q_4$  events significantly dominate the mean flux contribution compared to other quadrants.

Results from the quadrant analyses above suggests that  $Q_2/Q_4$  events possess the dominant flux contributions. The question thus arises as to what the structure of turbulent eddies associated with these events look like? In the following subsections, we focus on extreme ejection events as a criteria for conditional averaging. By examining

the conditionally averaged perturbation fields around these events, the representative structure of the derived "conditional eddy" is examined. We then employ the well known Q-criteria [90, 94, 139] for the identification of vortices, to further investigate the three dimensional structure of the conditional eddy. The Q-criteria identifies a vortex core simply as regions where the second invariant of the velocity gradient tensor,

$$Q = (\|\mathbf{\Omega}\|^2 - \|\mathbf{S}\|^2) / 2$$

is positive, where  $\mathbf{\Omega}$  and  $\mathbf{S}$  are the rotation and strain rate respectively.

#### 4.3.3 The structure of educed conditional eddies

We begin our investigation of the structure of conditional eddies in the near-surface HBL by first examining the structure of coherent **ejection** events (i.e.,  $[-u', +w']$  and  $[-v', +w']$ ) in the inner eyewall ( $r \approx 10 - 13\text{km}$ ), outer eyewall ( $r \approx 14 - 17\text{km}$ ) and inflowing BL ( $r \approx 22 - 30\text{km}$ ). Using the conditional averaging scheme detailed in the previous section, we search for events in each of the 61 snapshots that satisfy the conditions:  $-u' + w'$ ,  $-v' + w'$  **and**  $\sqrt{(u'w')^2 + (v'w')^2} > 99.9\%$  i.e., ejection events (for radial and tangential velocity) whose mean vertical fluxes are in the top 99.9 percentile. 106, 99 and 271 events are identified in the inner eyewall, outer eyewall and inflowing BL respectively. These events are then averaged in each region. It should be noted that the resulting conditionally averaged fields are normalized by the local surface friction velocity ( $u^*$  in m/s). A similar procedure is carried out for sweep events (see appendix D) with 107, 122 and 379 extreme events identified in the inner eyewall, outer eyewall and inflowing BL respectively.

Figures 4.5(a)-(c) shows a horizontal section through the conditionally averaged structure in the inner eyewall, outer eyewall and inflowing BL respectively. We note that the overall shape (as indicated by the red contour – Q-criteria) of the conditional

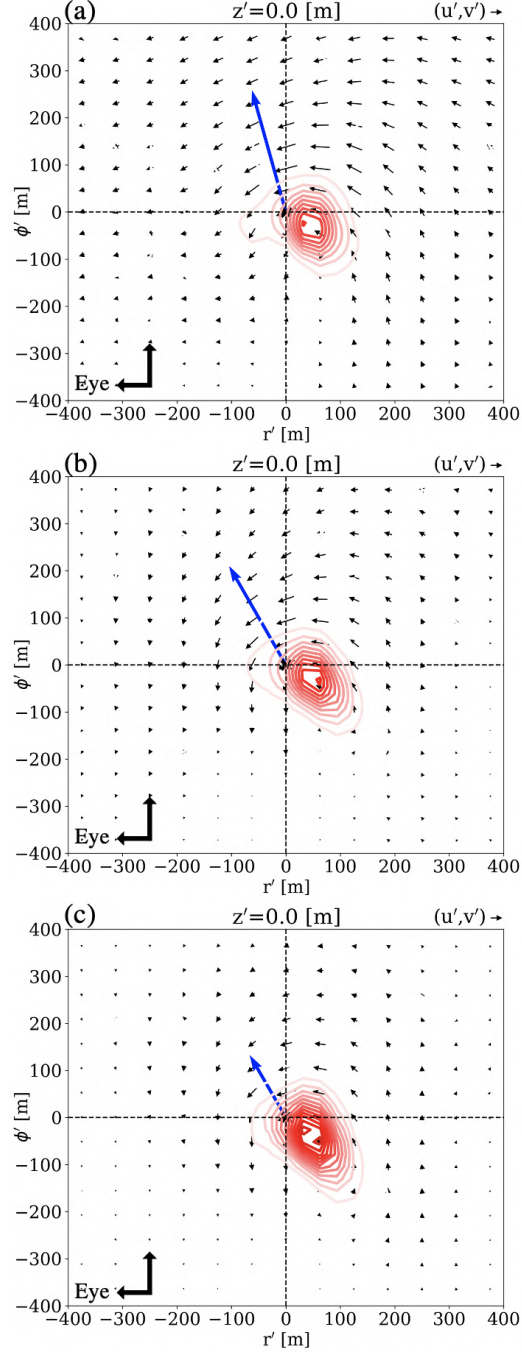


Figure 4.5. Horizontal sections through the center of the normalized conditionally-averaged structure (denoted by "x") in the (a) inner eyewall, (b) outer eyewall and (c) inflowing BL. The vectors  $[(u', v')]$ , at the top right corner of each panel, represents the normalized fluctuating velocity components (exaggerated by  $\times 7$  for visibility), while the red contours indicate the Q-criteria with  $[\text{min}, \text{max}, \text{interval}] = [-15, 15, 0.75]$ . The blue arrow in panel indicates the mean flow direction at the center of the averaging radii.

eddy in all three regions of the near-surface HBL are qualitatively similar (i.e., a vortex core inclined, in the direction of the tangential winds ( $\phi$ ), towards the TC eye), indicating that the general structure of the conditional eddy associated with extreme vertical momentum flux does not depend significantly on the near-surface location in the HBL. We note, however, that the circulation (black vectors) around the vortex core increases from the inflowing BL (Fig. 4.5(c)) to the inner eyewall (Fig. 4.5(a)). The solid blue arrow at the center of the horizontal cross sections (Fig. 4.5(a), (b), (c)) points in the direction of the mean flow, with an inflow angle of  $-15.59^\circ$ ,  $-29.85^\circ$  and  $-30.07^\circ$  respectively, while the length of the arrow indicates the mean velocity field. It is seen that the structures are roughly inclined with the mean flow. Seeing that the conditional eddies are qualitatively similar in all three regions analysed in this study, the rest of our discussion is focussed on the inner eyewall (Fig. 4.5(a)). A closer look at the wind vectors around the vortex core in Fig. 4.5(a) indicates that the characteristic conditional eddy associated with ejection events within the eyewall acts to "turn" the tangential flow ( $\phi'$  direction) of air parcels towards the TC eye ( $r'$  direction).

To further understand the kinematics of the flow around the structure in Fig. 4.5(a), vertical cross sections through the center of the structure ( $r' = 0$ ,  $\phi' = 0$ ) as well as downstream (in-front) and upstream (behind) the center are shown in Fig. 4.6(a)-(f). From Fig. 4.6(a), we note that the structure associated with the "overturning" of inflowing air upwards in the inner eyewall is a single vortex core. This overturning of the inflowing air upwards is seen to decrease downstream of the structure ( $\phi' = 103.5m$  – Fig. 4.6(c)), occurring at an elevated height. This indicates that the head of the structure might be slightly lifted downstream. On the other hand, a vertical cross section upstream of conditional eddy structure ( $\phi' = -103.5m$  – Fig. 4.6(e)) shows little overturning effect of the vortex core. A vertical cross section at  $r' = 0$  (Fig. 4.6(b)) indicates that air parcels flowing in the tangential

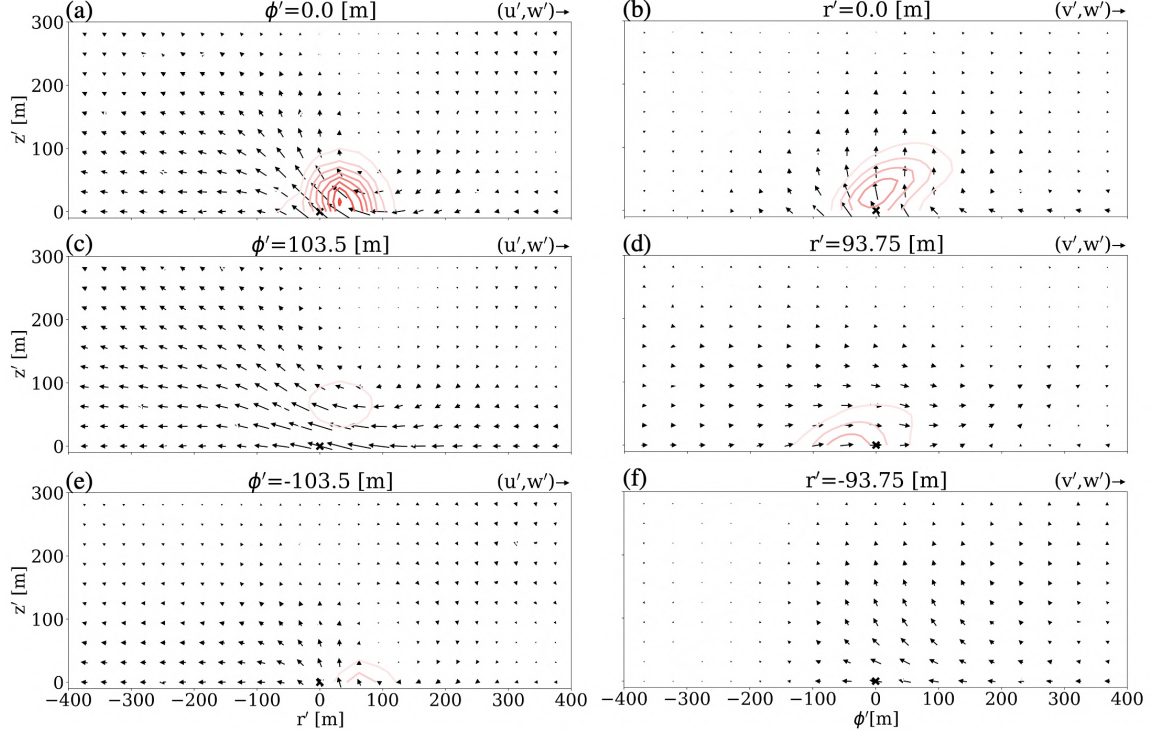


Figure 4.6. Transverse – [(b), (d), (f)] and longitudinal – [(c), (e), (g)] slices through the center of the normalized conditionally-averaged structure (denoted by "x") in the inner eyewall (Fig. 4.5(a) above). The vectors  $[(u', w'), (v', w')]$  respectively, at the top right corner of each panel, represents the normalized fluctuating velocity components (exaggerated by  $\times 7$  for visibility), while the red contours indicate the Q-criteria with  $[\text{min}, \text{max}, \text{interval}] = [-15, 15, 0.75]$ .

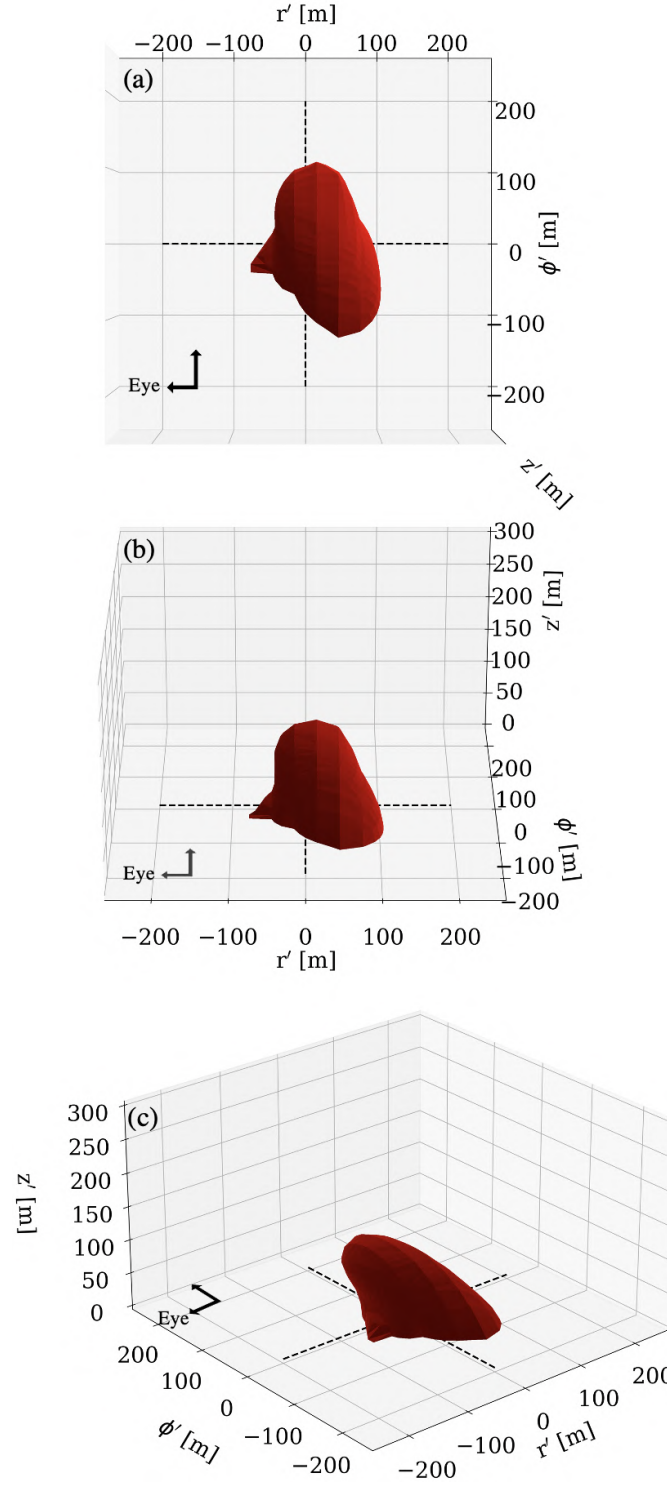


Figure 4.7. 3D isosurfaces of  $Q$ -criteria=1.0 in top view – (a) and side view – (b) for the conditionally averaged structure in the inner eyewall, shown in Fig. 4.5(a). The dashed black lines cut across the centroid of the structure.

direction ( $\phi'$ ) tend to be lifted around the the vortex core. There is notably less overturning vortex signature in this direction (i.e.,  $\phi'$  – Fig. 4.6(b)) compared to the cross section at  $r'$  (Fig. 4.6(a)). A comparison of the vector fields downstream ( $r' = -93.5m$  – Fig. 4.6(f)) and upstream ( $r' = 93.5m$  – Fig. 4.6(d)) shows opposing flow close to the conditional eddy, confirming a vertical vorticity component to the rotation seen in Fig. 4.5(a).

The foregoing discussion suggests the presence of a three dimensional vortex, lofting inflowing air upwards and circulating horizontal flow about it's core. In order to clarify the nature of this conditional eddy (shown in Figs. 4.5(a) and 4.6(a)-(f)), several views of the 3D isosurface of  $Q$ -criteria=1.0 is shown in Fig. 4.7. The plan view (Fig. 4.7(a)) of the conditionally averaged structure clearly confirms the horizontal inclination of the vortex core towards the TC eye, as seen in the two-dimensional horizontal slice (Fig. 4.5(a)). The oblique views in Figs. 4.7(b) and (c) confirms the vertical extent of the vortex core to be approximately 100m in height, confirming the two-dimensional cross section in Fig. 4.6(a). Most interestingly, Fig. 4.7(c) shows very clearly that the "head" of the coherent vortex core is lifted downstream, further clarifying the vertical cross sections in Figs. 4.6(a) and (c) where the "over turning" influence of the vortex core is lifted upwards downstream (i.e.,  $\phi' = 103.5m$ ). Overall, we find (from Figs. 4.5, 4.6 and Fig. 4.7) that the characteristic eddy associated with near-surface extreme vertical momentum fluxes (for ejection events) is a single vortex core, roughly horizontally inclined in the direction of the mean winds. We note that eddy conditioned on sweep events (see appendix D) exhibit an opposing flow (compared to ejections) around the structure. However, the conditional eddy appears less coherent that the  $Q$ -criteria signatures are weak.

#### 4.4 Discussion and Conclusions

In this study, output from a LES ( $\Delta x = \Delta y = 31.25\text{m}$ ,  $\Delta z = 15.625\text{m}$ ) of an idealized Category 5 TC is analyzed to investigate near-surface behaviour of coherent structures in the HBL and their relationship to extreme vertical momentum flux occurrences. In order to overcome the certain limitations of "bulk" approaches commonly used in the analysis of turbulent fluxes in the meteorology research community – e.g. the spatial and temporal averaging over the entire HBL as in [162] – conditional averaging was employed to educe the spatial structure of eddies associated with the most extreme flux occurrence. Using quadrant analysis, we confirm first the dominance of ejection/sweep events and then we conditionally average the spatial field around ejection events that are collocated with extreme vertical momentum fluxes. We find that the conditionally averaged structure exists as a vortex, roughly inclined with the mean winds. The structure associated with extreme sweep events appear to be comparatively less spatially coherent. The kinematics of the vortex core found in this study agrees with the mechanism (i.e., fluid acceleration) suggested by [15], [78] and [16] for the generation of extreme Reynolds stress events.

The coherent structure educed in this study differs from the "double-roller" signature found in LESs of atmospheric boundary layer flows [113, 65] and hairpin vortices in vegetation canopies [60, 109]. In their LES of a neutrally stratified PBL, [65] rotated both vertical momentum flux components (i.e.,  $v'w'$  and  $u'w'$ ) to be aligned. We choose, instead, to investigate the mean flux instead ( $\sqrt{(u'w')^2 + (v'w')^2}$ ) and believe that this subtle difference is not responsible for the difference in the structures found. We also explored (not shown in this study) structures conditioned on extreme vertical momentum fluxes alone and separately (i.e.,  $-v', +w' < 0$  and  $-u', +w' < 0$ ) and found a pair of counter-rotating legs of inclined vortices in the former and a single vortex core in the later. We insist that the interpretation of the vertical momentum flux of tangential velocity ( $-v', +w'$ ) separately from radial ve-

locity  $(-u', +w')$  is not justified seeing that some combination of both quantities (in our case  $-\sqrt{(-u', +w')^2 + (-v', +w')^2}$ ) defines the mean vertical momentum flux. Furthermore, we confirm the robustness of the structure deduced in this study by a series of sensitivity experiments varying the threshold for identifying extreme mean vertical momentum flux (i.e., the 99.9 percentile shown in this study).

Although this study focused on near-surface ejection events for the vertical momentum fluxes, we have shown key evidence on the a coherent vortex core being the characteristic eddy structure in the inner eyewall, outer eyewall in inflowing BL. From Figs. 4.3(a)-(d), we re-emphasize that the height of focus in the present study is the near-surface ( $h=63\text{m}$ ) slightly above the height of maximum radial inflow, where the mean vertical velocity is comparatively minimal and the radial variation in radial and tangential velocity is simpler. This is not the case at  $z \geq 750\text{m}$ . Future research efforts thus lie in the investigation of the kinematics of coherent structures associated with extreme vertical momentum fluxes far from the near-surface region of the HBL, possibly in the much more complicated inflow-outflow zone within the eyewall. More research effort could also be directed towards the investigation of near-surface coherent structures in intense TCs with moderate to strong vertical wind shear (unlike the present study with where the storm is symmetric).

#### 4.5 Acknowledgments

The authors would like to acknowledge useful personal correspondence with Dr. Richard Rotunno, Edward (Ned) Patton, Robert H. Shaw and John Finnigan. We also acknowledge ONR grants N00014-19-S-B001 to the University of Notre Dame and N00014-20-1-2071 to NCAR/UCAR for financial support under the Tropical Cyclone Rapid Intensification (TCRI) campaign. George Bryan and Peter P. Sullivan were also supported by the NSF under Cooperative Agreement No. 1852977. We also acknowledge high-performance computing support from Cheyenne (<https://www.cray.com/>):

[//www.doi.org/10.5065/D6RX99HX](http://www.doi.org/10.5065/D6RX99HX)) provided by NSF NCAR's Computational and Information Systems Laboratory.

Due to the large size (several tens of terabytes), the model simulation output used in this study is stored on NSF NCAR's campaign storage system, and is available upon request to Dr. George Bryan.

## CHAPTER 5

### DISSERTATION CONCLUSION

Future simulations of the climate (and more specifically their impact on extreme weather events) lie at the core of intergovernmental actions on climate change. One of the most costliest consequence of climate change is the predicted increase in the intensity of hurricanes/tropical cyclones [107, 14] and the associated storm surges in coastal communities. Yet, understanding the factors which lead to hurricane intensification remains a challenge in the broader context of weather forecasting, despite being a subject of research for decades.

Using a set of numerical experiments at convection permitting ( $\approx 2000\text{m}$ ) and turbulence resolving ( $\approx 30\text{m}$ ) resolutions, this dissertation presents novel findings on the role of mesoscale SST distribution on the onset of TC rapid intensification. In addition, this dissertation explores the frontier of turbulence in the TC environment, providing significant clarity on its role on the mean intensity of the storm as well as the kinematics of eddies in the TC boundary layer. The National Oceanic and Atmospheric Administration (NOAA) Hurricane Research Division (HRD) emphasizes the improvement of weather forecasts through continuous observations, data assimilation, modeling and predictive sciences. Results from this dissertation directly contributes towards this vision. Specifically, the quantitative description of the kinematics of turbulent structures in a Category 5 storm, discussed in this dissertation, will directly improve the representation of these structures in NOAA's Hurricane Analysis and Forecast System (HAFS). In turn, this is expected to improve the forecast of TC RI, thereby helping minimize the risks of TC-related disasters. Furthermore, results

from this dissertation could potentially complement future in-situ measurements of turbulence in TCs (i.e., aircraft [NOAA WP-3D] and uncrewed aerial systems [UAS]), supporting research efforts by NOAA-HRD.

The research findings from Chapter 2 of this dissertation introduced a novel methodology which combines spectral and structure function analyses to generate realistic realizations of multiscale anomalies characteristic of the SST conditions in which Hurricane Irma (2017) underwent rapid intensification (RI). We investigated the impact of the length scale of these SST anomalies and the role of translation speed on the variance in RI onset timing. Length-scale-induced convective asymmetries, in addition to the mean magnitude of SST anomalies beneath the storm eye, are shown to modulate the variance in RI onset timing. The size of the associated SST length scales relative to the storm size is critical to the magnitude of variance in RI onset timing, as smaller length scales are shown to lack the spatial extent required to induce preferential convective asymmetries. Storm translation speed is also shown to influence the variance in RI onset timing for larger length scale ensembles by altering the exposure time of the eye to these SST anomalies. We find that an interplay between SST-induced convective asymmetries, the magnitude of SST anomalies underneath the eye/eye-wall, and storm translation speed play crucial roles in modulating the variance in RI onset timing.

Chapter 3 of this dissertation uses a turbulence-resolving simulation of a Category 5 tropical cyclone to understand the role of turbulence in intense storms. Results show that turbulence clearly modulates storm structure and intensity. This study provides guidance for the values of turbulent quantities (which are usually parameterized in comparatively coarse operational TC forecast models) in scarcely observed regions of intense storms. Furthermore, a complete formulation of the effective eddy viscosities is proposed, incorporating contributions from typically ignored Reynolds normal stress terms.

In Chapter 4, this dissertation further explores the role of turbulence in a Category-5 TC, focussing on the kinematics of near-surface eddies associated with extremely high vertical momentum flux occurrence. By conditionally averaging instantaneous fields around extreme Reynolds stress events, the structure of near-surface eddies is deduced and shown to be a vortex inclined in the direction of the mean velocity fields in the HBL. The structure of this conditional eddy is further shown to vary minimally between the inflowing BL, outer eyewall and inner eyewall. The results from this chapter lays the foundation for future efforts in the understanding of coherent structures in TCs as well as the possible formulation of parameterization schemes that account for their existence in the HBL.

In summary, Chapters 2 – 4 of this dissertation addressed the different multi-scale mechanisms which affect the onset of TC rapid intensification, as well as the mean intensity. The novel methodology developed in Chapter 2 shows potential for application in the real time prediction of TC RI using satellite data. The revised formulation of effective eddy viscosity (including the Reynolds normal stress terms) proposed in Chapter 3 could potentially lead to a better understanding of turbulent quantities and their radial/vertical variation in the HBL. Finally, the finding in Chapter 4 sheds more light on the mechanism associated with intense fluxes in the HBL, with potential in informing future turbulence parameterizations in the HBL.

## APPENDIX A

### OCEAN OBSERVATION OF SST DURING HURRICANE IRMA’S (2017) PASSAGE

Temperature measurements from ALAMO floats beneath Hurricane Irma (2017) which were extensively analyzed in [188], are shown in Fig. A1a-d. Floats 9126 and 9134 are closest to the storm and located to the left and right respectively, while 9129 and 9143 are located farthest from the storm (see Fig. 2.2b). Regardless of our use of uncoupled simulations, Fig. A1a-d provides observational evidence of spatial and temporal variation in SST relative to the storm center, in addition to Fig. 2.2c. There is a clear deepening of the mixed layer depth (seen in floats 9134 between the 5th and 6th day) due to storm induced upwelling as a consequence of Irma’s passage.

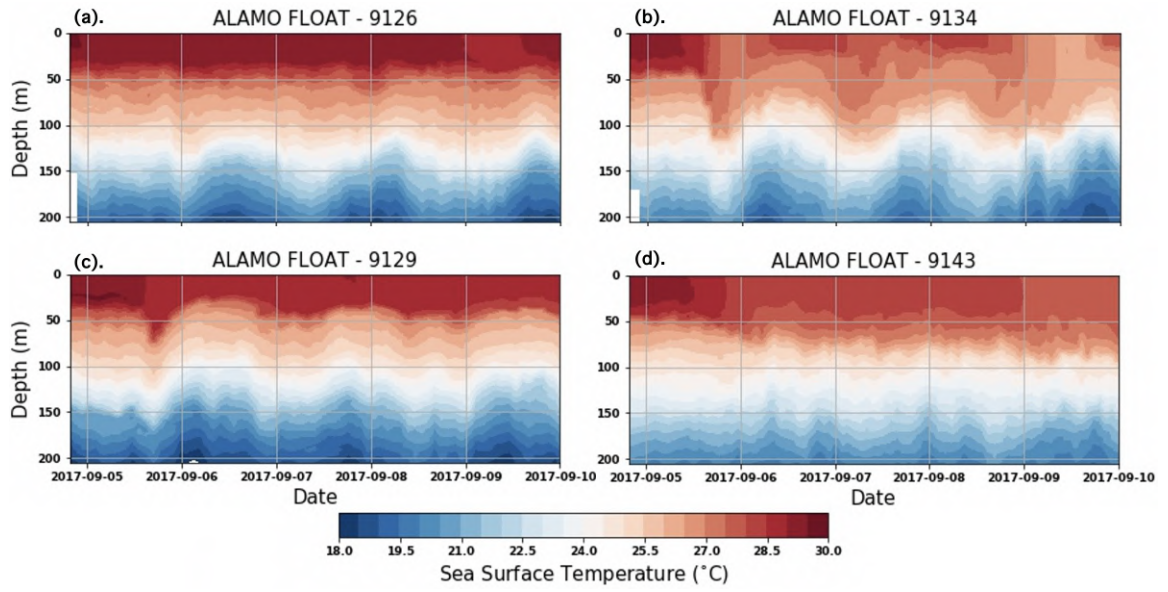


Figure A.1. Temporal variation of upper ocean temperature, measured from four selected ALAMO floats distributed across the path of Hurricane Irma (2017) as shown in Fig. 2.2b.

## APPENDIX B

### VARIOGRAM ESTIMATION AND ANISOTROPY

From the SST field provided in Fig. 2a, experimental variograms shown in figures B1 and B2 were computed using the Matheron estimator (Eqn. 6) implemented in the SciKit Gstat python [129]. For the omni directional variogram (ignoring anisotropic effects) shown in Fig. A1, 4000 random pairs of spatial locations, 45 bins of lag classes and a maximum lag of 280 grid points (i.e 560 km) were used.

Directional variograms (shown in Fig. B2) were also computed for the N-S and E-W direction using an azimuth of  $90^\circ$  and  $0^\circ$  respectively. The directional variograms were computed using similar parameters as the omnidirectional variogram, but for a 15 degree tolerance about the respective azimuth. From Fig. B2a, we see that the experimental variograms for both N-S/E-W directions track along each other up until a lag distance of about 230 grid points, suggesting that there is no preferred direction of spatial coherence up until that length scale. After this lag distance, the N-S directional variogram is seen to plateau, while the E-W directional variogram continues to increase. This indicates that up to a length scale of 230 grid points (560 km), there is no preferred direction of spatial continuity in the SST field, partially justifying our assumption of isotropy in the realizations of SST fields generated.

Figures B2b and c show the same directional experimental variograms in Fig. B2a, fitted with zero-nugget spherical variograms (shown by the green lines). From Fig. B2c, we see that the spherical theoretical variogram reasonably captures the behaviour of the experimental variogram, hence justifying our choice to generate random SST fields using the spherical variogram. We utilized the gstools python

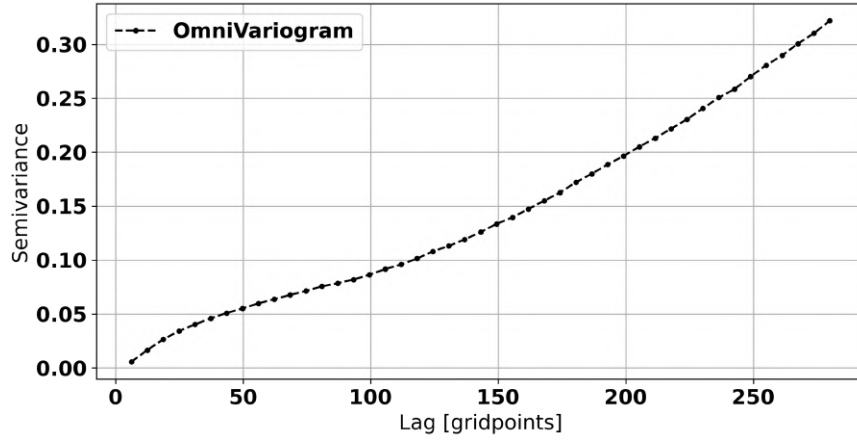


Figure B.1. Experimental omni-directional variogram (N-S and E-W direction) of the SST field traversed by Hurricane Irma (2017).

framework [153] for generating spatial random fields (SRF) using a well known spectral method known as the randomization approach, which we opted for due to its improved computational efficiency [81].

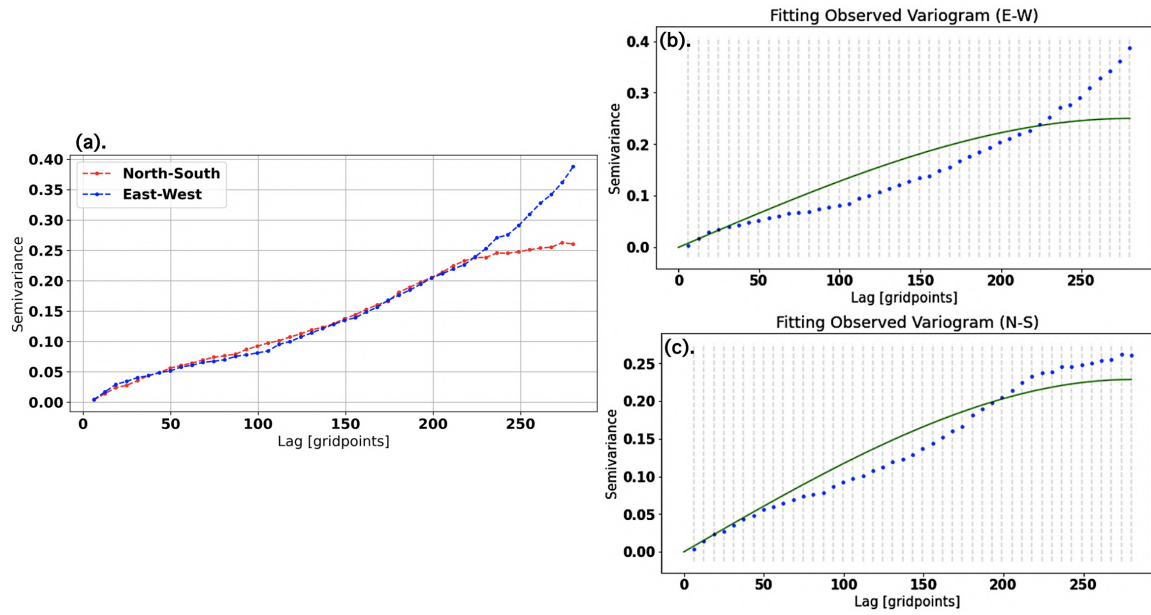


Figure B.2. (a) Experimental directional variogram (N-S and E-W direction) of the SST field traversed by Hurricane Irma (2017), (b) Experimental variogram for E-W direction fitted with spherical theoretical variogram, (c) Experimental variogram for N-S direction fitted with spherical theoretical variogram.

## APPENDIX C

### MEAN FIELD BUDGET ANALYSES

Figure C.1 shows the plot for other terms (mean advection terms, centripetal, pressure gradient and Coriolis force) in the azimuthally and time-averaged budget equations (3.1)-(3.2). For  $\langle v \rangle$ , the combined effect of the mean advection terms (first two rows) is to transport tangential velocity from the outer eyewall into the inner eyewall ( $V_{max}$ ) and aloft to the eyewall. Comparing this to the centripetal tendency directly below (third row), it is seen that the advective tendencies play an opposing role to the centripetal. For  $\langle u \rangle$ , it is seen that the combined effect of the mean advective tendencies (first two rows) is to transport the radial windspeed from outside the maximum inflow region ( $>15\text{km}$ ) towards the inner eyewall and aloft to the eyewall region. The combined centripetal and pressure gradient tendencies make nearly (but not exactly) compensating opposite contributions, with the net effect of positively contributing to the radial inflow in most regions slightly outside of the eyewall ( $r \geq 17\text{km}$ ) and also within the eyewall (but only beneath the height of maximum radial inflow). In both the  $\langle v \rangle$  and  $\langle u \rangle$  budgets, the azimuthally and time-averaged Coriolis tendencies contribute insignificantly to the mean budget equation.

For Fig. C.2, we see generally that the turbulent tendencies make a comparatively spatially smaller (but significant in magnitude) contribution to the mean budget equations (3.1)-(3.2). In both  $\langle v \rangle$  and  $\langle u \rangle$ , we note that the contributions from the vertical tendencies are comparatively more significant in magnitude, as opposed to radial tendencies. Furthermore, we note that the parameterized vertical tendencies for  $\langle v \rangle$  and  $\langle u \rangle$  are only significant at the lowest few model levels, with the standard

subgrid parameterization term being larger than the two-part term. In the rest of the boundary layer, the resolved turbulence dominates. Comparing Figs. C.1 and C.2, it is seen that the role of the turbulent eddies is most significant in the eyewall, corner-flow region and close to the surface.

Figure C.3 shows plots of the mean and turbulent eddy tendencies in the azimuthally and time-averaged budget for vertical velocity, (3.3). Overall the mean advective tendencies in the  $\langle w \rangle$  budget make small contributions. The vertical turbulent tendency in Fig. C.3 (third row – right) makes the largest turbulent contribution to the mean budget equation, opposing the sum of the buoyancy contribution and the vertical gradient of the normalized pressure term (third row – left).

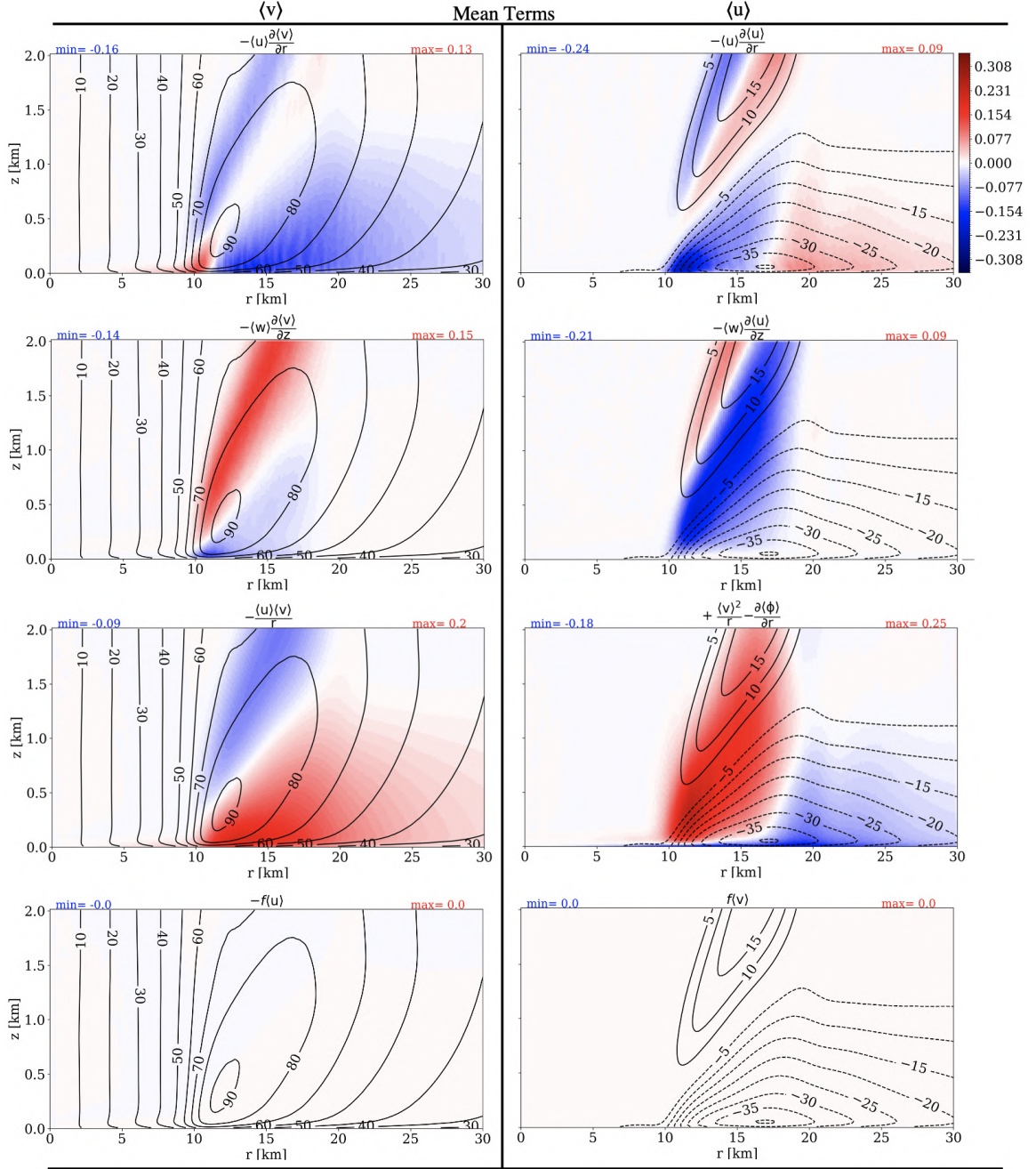


Figure C.1. As in Fig. 3.5 except showing the contribution from other mean-field terms in the budget equation shown in Eqs. (3.1) and (3.2), as indicated at the top of each panel.

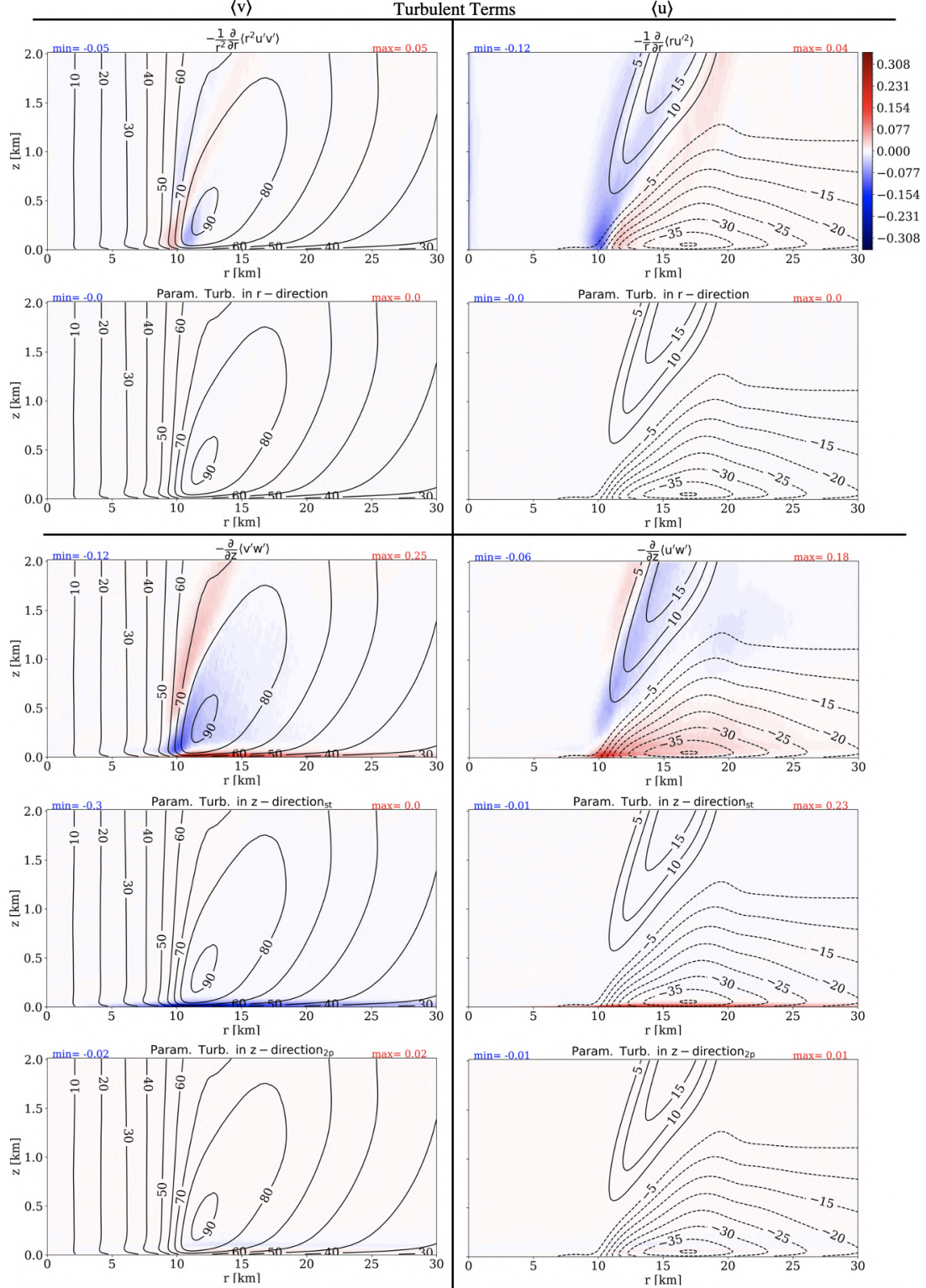


Figure C.2. As in Fig. 3.5 except showing terms related to the contribution of resolved and parameterized turbulence to the mean field budget, as indicated at the top of each panel.

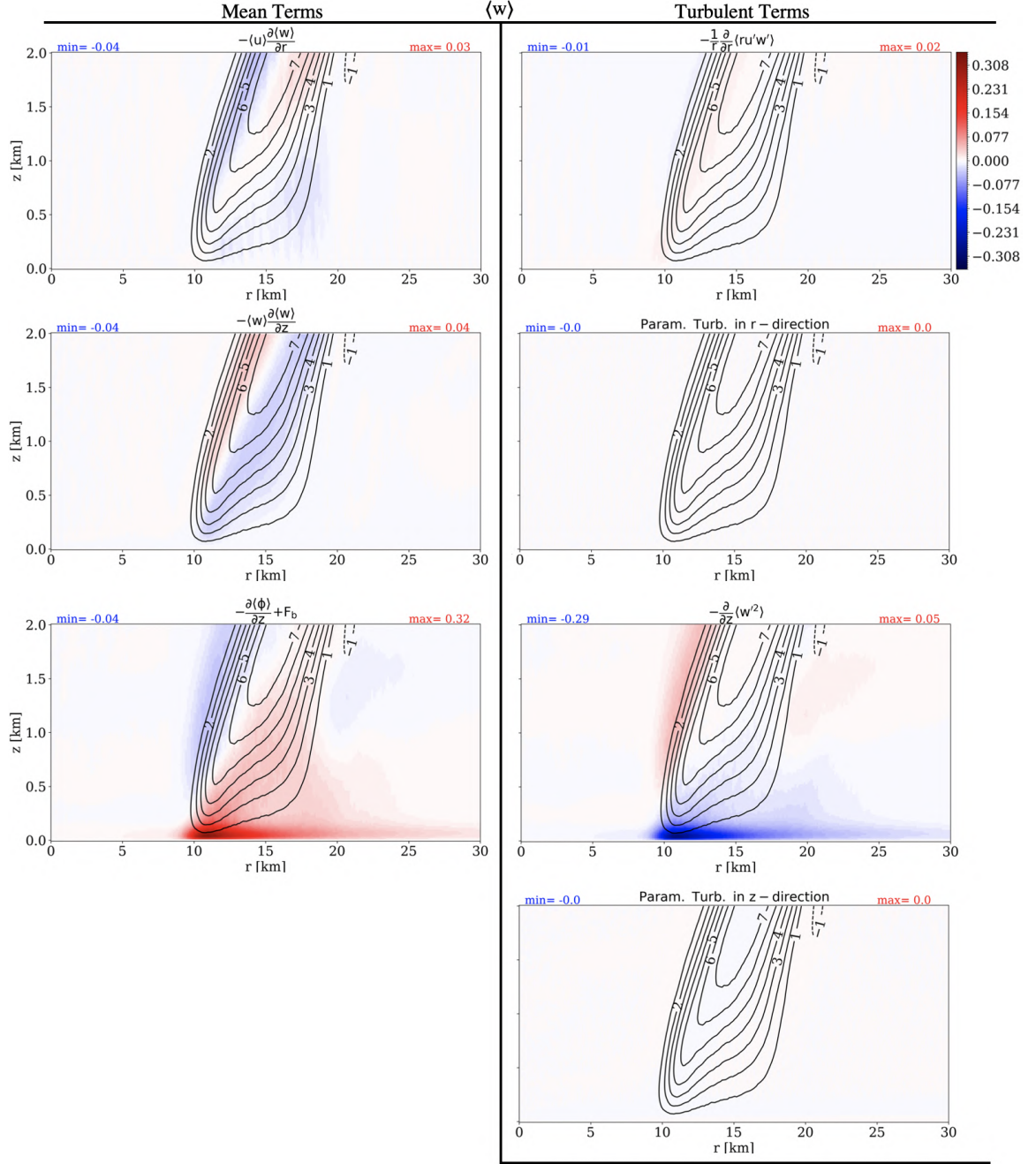


Figure C.3. As in Fig. 3.5(c)–(d) except showing the contribution from other mean-field and turbulent terms in the budget equation shown in Eq. (3.3), as indicated at the top of each panel.

## APPENDIX D

### STRUCTURE OF CONDITIONALLY AVERAGED SWEEP EVENTS

Figures D.1 shows horizontal (a) and vertical ((b)-(g)) cross sections through the "eddy" conditioned on the occurrence of extreme sweep ( $Q_4$ ) events, similar to Figs. 4.5(a) and Fig. 4.6(a)-(f) respectively. Fig D.1(a) shows that there is less rotation (as seen in the flow vectors) around the structure as flow moves away from the TC eye (compared to Fig. 4.5(a)). Vertical cross sections in the  $\phi'$  direction (Figs. D.1(b), (d) and (f)) shows flow vectors away from the TC eye (from  $-r'$  to  $+r'$ ) being pulled down around the center. Furthermore, vertical cross sections in the  $r'$  direction (Figs. D.1(c), (e) and (g)) shows the action of the coherent vortex in pulling down flow from  $-\phi'$  to  $+\phi'$ .

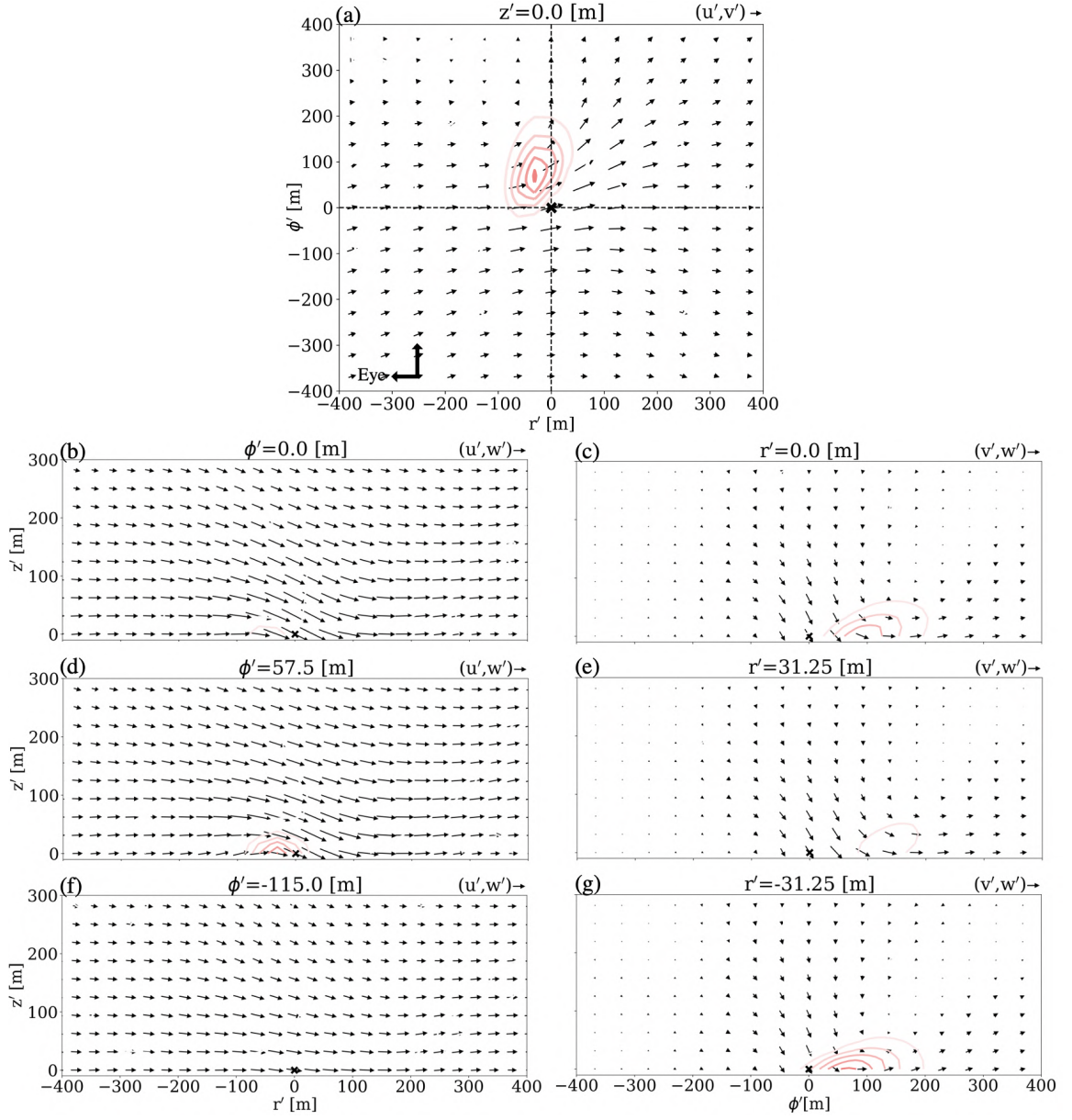


Figure D.1. Same as Fig. 4.5(a) and Fig. 4.6, but for sweep events i.e.,  $Q_4$ :  $[+u', -w']$ ,  $[+v', -w']$ .

## BIBLIOGRAPHY

1. S. D. Aberson, M. L. Black, R. A. Black, R. W. Burpee, J. J. Cione, C. W. Landsea, and F. D. Marks Jr. Thirty years of tropical cyclone research with the NOAA P-3 aircraft. *Bulletin of the American Meteorological Society*, 87(8): 1039–1056, 2006.
2. S. D. Aberson, M. T. Montgomery, M. Bell, and M. Black. Hurricane Isabel (2003): New insights into the physics of intense storms. Part II: Extreme localized wind. *Bulletin of the American Meteorological Society*, 87(10):1349–1354, 2006.
3. S. D. Aberson, J. A. Zhang, and K. N. Ocasio. An extreme event in the eyewall of Hurricane Felix on 2 September 2007. *Monthly Weather Review*, 145(6): 2083–2092, 2017.
4. R. J. Adrian. Stochastic estimation of the structure of turbulent fields. In *Eddy structure identification*, pages 145–195. Springer, 1996.
5. R. J. Adrian. Hairpin vortex organization in wall turbulence. *Physics of fluids*, 19(4), 2007.
6. K. Ahern, M. A. Bourassa, R. E. Hart, J. A. Zhang, and R. F. Rogers. Observed kinematic and thermodynamic structure in the hurricane boundary layer during intensity change. *Monthly Weather Review*, 147(8):2765–2785, 2019.
7. A. Aksoy, J. J. Cione, B. A. Dahl, and P. D. Reasor. Tropical cyclone data assimilation with Coyote uncrewed aircraft system observations, very frequent cycling, and a new online quality control technique. *Monthly Weather Review*, 150(4):797–820, 2022.
8. A. A. Alford, M. I. Biggerstaff, and G. Carrie. Using Ground-Based Radar Observations to Evaluate Asymmetric Convection and Eyewall Dynamics during the Landfall of Hurricane Harvey (2017). *Journal of the Atmospheric Sciences*, 80(7):1867–1889, 2023.
9. J. J. Alland, B. H. Tang, K. L. Corbosiero, and G. H. Bryan. Combined effects of midlevel dry air and vertical wind shear on tropical cyclone development. part ii: Radial ventilation. *Journal of the Atmospheric Sciences*, 78(3):783–796, 2021.

10. G. R. Alvey III, J. Zawislak, and E. Zipser. Precipitation properties observed during tropical cyclone intensity change. *Monthly Weather Review*, 143(11): 4476–4492, 2015.
11. T. S. Anandh, B. K. Das, J. Kuttippurath, and A. Chakraborty. A coupled model analyses on the interaction between oceanic eddies and tropical cyclones over the bay of bengal. *Ocean Dynamics*, 70(3):327–337, 2020.
12. R. A. Anthes. The dynamics and energetics of mature tropical cyclones. *Reviews of Geophysics*, 12(3):495–522, 1974.
13. B. N. Bailey and R. Stoll. Turbulence in sparse, organized vegetative canopies: a large-eddy simulation study. *Boundary-layer meteorology*, 147:369–400, 2013.
14. K. Balaguru, C.-C. Chang, L. R. Leung, G. R. Foltz, S. M. Hagos, M. F. Wehner, J. P. Kossin, M. Ting, and W. Xu. A global increase in nearshore tropical cyclone intensification. *Earth’s Future*, 12(5):e2023EF004230, 2024.
15. P. S. Bernard and R. A. Handler. Reynolds stress and the physics of turbulent momentum transport. *Journal of Fluid Mechanics*, 220:99–124, 1990.
16. P. S. Bernard, J. M. Thomas, and R. A. Handler. Vortex dynamics and the production of Reynolds stress. *Journal of Fluid Mechanics*, 253:385–419, 1993.
17. G. Biswas and V. Eswaran. *Turbulent flows: fundamentals, experiments and modeling*. CRC Press, 2002.
18. P. G. Black, E. A. D’Asaro, W. M. Drennan, J. R. French, P. P. Niiler, T. B. Sanford, E. J. Terrill, E. J. Walsh, and J. A. Zhang. Air–sea exchange in hurricanes: Synthesis of observations from the coupled boundary layer air–sea transfer experiment. *Bulletin of the American Meteorological Society*, 88(3): 357–374, 2007.
19. A. K. Blackadar. The vertical distribution of wind and turbulent exchange in a neutral atmosphere. *Journal of Geophysical Research*, 67(8):3095–3102, 1962.
20. H. B. Bluestein and F. D. Marks Jr. On the structure of the eyewall of Hurricane Diana (1984): Comparison of radar and visual characteristics. *Monthly Weather Review*, 115(10):2542–2552, 1987.
21. G. H. Bryan. Effects of surface exchange coefficients and turbulence length scales on the intensity and structure of numerically simulated hurricanes. *Monthly Weather Review*, 140(4):1125–1143, 2012.
22. G. H. Bryan and J. M. Fritsch. A benchmark simulation for moist nonhydrostatic numerical models. *Monthly Weather Review*, 130(12):2917–2928, 2002.
23. G. H. Bryan and R. Rotunno. The maximum intensity of tropical cyclones in axisymmetric numerical model simulations. *Monthly Weather Review*, 137(6): 1770–1789, 2009.

24. G. H. Bryan, N. A. Dahl, D. S. Nolan, and R. Rotunno. An eddy injection method for large-eddy simulations of tornado-like vortices. *Monthly Weather Review*, 145(5):1937–1961, 2017.
25. G. H. Bryan, R. P. Worsnop, J. K. Lundquist, and J. A. Zhang. A simple method for simulating wind profiles in the boundary layer of tropical cyclones. *Boundary-Layer Meteorology*, 162(3):475–502, 2017.
26. D. Byrne and J. A. Zhang. Height-dependent transition from 3-D to 2-D turbulence in the hurricane boundary layer. *Geophysical Research Letters*, 40(7):1439–1442, 2013.
27. J. P. Cangialosi, E. Blake, M. DeMaria, A. Penny, A. Latta, E. Rappaport, and V. Tallapragada. Recent progress in tropical cyclone intensity forecasting at the National Hurricane Center. *Weather and Forecasting*, 35(5):1913–1922, 2020.
28. C. A. Carrasco, C. W. Landsea, and Y.-L. Lin. The influence of tropical cyclone size on its intensification. *Weather and Forecasting*, 29(3):582–590, 2014.
29. R. Cécé, D. Bernard, Y. Krien, F. Leone, T. Candela, M. Péroche, E. Biabiany, G. Arnaud, A. Belmadani, P. Palany, et al. A 30 m scale modeling of extreme gusts during Hurricane Irma (2017) landfall on very small mountainous islands in the Lesser Antilles. *Natural Hazards and Earth System Sciences*, 21(1):129–145, 2021.
30. D. B. Chelton, M. G. Schlax, and R. M. Samelson. Global observations of nonlinear mesoscale eddies. *Progress in oceanography*, 91(2):167–216, 2011.
31. S. Chen, R. L. Elsberry, and P. A. Harr. Modeling interaction of a tropical cyclone with its cold wake. *Journal of the Atmospheric Sciences*, 74(12):3981–4001, 2017.
32. X. Chen. How Do Planetary Boundary Layer Schemes Perform in Hurricane Conditions: A Comparison With Large-Eddy Simulations. *Journal of Advances in Modeling Earth Systems*, 14(10):e2022MS003088, 2022.
33. X. Chen and F. D. Marks. Parameterizations of Boundary Layer Mass Fluxes in High-Wind Conditions for Tropical Cyclone Simulations. *Journal of the Atmospheric Sciences*, 81(1):77–91, 2024.
34. X. Chen, G. H. Bryan, J. A. Zhang, J. J. Cione, and F. D. Marks. A framework for simulating the tropical cyclone boundary layer using large-eddy simulation and its use in evaluating PBL parameterizations. *Journal of the Atmospheric Sciences*, 78(11):3559–3574, 2021.
35. Y.-H. Cheng, C.-R. Ho, Q. Zheng, and N.-J. Kuo. Statistical characteristics of mesoscale eddies in the north pacific derived from satellite altimetry. *Remote Sensing*, 6(6):5164–5183, 2014.

36. T. M. Chin, J. Vazquez-Cuervo, and E. M. Armstrong. A multi-scale high-resolution analysis of global sea surface temperature. *Remote sensing of environment*, 200:154–169, 2017.
37. J. J. Cione and E. W. Uhlhorn. Sea surface temperature variability in hurricanes: Implications with respect to intensity change. *Monthly Weather Review*, 131(8): 1783–1796, 2003.
38. J. J. Cione, E. Kalina, E. Uhlhorn, A. Farber, and B. Damiano. Coyote unmanned aircraft system observations in Hurricane Edouard (2014). *Earth and Space Science*, 3(9):370–380, 2016.
39. J. J. Cione, G. H. Bryan, R. Dobosy, J. A. Zhang, G. de Boer, A. Aksoy, J. B. Wadler, E. A. Kalina, B. A. Dahl, K. Ryan, et al. Eye of the storm: Observing hurricanes with a small unmanned aircraft system. *Bulletin of the American Meteorological Society*, 101(2):E186–E205, 2020.
40. I. Clark. *Practical geostatistics*, volume 3. Applied Science Publishers London, 1979.
41. C. Combot, A. Mouche, J. Knaff, Y. Zhao, Y. Zhao, L. Vinour, Y. Quilfen, and B. Chapron. Extensive high-resolution synthetic aperture radar (SAR) data analysis of tropical cyclones: Comparisons with SFMR flights and best track. *Monthly Weather Review*, 148(11):4545–4563, 2020.
42. N. Cressie. *Statistics for spatial data* wiley-interscience. 1993.
43. J. Darko, L. Folsom, H. Park, M. Minamide, M. Ono, and H. Su. A Sampling-Based Path Planning Algorithm for Improving Observations in Tropical Cyclones. *Earth and Space Science*, 9(1):e2020EA001498, 2022.
44. J. W. Deardorff. Stratocumulus-capped mixed layers derived from a three-dimensional model. *Boundary-Layer Meteorology*, 18(4):495–527, 1980.
45. M. DeMaria and J. Kaplan. A statistical hurricane intensity prediction scheme (ships) for the atlantic basin. *Weather and Forecasting*, 9(2):209–220, 1994.
46. M. DeMaria and J. Kaplan. An updated statistical hurricane intensity prediction scheme (ships) for the atlantic and eastern north pacific basins. *Weather and Forecasting*, 14(3):326–337, 1999.
47. M. DeMaria, C. R. Sampson, J. A. Knaff, and K. D. Musgrave. Is tropical cyclone intensity guidance improving? *Bulletin of the American Meteorological Society*, 95(3):387–398, 2014.
48. S. C. Doney, D. M. Glover, S. J. McCue, and M. Fuentes. Mesoscale variability of sea-viewing wide field-of-view sensor (seawifs) satellite ocean color: Global patterns and spatial scales. *Journal of Geophysical Research: Oceans*, 108(C2), 2003.

49. S. Dong, A. Lozano-Durán, A. Sekimoto, and J. Jiménez. Coherent structures in statistically stationary homogeneous shear turbulence. *Journal of Fluid Mechanics*, 816:167–208, 2017.
50. S. Dong, Y. Huang, X. Yuan, and A. Lozano-Durán. The coherent structure of the kinetic energy transfer in shear turbulence. *Journal of Fluid Mechanics*, 892:A22, 2020.
51. W. M. Drennan, J. A. Zhang, J. R. French, C. McCormick, and P. G. Black. Turbulent fluxes in the hurricane boundary layer. Part II: Latent heat flux. *Journal of the Atmospheric Sciences*, 64(4):1103–1115, 2007.
52. A. Eliassen. On the formation of fronts in the atmosphere. *The Atmosphere and the Sea in Motion (Rossby Memorial Volume)*, pages 277–287, 1959.
53. K. Emanuel. Will global warming make hurricane forecasting more difficult? *Bulletin of the American Meteorological Society*, 98(3):495–501, 2017.
54. K. Emanuel, C. DesAutels, C. Holloway, and R. Korty. Environmental control of tropical cyclone intensity. *Journal of the atmospheric sciences*, 61(7):843–858, 2004.
55. K. A. Emanuel. An air-sea interaction theory for tropical cyclones. Part I: Steady-state maintenance. *Journal of Atmospheric Sciences*, 43(6):585–605, 1986.
56. K. A. Emanuel. The maximum intensity of hurricanes. *Journal of the Atmospheric Sciences*, 45(7):1143–1155, 1988.
57. K. A. Emanuel. Sensitivity of tropical cyclones to surface exchange coefficients and a revised steady-state model incorporating eye dynamics. *Journal of Atmospheric Sciences*, 52(22):3969–3976, 1995.
58. K. A. Emanuel. Some aspects of hurricane inner-core dynamics and energetics. *Journal of the Atmospheric Sciences*, 54(8):1014–1026, 1997.
59. M. P. Encinar and J. Jiménez. Momentum transfer by linearised eddies in turbulent channel flows. *Journal of Fluid Mechanics*, 895:A23, 2020.
60. J. J. Finnigan, R. H. Shaw, and E. G. Patton. Turbulence structure above a vegetation canopy. *Journal of Fluid Mechanics*, 637:387–424, 2009.
61. P. M. Finocchio, S. J. Majumdar, D. S. Nolan, and M. Iskandarani. Idealized tropical cyclone responses to the height and depth of environmental vertical wind shear. *Monthly Weather Review*, 144(6):2155–2175, 2016.
62. L. Fitzmaurice, R. H. Shaw, K. T. Paw U, and E. G. Patton. Three-dimensional scalar microfront systems in a large-eddy simulation of vegetation canopy flow. *Boundary-layer meteorology*, 112(1):107–127, 2004.

63. R. Foster. Signature of large aspect ratio roll vortices in synthetic aperture radar images of tropical cyclones. *Oceanography*, 26(2):58–67, 2013.
64. R. C. Foster. Why rolls are prevalent in the hurricane boundary layer. *Journal of the Atmospheric Sciences*, 62(8):2647–2661, 2005.
65. R. C. Foster, F. Vianey, P. Drobinski, and P. Carlotti. Near-surface coherent structures and the vertical momentum flux in a large-eddy simulation of the neutrally-stratified boundary layer. *Boundary-layer meteorology*, 120:229–255, 2006.
66. J. R. French, W. M. Drennan, J. A. Zhang, and P. G. Black. Turbulent fluxes in the hurricane boundary layer. Part I: Momentum flux. *Journal of the Atmospheric Sciences*, 64(4):1089–1102, 2007.
67. K. Gao and I. Ginis. On the generation of roll vortices due to the inflection point instability of the hurricane boundary layer flow. *Journal of the Atmospheric Sciences*, 71(11):4292–4307, 2014.
68. K. Gao and I. Ginis. On the equilibrium-state roll vortices and their effects in the hurricane boundary layer. *Journal of the Atmospheric Sciences*, 73(3):1205–1222, 2016.
69. K. Gao and I. Ginis. On the characteristics of linear-phase roll vortices under a moving hurricane boundary layer. *Journal of the Atmospheric Sciences*, 75(8):2589–2598, 2018.
70. K. Gao, I. Ginis, J. D. Doyle, and Y. Jin. Effect of boundary layer roll vortices on the development of an axisymmetric tropical cyclone. *Journal of the Atmospheric Sciences*, 74(9):2737–2759, 2017.
71. J. L. García-Franco, O. Gómez-Ramos, and C. Domínguez. Hurricane Otis: the costliest and strongest hurricane at landfall on record in Mexico. *Weather*, 79(6):182–184, 2024.
72. W. M. Gray. On the scales of motion and internal stress characteristics of the hurricane. *Journal of Atmospheric Sciences*, 23(3):278–288, 1966.
73. B. Guerrero, M. F. Lambert, and R. C. Chin. Extreme wall shear stress events in turbulent pipe flows: Spatial characteristics of coherent motions. *Journal of Fluid Mechanics*, 904:A18, 2020.
74. S. R. Guimond, G. M. Heymsfield, P. D. Reasor, and A. C. Didlake Jr. The rapid intensification of Hurricane Karl (2010): New remote sensing observations of convective bursts from the Global Hawk platform. *Journal of the Atmospheric Sciences*, 73(9):3617–3639, 2016.

75. S. R. Guimond, J. A. Zhang, J. W. Sapp, and S. J. Frasier. Coherent turbulence in the boundary layer of Hurricane Rita (2005) during an eyewall replacement cycle. *Journal of the Atmospheric Sciences*, 75(9):3071–3093, 2018.
76. K. Haakman, J.-M. Sayol, C. G. van der Boog, and C. A. Katsman. Statistical characterization of the observed cold wake induced by north atlantic hurricanes. *Remote Sensing*, 11(20):2368, 2019.
77. J. Han and C. S. Bretherton. TKE-based moist eddy-diffusivity mass-flux (EDMF) parameterization for vertical turbulent mixing. *Weather and Forecasting*, 34(4):869–886, 2019.
78. R. A. Handler, P. S. Bernard, A. L. Rovelstad, and J. D. Swearingen. On the role of accelerating fluid particles in the generation of Reynolds stress. *Physics of Fluids A: Fluid Dynamics*, 4(6):1317–1319, 1992.
79. C. Härtel, L. Kleiser, F. Unger, and R. Friedrich. Subgrid-scale energy transfer in the near-wall region of turbulent flows. *Physics of Fluids*, 6(9):3130–3143, 1994.
80. B. L. Hemingway, A. E. Frazier, B. R. Elbing, and J. D. Jacob. High-resolution estimation and spatial interpolation of temperature structure in the atmospheric boundary layer using a small unmanned aircraft system. *Boundary-Layer Meteorology*, 175(3):397–416, 2020.
81. F. Heße, V. Prykhodko, S. Schlüter, and S. Attinger. Generating random fields with a truncated power-law variogram: A comparison of several numerical methods. *Environmental modelling & software*, 55:32–48, 2014.
82. J. Hinze. Turbulence McGraw-Hill. *New York*, 421(3), 1959.
83. J. Hinze. Memory effects in turbulence. *Zeitschrift Angewandte Mathematik und Mechanik*, 56:403, 1976.
84. G. J. Holland. The maximum potential intensity of tropical cyclones. *Journal of the Atmospheric Sciences*, 54(21):2519–2541, 1997.
85. G. J. Holland and R. T. Merrill. On the dynamics of tropical cyclone structural changes. *Quarterly Journal of the Royal Meteorological Society*, 110(465):723–745, 1984.
86. P. Holmes. *Turbulence, coherent structures, dynamical systems and symmetry*. Cambridge university press, 2012.
87. J. Hong, J. Katz, C. Meneveau, and M. P. Schultz. Coherent structures and associated subgrid-scale energy transfer in a rough-wall turbulent channel flow. *Journal of Fluid Mechanics*, 712:92–128, 2012.

88. J. Horstmann, S. Falchetti, C. Wackerman, S. Maresca, M. J. Caruso, and H. C. Graber. Tropical cyclone winds retrieved from C-band cross-polarized synthetic aperture radar. *IEEE Transactions on Geoscience and Remote Sensing*, 53(5): 2887–2898, 2015.
89. L. Huang, X. Li, B. Liu, J. A. Zhang, D. Shen, Z. Zhang, and W. Yu. Tropical cyclone boundary layer rolls in synthetic aperture radar imagery. *Journal of Geophysical Research: Oceans*, 123(4):2981–2996, 2018.
90. J. C. Hunt, A. A. Wray, and P. Moin. Eddies, streams, and convergence zones in turbulent flows. *Studying turbulence using numerical simulation databases, 2. Proceedings of the 1988 summer program*, 1988.
91. A. F. Hussain. Role of coherent structures in turbulent shear flows. *Proceedings of the Indian Academy of Sciences Section C: Engineering Sciences*, 4:129–175, 1981.
92. J. Ito, T. Oizumi, and H. Niino. Near-surface coherent structures explored by large eddy simulation of entire tropical cyclones. *Scientific Reports*, 7(1):1–10, 2017.
93. B. Jaimes de la Cruz, L. K. Shay, J. B. Wadler, and J. E. Rudzin. On the hyperbolicity of the bulk air–sea heat flux functions: insights into the efficiency of air–sea moisture disequilibrium for tropical cyclone intensification. *Monthly weather review*, 149(5):1517–1534, 2021.
94. J. Jeong and F. Hussain. On the identification of a vortex. *Journal of fluid mechanics*, 285:69–94, 1995.
95. A. Journel. Ch... j. huijbregts,” mining geostatistics, 1978.
96. S. Kanada, S. Tsujino, H. Aiki, M. K. Yoshioka, Y. Miyazawa, K. Tsuboki, and I. Takayabu. Impacts of sst patterns on rapid intensification of typhoon megi (2010). *Journal of Geophysical Research: Atmospheres*, 122(24):13–245, 2017.
97. K. B. Karnauskas, L. Zhang, and K. A. Emanuel. The feedback of cold wakes on tropical cyclones. *Geophysical Research Letters*, 48(7):e2020GL091676, 2021.
98. G. Katul, C.-I. Hsieh, G. Kuhn, D. Ellsworth, and D. Nie. Turbulent eddy motion at the forest-atmosphere interface. *Journal of Geophysical Research: Atmospheres*, 102(D12):13409–13421, 1997.
99. J. Kepert and Y. Wang. The dynamics of boundary layer jets within the tropical cyclone core. Part II: Nonlinear enhancement. *Journal of the Atmospheric Sciences*, 58(17):2485–2501, 2001.
100. J. D. Kepert. Choosing a boundary layer parameterization for tropical cyclone modeling. *Monthly Weather Review*, 140(5):1427–1445, 2012.

101. J. Kim and P. Moin. The structure of the vorticity field in turbulent channel flow. Part 2. Study of ensemble-averaged fields. *Journal of Fluid Mechanics*, 162:339–363, 1986.
102. S. J. Kline, W. C. Reynolds, F. A. Schraub, and P. W. Runstadler. The structure of turbulent boundary layers. *Journal of Fluid Mechanics*, 30(4):741–773, 1967.
103. K. A. Kosiba and J. Wurman. Finescale dual-Doppler analysis of hurricane boundary layer structures in Hurricane Frances (2004) at landfall. *Monthly Weather Review*, 142(5):1874–1891, 2014.
104. J. P. Kossin. A global slowdown of tropical-cyclone translation speed. *Nature*, 558(7708):104–107, 2018.
105. J. P. Kossin and W. H. Schubert. Mesovortices in hurricane Isabel. *Bulletin of the American Meteorological Society*, 85(2):151–153, 2004.
106. J. P. Kossin, B. D. McNoldy, and W. H. Schubert. Vortical swirls in hurricane eye clouds. *Monthly Weather Review*, 130(12):3144–3149, 2002.
107. J. P. Kossin, K. R. Knapp, T. L. Olander, and C. S. Velden. Global increase in major tropical cyclone exceedance probability over the past four decades. *Proceedings of the National Academy of Sciences*, 117(22):11975–11980, 2020.
108. M. Le Hénaff, R. Domingues, G. Halliwell, J. A. Zhang, H.-S. Kim, M. Aristizabal, T. Miles, S. Glenn, and G. Goni. The role of the gulf of mexico ocean conditions in the intensification of hurricane michael (2018). *Journal of Geophysical Research: Oceans*, 126(5):e2020JC016969, 2021.
109. W. Li and M. G. Giometto. The structure of turbulence in unsteady flow over urban canopies. *Journal of Fluid Mechanics*, 985:A5, 2024.
110. X. Li and Z. Pu. Dynamic Mechanisms Associated with the Structure and Evolution of Roll Vortices and Coherent Turbulence in the Hurricane Boundary Layer: A Large Eddy Simulation During the Landfall of Hurricane Harvey. *Boundary-Layer Meteorology*, 186(3):615–636, 2023.
111. X. Li, J. A. Zhang, X. Yang, W. G. Pichel, M. DeMaria, D. Long, and Z. Li. Tropical cyclone morphology from spaceborne synthetic aperture radar. *Bulletin of the American Meteorological Society*, 94(2):215–230, 2013.
112. X. Li, Z. Pu, and Z. Gao. Effects of roll vortices on the evolution of Hurricane Harvey during landfall. *Journal of the Atmospheric Sciences*, 78(6):1847–1867, 2021.
113. C.-L. Lin, J. C. McWilliams, C.-H. Moeng, and P. P. Sullivan. Coherent structures and dynamics in a neutrally stratified planetary boundary layer flow. *Physics of Fluids*, 8(10):2626–2639, 1996.

114. I. Lin, C.-C. Wu, K. A. Emanuel, I.-H. Lee, C.-R. Wu, and I.-F. Pun. The interaction of supertyphoon maemi (2003) with a warm ocean eddy. *Monthly Weather Review*, 133(9):2635–2649, 2005.
115. I. Lin, I.-F. Pun, and C.-C. Wu. Upper-ocean thermal structure and the western north pacific category 5 typhoons. part ii: Dependence on translation speed. *Monthly Weather Review*, 137(11):3744–3757, 2009.
116. I. Lin, M.-D. Chou, and C.-C. Wu. The impact of a warm ocean eddy on typhoon morakot (2009): A preliminary study from satellite observations and numerical modelling. *TAO: Terrestrial, Atmospheric and Oceanic Sciences*, 22(6):6, 2011.
117. I.-I. Lin, C.-H. Chen, I.-F. Pun, W. T. Liu, and C.-C. Wu. Warm ocean anomaly, air sea fluxes, and the rapid intensification of tropical cyclone nargis (2008). *Geophysical Research Letters*, 36(3), 2009.
118. Q. Liu, L. Wu, N. Qin, J. Song, and N. Wei. Wind Gusts Associated with Tornado-Scale Vortices in the Tropical Cyclone Boundary Layer: A Numerical Simulation. *Frontiers in Earth Science*, 10:945058, 2022.
119. Y. Liu, C. Dong, Y. Guan, D. Chen, J. McWilliams, and F. Nencioli. Eddy analysis in the subtropical zonal band of the north pacific ocean. *Deep Sea Research Part I: Oceanographic Research Papers*, 68:54–67, 2012.
120. Y. Liu, H. LÜ, H. Zhang, Y. Cui, and X. Xing. Effects of ocean eddies on the tropical storm roanu intensity in the bay of bengal. *Plos one*, 16(3):e0247521, 2021.
121. S. Lorsolo, J. L. Schroeder, P. Dodge, and F. Marks. An observational study of hurricane boundary layer small-scale coherent structures. *Monthly Weather Review*, 136(8):2871–2893, 2008.
122. S. Lorsolo, J. A. Zhang, F. Marks, and J. Gamache. Estimation and mapping of hurricane turbulent energy using airborne Doppler measurements. *Monthly Weather Review*, 138(9):3656–3670, 2010.
123. J.-F. Louis. A parametric model of vertical eddy fluxes in the atmosphere. *Boundary-Layer Meteorology*, 17(2):187–202, 1979.
124. J. F. Louis. A short history of the operational PBL parameterization at ECMWF. In *Workshop on Planetary Boundary Layer Parameterization, ECMWF, England, 1982*, 1982.
125. A. Lozano-Durán, O. Flores, and J. Jiménez. The three-dimensional structure of momentum transfer in turbulent channels. *Journal of Fluid Mechanics*, 694: 100–130, 2012.

126. A. Lozano-Durán, M. G. Giometto, G. I. Park, and P. Moin. Non-equilibrium three-dimensional boundary layers at moderate Reynolds numbers. *Journal of Fluid Mechanics*, 883:A20, 2020.
127. Z. Ma, J. Fei, L. Liu, X. Huang, and Y. Li. An investigation of the influences of mesoscale ocean eddies on tropical cyclone intensities. *Monthly Weather Review*, 145(4):1181–1201, 2017.
128. H. Maeyama and S. Kawai. Near-wall numerical coherent structures and turbulence generation in wall-modelled large-eddy simulation. *Journal of Fluid Mechanics*, 969:A29, 2023.
129. M. Mälicke. Scikit-gstat 1.0: a scipy-flavored geostatistical variogram estimation toolbox written in python. *Geoscientific Model Development*, 15(6):2505–2532, 2022.
130. J. S. Malkus and H. Riehl. On the dynamics and energy transformations in steady-state hurricanes. *Tellus*, 12(1):1–20, 1960.
131. F. D. Marks and R. A. Houze. Inner core structure of Hurricane Alicia from airborne Doppler radar observations. *Journal of the Atmospheric Sciences*, 44(9):1296–1317, 1987.
132. F. D. Marks, P. G. Black, M. T. Montgomery, and R. W. Burpee. Structure of the eye and eyewall of Hurricane Hugo (1989). *Monthly Weather Review*, 136(4):1237–1259, 2008.
133. J. Martinez, C. A. Davis, and M. M. Bell. Eyewall asymmetries and their contributions to the intensification of an idealized tropical cyclone translating in uniform flow. *Journal of the Atmospheric Sciences*, 2022.
134. P. Mason and R. Sykes. A two-dimensional numerical study of horizontal roll vortices in an inversion capped planetary boundary layer. *Quarterly Journal of the Royal Meteorological Society*, 108(458):801–823, 1982.
135. P. J. Mason and D. J. Thomson. Stochastic backscatter in large-eddy simulations of boundary layers. *Journal of Fluid Mechanics*, 242:51–78, 1992.
136. J. M. Masters. Hunting Hugo: Ten years ago, the hurricane hunters had one of their wildest rides ever. *Weatherwise*, 52(5):20–27, 1999.
137. G. Matheron. *The regionalized variables and their estimation: an application of the theory of random functions to the natural sciences*, volume 4597. Masson and CIE, 1965.
138. W. Mei, C. Pasquero, and F. Primeau. The effect of translation speed upon the intensity of tropical cyclones over the tropical ocean. *Geophysical Research Letters*, 39(7), 2012.

139. K. Menon and R. Mittal. Significance of the strain-dominated region around a vortex on induced aerodynamic loads. *Journal of Fluid Mechanics*, 918:R3, 2021.
140. J. Ming, J. A. Zhang, and R. F. Rogers. Typhoon kinematic and thermodynamic boundary layer structure from dropsonde composites. *Journal of Geophysical Research: Atmospheres*, 120(8):3158–3172, 2015.
141. C.-H. Moeng and P. P. Sullivan. Large-eddy simulation. *Encyclopedia of Atmospheric Sciences*, 2:232–240, 2015.
142. P. Moin and J. Kim. Numerical investigation of turbulent channel flow. *Journal of fluid mechanics*, 118:341–377, 1982.
143. P. Moin and J. Kim. The structure of the vorticity field in turbulent channel flow. Part 1. Analysis of instantaneous fields and statistical correlations. *Journal of Fluid Mechanics*, 155:441–464, 1985.
144. J. D. Möller and L. J. Shapiro. Influences of asymmetric heating on hurricane evolution in the mm5. *Journal of the atmospheric sciences*, 62(11):3974–3992, 2005.
145. M. T. Montgomery and R. K. Smith. Paradigms for tropical cyclone intensification. *Australian Meteorological and Oceanographic Journal*, 64(1):37–66, 2014.
146. M. T. Montgomery and R. K. Smith. Recent developments in the fluid dynamics of tropical cyclones. *Annual Review of Fluid Mechanics*, 49:541–574, 2017.
147. M. T. Montgomery, M. M. Bell, S. D. Aberson, and M. L. Black. Hurricane Isabel (2003): New insights into the physics of intense storms. Part I: Mean vortex structure and maximum intensity estimates. *Bulletin of the American Meteorological Society*, 87(10):1335–1348, 2006.
148. H. Morrison, J. Curry, and V. Khvorostyanov. A new double-moment microphysics parameterization for application in cloud and climate models. part i: Description. *Journal of the atmospheric sciences*, 62(6):1665–1677, 2005.
149. H. Morrison, G. Thompson, and V. Tatarskii. Impact of cloud microphysics on the development of trailing stratiform precipitation in a simulated squall line: Comparison of one- and two-moment schemes. *Monthly Weather Review*, 137: 991 – 1007, 2009. doi: 10.1175/2008MWR2556.1.
150. H. Morrison, G. Thompson, and V. Tatarskii. Impact of cloud microphysics on the development of trailing stratiform precipitation in a simulated squall line: Comparison of one-and two-moment schemes. *Monthly weather review*, 137(3): 991–1007, 2009.

151. I. Morrison, S. Businger, F. Marks, P. Dodge, and J. A. Businger. An observational case for the prevalence of roll vortices in the hurricane boundary layer. *Journal of the Atmospheric Sciences*, 62(8):2662–2673, 2005.
152. R. K. Mrvaljevic, P. G. Black, L. R. Centurioni, Y.-T. Chang, E. A. D’Asaro, S. R. Jayne, C. M. Lee, R.-C. Lien, I.-I. Lin, J. Morzel, et al. Observations of the cold wake of typhoon fanapi (2010). *Geophysical Research Letters*, 40(2): 316–321, 2013.
153. S. Müller, L. Schüller, A. Zech, and F. Heße. Gstools v1. 3: A toolbox for geostatistical modelling in python. *Geoscientific Model Development*, 15(7): 3161–3182, 2022.
154. W. Munters, C. Meneveau, and J. Meyers. Turbulent inflow precursor method with time-varying direction for large-eddy simulations and applications to wind farms. *Boundary-Layer Meteorology*, 159:305–328, 2016.
155. D. Muñoz-Esparza, B. Kosović, J. Mirocha, and J. van Beeck. Bridging the Transition from Mesoscale to Microscale Turbulence in Numerical Weather Prediction Models. *Boundary-Layer Meteorol*, 153(3):409–440, Dec. 2014. ISSN 0006-8314, 1573-1472.
156. M. Nakanishi and H. Niino. Large-eddy simulation of roll vortices in a hurricane boundary layer. *Journal of the Atmospheric Sciences*, 69(12):3558–3575, 2012.
157. K. M. Nardi, C. M. Zarzycki, V. E. Larson, and G. H. Bryan. Assessing the Sensitivity of the Tropical Cyclone Boundary Layer to the Parameterization of Momentum Flux in the Community Earth System Model. *Monthly Weather Review*, 150(4):883–906, 2022.
158. V. K. Natrajan and K. T. Christensen. The role of coherent structures in subgrid-scale energy transfer within the log layer of wall turbulence. *Physics of Fluids*, 18(6), 2006.
159. D. S. Nolan, Y. Moon, and D. P. Stern. Tropical cyclone intensification from asymmetric convection: Energetics and efficiency. *Journal of the Atmospheric Sciences*, 64(10):3377–3405, 2007.
160. D. S. Nolan, N. A. Dahl, G. H. Bryan, and R. Rotunno. Tornado vortex structure, intensity, and surface wind gusts in large-eddy simulations with fully developed turbulence. *Journal of the Atmospheric Sciences*, 74(5):1573–1597, 2017.
161. K. Nolan, E. Walsh, and D. McEligot. Quadrant analysis of a transitional boundary layer subject to free-stream turbulence. *Journal of Fluid Mechanics*, 658:310–335, 2010.
162. C. N. Oguejiofor, G. H. Bryan, R. Rotunno, P. P. Sullivan, and D. H. Richter. The Role of Turbulence in an Intense Tropical Cyclone: Momentum Diffusion,

- Eddy Viscosities, and Mixing Lengths. *Journal of the Atmospheric Sciences*, 2024.
163. R. Oyama and A. Wada. The relationship between convective bursts and warm-core intensification in a nonhydrostatic simulation of typhoon lionrock (2016). *Monthly Weather Review*, 147(5):1557–1579, 2019.
  164. E. Palmén, C. W. Newton, et al. *Atmospheric circulation systems: their structure and physical interpretation*. Academic press, 1969.
  165. H. Panofsky. The variation of the turbulence spectrum with height under superadiabatic conditions. *Quarterly Journal of the Royal Meteorological Society*, 79(339):150–153, 1953.
  166. H. A. Panofsky and R. A. McCormick. The spectrum of vertical velocity near the surface. *Quarterly Journal of the Royal Meteorological Society*, 86(370):495–503, 1960.
  167. J. Persing, M. T. Montgomery, J. C. McWilliams, and R. K. Smith. Asymmetric and axisymmetric dynamics of tropical cyclones. *Atmospheric Chemistry and Physics*, 13(24):12299–12341, 2013.
  168. L. Prandtl. Zur turbulenten Strömung in Rohren und längs Platten. In *Ergebnisse der aerodynamischen Versuchsanstalt zu Göttingen Lfg. 4*, pages 18–29. De Gruyter, 1932.
  169. J. F. Price. Upper ocean response to a hurricane. *Journal of Physical Oceanography*, 11(2):153–175, 1981.
  170. J. F. Price, J. Morzel, and P. P. Niiler. Warming of sst in the cool wake of a moving hurricane. *Journal of Geophysical Research: Oceans*, 113(C7), 2008.
  171. D. E. Protzko, S. R. Guimond, C. R. Jackson, J. W. Sapp, Z. Jelenak, and P. S. Chang. Documenting Coherent Turbulent Structures in the Boundary Layer of Intense Hurricanes through Wavelet Analysis on IWRAP and SAR Data. *IEEE Transactions on Geoscience and Remote Sensing*, 2023.
  172. D. H. Richter, C. Wainwright, D. P. Stern, G. H. Bryan, and D. Chavas. Potential low bias in high-wind drag coefficient inferred from dropsonde data in hurricanes. *Journal of the Atmospheric Sciences*, 78(7):2339–2352, 2021.
  173. D. H. Richter, C. Wainwright, D. P. Stern, G. H. Bryan, and D. Chavas. Potential low bias in high-wind drag coefficient inferred from dropsonde data in hurricanes. *Journal of the Atmospheric Sciences*, 78:2339 – 2352, 2021.
  174. S. Robinson. The kinematics of turbulent boundary layer structure, NASA TM-103859. *Ames Res. Centre, Moffett Field*, 1991.

175. S. Robinson, S. J. Kline, and P. Spalart. A review of quasi-coherent structures in a numerically simulated turbulent boundary layer. In *Quasi-Coherent Structures in the Turbulent Boundary Layer, part 2. Verification and New Inform. from a Numerically Simulated Flat-Plate Layer at Memorial Intern. Seminar on Near-Wall Turbulence*, number NASA-TM-102191, 1989.
176. S. K. Robinson. Coherent motions in the turbulent boundary layer. *Annual review of fluid mechanics*, 23(1):601–639, 1991.
177. R. Rogers, S. Aberson, M. Black, P. Black, J. Cione, P. Dodge, J. Dunion, J. Gamache, J. Kaplan, M. Powell, et al. The intensity forecasting experiment: A NOAA multiyear field program for improving tropical cyclone intensity forecasts. *Bulletin of the American Meteorological Society*, 87(11):1523–1538, 2006.
178. R. Rogers, S. Lorsolo, P. Reasor, J. Gamache, and F. Marks. Multiscale analysis of tropical cyclone kinematic structure from airborne Doppler radar composites. *Monthly Weather Review*, 140(1):77–99, 2012.
179. R. F. Rogers, J. A. Zhang, J. Zawislak, H. Jiang, G. R. Alvey III, E. J. Zipser, and S. N. Stevenson. Observations of the structure and evolution of hurricane edouard (2014) during intensity change. part ii: Kinematic structure and the distribution of deep convection. *Monthly Weather Review*, 144(9):3355–3376, 2016.
180. C. Rossby and R. Montgomery. *The layer of frictional influence in wind and ocean currents. Papers in Physical Oceanography and Meteorology 3 (3)*. Cambridge, MA: Massachusetts Institute of Technology and Woods Hole . . . , 1935.
181. R. Rotunno and G. H. Bryan. Effects of parameterized diffusion on simulated hurricanes. *Journal of the atmospheric sciences*, 69(7):2284–2299, 2012.
182. R. Rotunno and K. A. Emanuel. An air–sea interaction theory for tropical cyclones. Part II: Evolutionary study using a nonhydrostatic axisymmetric numerical model. *Journal of Atmospheric Sciences*, 44(3):542–561, 1987.
183. R. Rotunno, Y. Chen, W. Wang, C. Davis, J. Dudhia, and G. Holland. Large-eddy simulation of an idealized tropical cyclone. *Bulletin of the American Meteorological Society*, 90(12):1783–1788, 2009.
184. C. M. Rozoff, D. S. Nolan, G. H. Bryan, E. A. Hendricks, and J. Knievel. Large-eddy Simulations of the Tropical Cyclone Boundary Layer at Landfall in an Idealized Urban Environment. *Journal of Applied Meteorology and Climatology*, Sept. 2023. doi: 10.1175/jamc-d-23-0024.1. URL <https://doi.org/10.1175/jamc-d-23-0024.1>.
185. J. E. Rudzin, L. K. Shay, and B. Jaimes de la Cruz. The impact of the amazon–orinoco river plume on enthalpy flux and air–sea interaction within caribbean sea tropical cyclones. *Monthly weather review*, 147(3):931–950, 2019.

186. J. E. Rudzin, S. Chen, E. R. Sanabia, and S. R. Jayne. The air-sea response during hurricane irma’s (2017) rapid intensification over the amazon-orinoco river plume as measured by atmospheric and oceanic observations. *Journal of Geophysical Research: Atmospheres*, 125(18):e2019JD032368, 2020.
187. S. Salesky and W. Anderson. Coherent structures modulate atmospheric surface layer flux-gradient relationships. *Physical Review Letters*, 125(12):124501, 2020.
188. E. R. Sanabia and S. R. Jayne. Ocean observations under two major hurricanes: Evolution of the response across the storm wakes. *AGU Advances*, 1(3):e2019AV000161, 2020.
189. L. R. Schade and K. A. Emanuel. The ocean’s effect on the intensity of tropical cyclones: Results from a simple coupled atmosphere–ocean model. *Journal of the Atmospheric Sciences*, 56(4):642–651, 1999.
190. H. Schlichting and J. Kestin. *Boundary layer theory*, volume 121. Springer, 1961.
191. K. J. Sellwood, J. A. Sippel, and A. Aksoy. Assimilation of Coyote Small Uncrewed Aircraft System Observations in Hurricane Maria (2017) Using Operational HWRF. *Weather and Forecasting*, 38(6):901–919, 2023.
192. Y. Shah, S. Ghaemi, and S. Yarusevych. Three-dimensional characterization of Reynolds shear stress in near-wall coherent structures of polymer drag reduced turbulent boundary layers. *Experiments in Fluids*, 62:1–21, 2021.
193. R. H. Shaw, J. Tavangar, and D. P. Ward. Structure of the Reynolds stress in a canopy layer. *Journal of Applied Meteorology and Climatology*, 22(11):1922–1931, 1983.
194. L. K. Shay, G. J. Goni, and P. G. Black. Effects of a warm oceanic feature on hurricane opal. *Monthly Weather Review*, 128(5):1366–1383, 2000.
195. D. J. Shea and W. M. Gray. The hurricane’s inner core region. I. Symmetric and asymmetric structure. *Journal of the Atmospheric Sciences*, 30(8):1544–1564, 1973.
196. T.-H. Shih, J. L. Lumley, and J. Janicka. Second-order modelling of a variable-density mixing layer. *Journal of Fluid Mechanics*, 180:93–116, 1987.
197. J. Smagorinsky. General circulation experiments with the primitive equations: I. The basic experiment. *Monthly Weather Review*, 91(3):99–164, 1963.
198. C. R. Smith, J. Walker, A. Haidari, and U. Sobrun. On the dynamics of near-wall turbulence. *Philosophical Transactions of the Royal Society of London. Series A: Physical and Engineering Sciences*, 336(1641):131–175, 1991.

199. R. K. Smith and M. T. Montgomery. Hurricane boundary-layer theory. *Quarterly Journal of the Royal Meteorological Society*, 136(652):1665–1670, 2010.
200. R. K. Smith, M. T. Montgomery, and N. Van Sang. Tropical cyclone spin-up revisited. *Quarterly Journal of the Royal Meteorological Society*, 135(642):1321–1335, 2009.
201. P. R. Spalart. Direct simulation of a turbulent boundary layer up to  $Re_\theta = 1410$ . *Journal of fluid mechanics*, 187:61–98, 1988.
202. N. Sparks, K. Hon, P. Chan, S. Wang, J. Chan, T. Lee, and R. Toumi. Aircraft observations of tropical cyclone boundary layer turbulence over the South China Sea. *Journal of the Atmospheric Sciences*, 76(12):3773–3783, 2019.
203. M. Stanisic. *The mathematical theory of turbulence*. Springer Science & Business Media, 2012.
204. D. P. Stern and G. H. Bryan. Using simulated dropsondes to understand extreme updrafts and wind speeds in tropical cyclones. *Monthly Weather Review*, 146(11):3901–3925, 2018.
205. D. P. Stern, G. H. Bryan, and S. D. Aberson. Extreme low-level updrafts and wind speeds measured by dropsondes in tropical cyclones. *Monthly Weather Review*, 144(6):2177–2204, 2016.
206. D. P. Stern, G. H. Bryan, C.-Y. Lee, and J. D. Doyle. Estimating the risk of extreme wind gusts in tropical cyclones using idealized large-eddy simulations and a statistical–dynamical model. *Monthly Weather Review*, 149(12):4183–4204, 2021.
207. J. E. Stopa, C. Wang, D. Vandemark, R. Foster, A. Mouche, and B. Chapron. Automated global classification of surface layer stratification using high-resolution sea surface roughness measurements by satellite synthetic aperture radar. *Geophysical Research Letters*, 49(12):e2022GL098686, 2022.
208. R. B. Stull. *An introduction to boundary layer meteorology*, volume 13. Springer Science & Business Media, 1988.
209. P. P. Sullivan, J. C. McWilliams, J. C. Weil, E. G. Patton, and H. J. S. Fernando. Marine atmospheric boundary layers above heterogeneous SST: Across-front winds. *Journal of the Atmospheric Sciences*, 77:4251–4275, 2020. doi: 10.1175/JAS-D-20-0062.1.
210. J. Sun, G. Wang, X. Xiong, Z. Hui, X. Hu, Z. Ling, L. Yu, G. Yang, Y. Guo, X. Ju, et al. Impact of warm mesoscale eddy on tropical cyclone intensity. *Acta Oceanologica Sinica*, 39(8):1–13, 2020.

211. J. Tang, D. Byrne, J. A. Zhang, Y. Wang, X.-T. Lei, D. Wu, P.-Z. Fang, and B.-K. Zhao. Horizontal transition of turbulent cascade in the near-surface layer of tropical cyclones. *Journal of the Atmospheric Sciences*, 72(12):4915–4925, 2015.
212. J. Tang, J. A. Zhang, P. Chan, K. Hon, X. Lei, and Y. Wang. A direct aircraft observation of helical rolls in the tropical cyclone boundary layer. *Scientific Reports*, 11(1):18771, 2021.
213. D. Tao and F. Zhang. Evolution of dynamic and thermodynamic structures before and during rapid intensification of tropical cyclones: Sensitivity to vertical wind shear. *Monthly Weather Review*, 147(4):1171–1191, 2019.
214. H. Tennekes and J. L. Lumley. *A first course in turbulence*. MIT press, 1972.
215. T. Theodorsen. Mechanisms of turbulence. In *Proceedings of the 2<sup>nd</sup> Midwestern Conference on Fluid Mechanics, 1952*, 1952.
216. T. Theodorsen. The structure of turbulence. *50 Jahre Grenzschichtforschung: Eine Festschrift in Originalbeiträgen*, pages 55–62, 1955.
217. A. Townsend. *The structure of turbulent shear flow*. Cambridge university press, 1976.
218. T. Tsukada and T. Horinouchi. Estimation of the tangential winds and asymmetric structures in typhoon inner core region using Himawari-8. *Geophysical Research Letters*, 47(11):e2020GL087637, 2020.
219. J. B. Wadler, R. F. Rogers, and P. D. Reasor. The relationship between spatial variations in the structure of convective bursts and tropical cyclone intensification as determined by airborne doppler radar. *Monthly Weather Review*, 146(3):761–780, 2018.
220. J. B. Wadler, J. A. Zhang, R. F. Rogers, B. Jaimes, and L. K. Shay. The rapid intensification of hurricane michael (2018): Storm structure and the relationship to environmental and air–sea interactions. *Monthly weather review*, 149(1):245–267, 2021.
221. R. A. Wajsowicz. A consistent formulation of the anisotropic stress tensor for use in models of the large-scale ocean circulation. *J. Comput. Phys.*, 105:333–338, 1993.
222. J. M. Wallace. Quadrant analysis in turbulence research: history and evolution. *Annual Review of Fluid Mechanics*, 48:131–158, 2016.
223. J. M. Wallace, H. Eckelmann, and R. S. Brodkey. The wall region in turbulent shear flow. *Journal of Fluid Mechanics*, 54(1):39–48, 1972.

224. Z.-H. Wan, S.-W. Dong, N.-S. Liu, D.-J. Sun, X.-Y. Lu, et al. Conditional analysis on extreme wall shear stress and heat flux events in compressible turbulent boundary layers. *Journal of Fluid Mechanics*, 974:A38, 2023.
225. A. Wang, Y. Pan, G. H. Bryan, and P. M. Markowski. Modeling near-surface turbulence in large-eddy simulations of a tornado: An application of thin boundary layer equations. *Monthly Weather Review*, 151:1587 – 1607, 2023.
226. C. Wang, A. Mouche, R. C. Foster, D. Vandemark, J. E. Stopa, P. Tandeo, N. Longepe, and B. Chapron. Characteristics of marine atmospheric boundary layer roll vortices from Sentinel-1 SAR wave mode. In *IGARSS 2019-2019 IEEE international geoscience and Remote sensing symposium*, pages 7908–7911. IEEE, 2019.
227. C. Wang, D. Vandemark, A. Mouche, B. Chapron, H. Li, and R. C. Foster. An assessment of marine atmospheric boundary layer roll detection using Sentinel-1 SAR data. *Remote Sensing of Environment*, 250:112031, 2020.
228. H. Wang, Z. Yang, T. Wu, and S. Wang. Coherent structures associated with interscale energy transfer in turbulent channel flows. *Physical Review Fluids*, 6(10):104601, 2021.
229. S. Wang and Q. Jiang. Impact of vertical wind shear on roll structure in idealized hurricane boundary layers. *Atmospheric Chemistry and Physics*, 17(5):3507–3524, 2017.
230. R. Webster and M. A. Oliver. *Geostatistics for environmental scientists*. John Wiley & Sons, 2007.
231. L. J. Wicker and W. C. Skamarock. Time-splitting methods for elastic models using forward time schemes. *Monthly Weather Review*, 130:2088 – 2097, 2002. doi: 10.1175/1520-0493(2002)130<2088:TSMFEM>2.0.CO;2.
232. R. P. Worsnop, G. H. Bryan, J. K. Lundquist, and J. A. Zhang. Using large-eddy simulations to define spectral and coherence characteristics of the hurricane boundary layer for wind-energy applications. *Boundary-Layer Meteorology*, 165: 55–86, 2017.
233. C.-C. Wu, C.-Y. Lee, and I. Lin. The effect of the ocean eddy on tropical cyclone intensity. *Journal of the Atmospheric Sciences*, 64(10):3562–3578, 2007.
234. L. Wu, B. Wang, and S. A. Braun. Impacts of air–sea interaction on tropical cyclone track and intensity. *Monthly weather review*, 133(11):3299–3314, 2005.
235. L. Wu, Q. Liu, and Y. Li. Prevalence of tornado-scale vortices in the tropical cyclone eyewall. *Proceedings of the National Academy of Sciences*, 115(33): 8307–8310, 2018.

236. L. Wu, Q. Liu, and Y. Li. Tornado-scale vortices in the tropical cyclone boundary layer: numerical simulation with the WRF–LES framework. *Atmospheric Chemistry and Physics*, 19(4):2477–2487, 2019.
237. J. Wurman and K. Kosiba. The role of small-scale vortices in enhancing surface winds and damage in Hurricane Harvey (2017). *Monthly Weather Review*, 146(3):713–722, 2018.
238. J. Wurman and J. Winslow. Intense sub-kilometer-scale boundary layer rolls observed in Hurricane Fran. *science*, 280(5363):555–557, 1998.
239. F. Xu and A. Ignatov. Evaluation of in situ sea surface temperatures for use in the calibration and validation of satellite retrievals. *Journal of Geophysical Research: Oceans*, 115(C9), 2010.
240. F. Xu and A. Ignatov. In situ sst quality monitor (i quam). *Journal of Atmospheric and Oceanic Technology*, 31(1):164–180, 2014.
241. F. Xu and A. Ignatov. Error characterization in iquam ssts using triple collocations with satellite measurements. *Geophysical Research Letters*, 43(20):10–826, 2016.
242. G. Yang, F. Wang, Y. Li, and P. Lin. Mesoscale eddies in the northwestern subtropical pacific ocean: Statistical characteristics and three-dimensional structures. *Journal of Geophysical Research: Oceans*, 118(4):1906–1925, 2013.
243. G. Yang, W. Yu, Y. Yuan, X. Zhao, F. Wang, G. Chen, L. Liu, and Y. Duan. Characteristics, vertical structures, and heat/salt transports of mesoscale eddies in the southeastern tropical indian ocean. *Journal of Geophysical Research: Oceans*, 120(10):6733–6750, 2015.
244. F. Zhang and D. Tao. Effects of vertical wind shear on the predictability of tropical cyclones. *Journal of the Atmospheric Sciences*, 70(3):975–983, 2013.
245. J. Zhang, Y. Lin, D. R. Chavas, and W. Mei. Tropical cyclone cold wake size and its applications to power dissipation and ocean heat uptake estimates. *Geophysical Research Letters*, 46(16):10177–10185, 2019.
246. J. A. Zhang and W. M. Drennan. An observational study of vertical eddy diffusivity in the hurricane boundary layer. *Journal of the Atmospheric Sciences*, 69(11):3223–3236, 2012.
247. J. A. Zhang and F. D. Marks. Effects of horizontal diffusion on tropical cyclone intensity change and structure in idealized three-dimensional numerical simulations. *Monthly Weather Review*, 143(10):3981–3995, 2015.
248. J. A. Zhang and M. T. Montgomery. Observational estimates of the horizontal eddy diffusivity and mixing length in the low-level region of intense hurricanes. *Journal of the Atmospheric Sciences*, 69(4):1306–1316, 2012.

249. J. A. Zhang, K. B. Katsaros, P. G. Black, S. Lehner, J. R. French, and W. M. Drennan. Effects of roll vortices on turbulent fluxes in the hurricane boundary layer. *Boundary-layer meteorology*, 128:173–189, 2008.
250. J. A. Zhang, W. M. Drennan, P. G. Black, and J. R. French. Turbulence structure of the hurricane boundary layer between the outer rainbands. *Journal of the Atmospheric Sciences*, 66(8):2455–2467, 2009.
251. J. A. Zhang, F. D. Marks, M. T. Montgomery, and S. Lorsolo. An estimation of turbulent characteristics in the low-level region of intense Hurricanes Allen (1980) and Hugo (1989). *Monthly Weather Review*, 139(5):1447–1462, 2010.
252. J. A. Zhang, R. F. Rogers, D. S. Nolan, and F. D. Marks Jr. On the characteristic height scales of the hurricane boundary layer. *Monthly Weather Review*, 139(8): 2523–2535, 2011.
253. J. A. Zhang, R. F. Rogers, P. D. Reasor, and J. Gamache. The mean kinematic structure of the tropical cyclone boundary layer and its relationship to intensity change. *Monthly Weather Review*, 151(1):63–84, 2023.
254. P. Zhu. Simulation and parameterization of the turbulent transport in the hurricane boundary layer by large eddies. *Journal of Geophysical Research: Atmospheres*, 113(D17), 2008.